ISSN
2395-6992

International Journal of Engineering Research & Science

www.ijoer.com
www.adpublications.org

Volume-4! Issue-4! April, 2018 www.ijoer.com ! info@ijoer.com

Preface

We would like to present, with great pleasure, the inaugural volume-4, Issue-4, April 2018, of a scholarly journal, *International Journal of Engineering Research & Science*. This journal is part of the AD Publications series *in the field of Engineering, Mathematics, Physics, Chemistry and science Research Development*, and is devoted to the gamut of Engineering and Science issues, from theoretical aspects to application-dependent studies and the validation of emerging technologies.

This journal was envisioned and founded to represent the growing needs of Engineering and Science as an emerging and increasingly vital field, now widely recognized as an integral part of scientific and technical investigations. Its mission is to become a voice of the Engineering and Science community, addressing researchers and practitioners in below areas

Chemical Engineering	
Biomolecular Engineering	Materials Engineering
Molecular Engineering	Process Engineering
Corrosion Engineering	
Civil Engineering	
Environmental Engineering	Geotechnical Engineering
Structural Engineering	Mining Engineering
Transport Engineering	Water resources Engineering
Electrical Engineering	
Power System Engineering	Optical Engineering
Mechanical Engineering	
Acoustical Engineering	Manufacturing Engineering
Optomechanical Engineering	Thermal Engineering
Power plant Engineering	Energy Engineering
Sports Engineering	Vehicle Engineering
Software Engineering	
Computer-aided Engineering	Cryptographic Engineering
Teletraffic Engineering	Web Engineering
System Engineering	
Mathematics	
Arithmetic	Algebra
Number theory	Field theory and polynomials
Analysis	Combinatorics
Geometry and topology	Topology
Probability and Statistics	Computational Science
Physical Science	Operational Research
Physics	
Nuclear and particle physics	Atomic, molecular, and optical physics
Condensed matter physics	Astrophysics
Applied Physics	Modern physics
Philosophy	Core theories

Chemistry	
Analytical chemistry	Biochemistry
Inorganic chemistry	Materials chemistry
Neurochemistry	Nuclear chemistry
Organic chemistry	Physical chemistry
Other Engineering Areas	
Aerospace Engineering	Agricultural Engineering
Applied Engineering	Biomedical Engineering
Biological Engineering	Building services Engineering
Energy Engineering	Railway Engineering
Industrial Engineering	Mechatronics Engineering
Management Engineering	Military Engineering
Petroleum Engineering	Nuclear Engineering
Textile Engineering	Nano Engineering
Algorithm and Computational Complexity	Artificial Intelligence
Electronics & Communication Engineering	Image Processing
Information Retrieval	Low Power VLSI Design
Neural Networks	Plastic Engineering

Each article in this issue provides an example of a concrete industrial application or a case study of the presented methodology to amplify the impact of the contribution. We are very thankful to everybody within that community who supported the idea of creating a new Research with IJOER. We are certain that this issue will be followed by many others, reporting new developments in the Engineering and Science field. This issue would not have been possible without the great support of the Reviewer, Editorial Board members and also with our Advisory Board Members, and we would like to express our sincere thanks to all of them. We would also like to express our gratitude to the editorial staff of AD Publications, who supported us at every stage of the project. It is our hope that this fine collection of articles will be a valuable resource for *IJOER* readers and will stimulate further research into the vibrant area of Engineering and Science Research.

Mukesh Arora

(Chief Editor)

Board Members

Dr. S.R.Boselin Prabhu

Ph.D, Wireless Sensor Networks, M.E. Network Engineering, Excellent Professional Achievement Award Winner from Society of Professional Engineers Biography Included in Marquis Who's Who in the World (Academic Year 2015 and 2016). Currently Serving as Assistant Professor in the department of ECE in SVS College of Engineering, Coimbatore.

Dr. Maheshwar Shrestha

Postdoctoral Research Fellow in DEPT. OF ELE ENGG & COMP SCI, SDSU, Brookings, SD Ph.D, M.Sc. in Electrical Engineering from SOUTH DAKOTA STATE UNIVERSITY, Brookings, SD.

Zairi Ismael Rizman

Senior Lecturer, Faculty of Electrical Engineering, Universiti Teknologi MARA (UiTM) (Terengganu) Malaysia Master (Science) in Microelectronics (2005), Universiti Kebangsaan Malaysia (UKM), Malaysia. Bachelor (Hons.) and Diploma in Electrical Engineering (Communication) (2002), UiTM Shah Alam, Malaysia

Dr. D. Amaranatha Reddy

Ph.D.(Postdocteral Fellow,Pusan National University, South Korea), M.Sc., B.Sc. : Physics.

Dr. Dibya Prakash Rai

Post Doctoral Fellow (PDF), M.Sc.,B.Sc., Working as Assistant Professor in Department of Physics in Pachhuncga University College, Mizoram, India.

Dr. Pankaj Kumar Pal

Ph.D R/S, ECE Deptt., IIT-Roorkee.

Dr. P. Thangam

BE(Computer Hardware & Software), ME(CSE), PhD in Information & Communication Engineering, currently serving as Associate Professor in the Department of Computer Science and Engineering of Coimbatore Institute of Engineering and Technology.

Dr. Pradeep K. Sharma

PhD., M.Phil, M.Sc, B.Sc, in Physics, MBA in System Management, Presently working as Provost and Associate Professor & Head of Department for Physics in University of Engineering & Management, Jaipur.

Dr. R. Devi Priya

Ph.D (CSE),Anna University Chennai in 2013, M.E, B.E (CSE) from Kongu Engineering College, currently working in the Department of Computer Science and Engineering in Kongu Engineering College, Tamil Nadu, India.

Dr. Sandeep

Post-doctoral fellow, Principal Investigator, Young Scientist Scheme Project (DST-SERB), Department of Physics, Mizoram University, Aizawl Mizoram, India- 796001.

Mr. Abilash

MTech in VLSI, BTech in Electronics & Telecommunication engineering through A.M.I.E.T.E from Central Electronics Engineering Research Institute (C.E.E.R.I) Pilani, Industrial Electronics from ATI-EPI Hyderabad, IEEE course in Mechatronics, CSHAM from Birla Institute Of Professional Studies.

Mr. Varun Shukla

M.Tech in ECE from RGPV (Awarded with silver Medal By President of India), Assistant Professor, Dept. of ECE, PSIT, Kanpur.

Mr. Shrikant Harle

Presently working as a Assistant Professor in Civil Engineering field of Prof. Ram Meghe College of Engineering and Management, Amravati. He was Senior Design Engineer (Larsen & Toubro Limited, India).

Table of Contents

Dimensioning of a natural ponds as wastewater treatment plant for the city of Ouazzane

SIBARI M.[1*], A. EL ATMANI[2], Y. SAIDI[3], M. LAKHLIFI[4], K. EL KHARRIM[5], D. BELGHYTI[6*]

[1-6]Laboratory Biotechnology, Environment & Quality, Faculty of Sciences, University Ibn Tofail, PB: 133, 14000 Kenitra, Morocco.
[1]ONEP, Regional Office of Water and Electricity, Kenitra, Morocco.
[2]Studies Technical Office, Rabat, Morocco.
[3]Studies Technical Office, Meknes, Morocco.
[4]Redal Violea, Water and Electricity, Rabat, Morocco.
*Corresponding authors
Email: sibari20@yahoo.fr; belghyti@hotmail.com

Abstract*—Morocco has a mobilizable water heritage of 21 billion m^3 including 16 billion m^3 of surface water and 5 billion m^3 of groundwater. Unfortunately due to the exponential population growth and economic and social development, these water resources cannot meet the growing demand of the agriculture, industry and drinking water sectors.*

In addition, more than 546 million m^3 of raw wastewater is discharged annually into the receiving environment and only a tiny proportion is reused in the irrigation of about 7000 ha. Most of the wastewater discharged is responsible for the pollution of the environment.

To seek new water resources while curbing pollution, Morocco has undertaken a gigantic project of treatment of its wastewater. The city of Ouazzane, like other urban agglomerations, must choose an adequate system for the purification of its wastewater discharges.

The present work proposes the design and sizing of a natural lagoon WWTP based on demographic data, pollutant load, wastewater flow and availability of land for the city of Ouazzane.

The project proposes a pretreatment using a vertical manual screens of 36 bars of 10 mm diameter and spaced 12 mm and a Grit/Grease Separator of 5.6x1.8 m in size. Primary treatment with a circular primary decanter 16 m in diameter, 3 m deep and 602.88 m in volume. Four anaerobic basins 4 m deep, 8204 m^3 in volume and 58.02 x 35.35 m in size. Also four Optional ponds 2m deep, 41008m^3 deep and 107 x 192m in size. Finally, four maturation ponds of 1 m deep and 6400 m^3 of volume each.

***Keywords*— Wastewaters, Epuration, Lagoons, Ouazzane, Morocco.**

I. INTRODUCTION

Our study focuses on the choice of the appropriate purification system to treat wastewaters from the city of Ouazzane. Unfortunately, several constraints will have an influence on the choice of the most suitable method for the habitat of Ouazzane. Among these, we can note: the high altitudes, a rugged topography and difficult accesses; irregularity of use; Difficult energy supply; weakness of economic and financial resources [1].

So after the examination of the studied treatment variants (Activated sludge, Lagoon, Bacterial bed, Reed plant filters ...) our choice was based on the techniques presenting a good robustness of treatment, a level of technicality easy to implement and reasonable investment and operating costs. As a result, the process that will be used for the purification of the effluent volumes to be treated is a natural lagoon.

In agreement with ONEP, we included a pretreatment, primary treatment (anaerobic lagoons) and secondary treatment (optional lagoons) and we added a tertiary treatment (ripening lagoons). In what follows in the present study, the objective was to calculate or deduce the volume load, the pollutant load, the surface load, the flow rates of the raw sewage and the dimensions of the different lagoons, the time of sewage stays, the total surface area of the WWTP.

II. STUDY AREA

2.1 Geographical Position

The city of Ouazzane is located in the northern limit of the Gharb plain. The topography of the city is contrasted: Upstream, on the hill, the slopes are of the order of a few percent. Further downstream, at the level of the urban site, the general slope is weaker until the outlet in the low-slope agricultural plain [2].

The city of Ouazzane is 171 km from Rabat and 134 km from Fez. It is crossed by the RN13 national road connecting Meknes - Tetouan and RR408 regional road. The center is part of the geographical area of the Pre-rif and from an administrative point of view, the center of Ouazzane comes from the region of Tangier-Tetouan. His average Lambert coordinates are: X = 484.00 and Y = 466.40 (**Figure 1**).

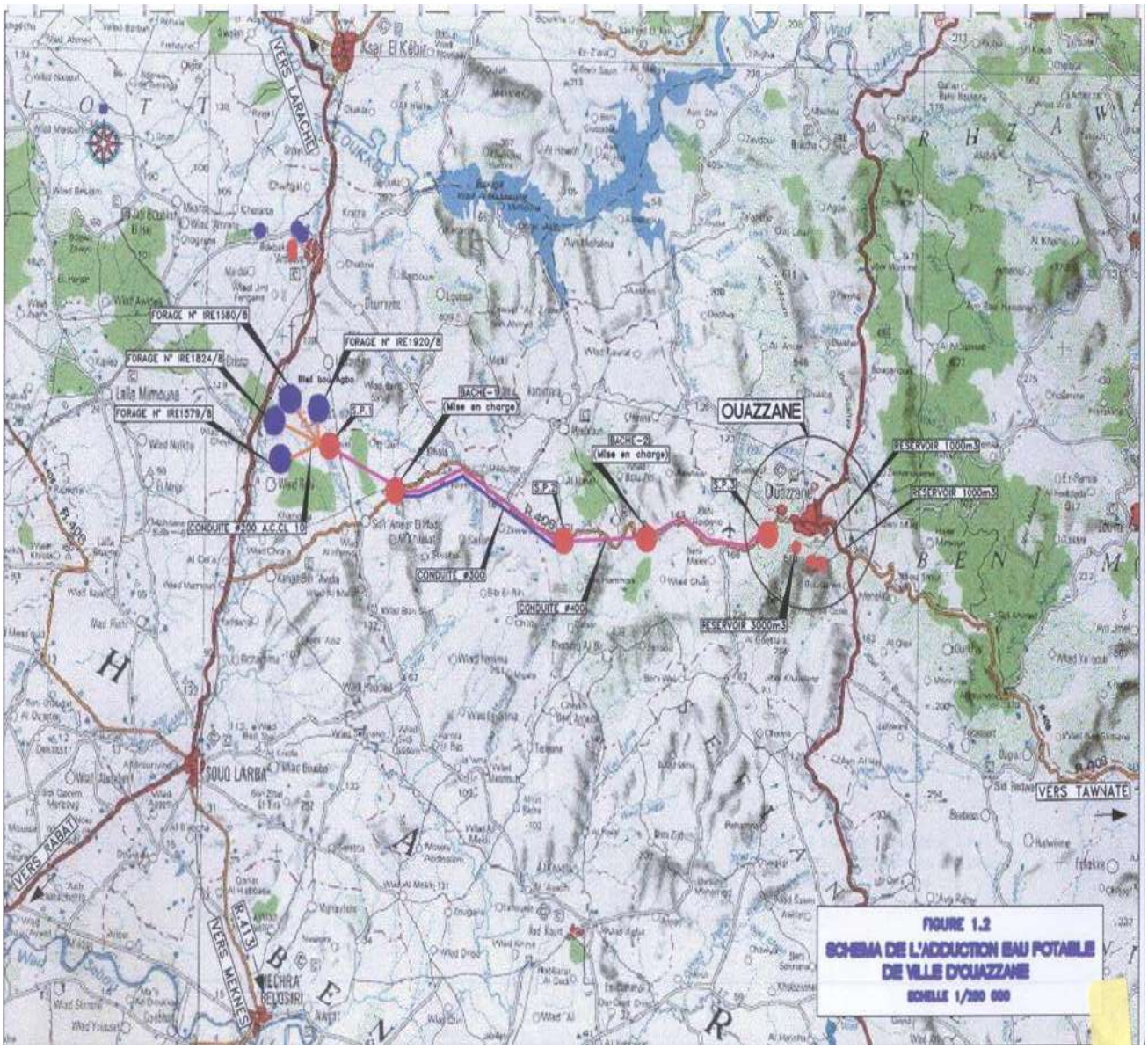

FIGURE 1: GEOGRAPHICAL LOCALIZATION OF OUAZZANE CITY

2.2 Meteorological Datas

The city of Ouazzane is located in the western part of the pre-rif mountain. It is characterized by a subhumid climate with moderate winter: the average temperature is around 18 °C, the evapotranspiration is 700 to 900 mm. Maximum, minimum

and average monthly temperatures are presented in **Table 1**. The average monthly precipitation recorded is given in Table 2 and the average annual rainfall is about 885 mm [3].

TABLE 1
MONTHLY VARIATION OF TEMPERATURE IN OUAZZANE (°C).

Months	Jan	Feb	Mar	Abr	May	Jun	Jul	Aug	Sep	Oct	Nov	Dec	Mean
Max	16,2	18,1	21	23,2	26,6	30,7	35 ,6	36	32,6	28,5	22	17,6	25 ,7
Min	5,3	5,9	7,9	9,1	11	13,9	15,9	16,2	14,8	11,9	8,7	6,6	10,6
Mean	10,8	12,0	14,5	16,2	18,8	22,3	25,8	25,8	23,7	20,2	15,4	12,1	18,1

TABLE 2
AVERAGE ANNUAL RAINFALL IN OUAZZANE

Months	Jan	Feb	Mar	Abr	May	Jun	Jul	Aug	Sep	Oct	Nov	Dec	Mean
P (mm)	129	118	119	74	45	13	1	1	14	70	127	174	73,75

2.3 Hydrology

The Ouazzane city is built on the northern flank of the syncline Bouhlal mountain, which is formed at the base by a practically impermeable schisto-sandstone series on which rests a more permeable sandstone series as one rises. Towards the top, the contact of the two series is marked by the resurgence of many sources.

The basin of Bou Agba is lined at the bottom by marls of the Miocene then come above the conglomeratic formations more or less clayey or sandy of Villafranchian age and old quaternary which outcrop largely on the edges of the basin. The River M'Da upstream of Souk El Larbaa, enters the basin of Bou-Agba from the East and comes south at Sidi Bou-Knadel to continue thereafter on the plain of Gharb. The River M'Da enters this basin from the east to Grouna and comes south to the threshold of Sidi Bou Knadel to then enter the plain of Gharb [4].

The tablecloth of Bou-Agba stands in the pebbles of Villafranchien, which are outcropping at the edge of the bowl and fleeing in the center under the sandy clay quaternary cover. The thickness of the pebbles is 50 m at the edges and 100 to 200 m at the center. The sheet is free on the borders (50 km^2) and in charge in the center (25 km^2). The waters of the deep aquifer of Bou-Agba are sweet of good quality (less than 0.5 g / L of total salts) and calcium carbonate type.

In addition, the geotechnical surveys undertaken in Ouazzane recently showed at the level of the city and its sewerage network the ground is rather clayey, without presence of tablecloth at the level of the projected WWTP. The terrain is also clayey, impervious since the permeability coefficient revealed on the WWTP site, by the measurements is of the order of 10-9 cm/s (10-11 m/s).

The drinking water supply of the city of Ouazzane is provided by 4 boreholes located about 40 km from the city so far from the planned site of the WWTP in the basin of Bou-Agba which houses a large underground water reserve [5].

2.4 Economic Activity

The agricultural vocation of the Ouazzane city contributes to the relative dynamism of the local economy. Ten rural communes belong to the very wide circle of Ouazzane. The Ouazzane region is especially famous for its olive trees. In fact, among the 17,000 hectares cultivated by arboriculture, there are 15,000 hectares of olives and around 1,500,000 trees producing up to 25,000 tons of olives per year. There is also an area of 600 hectares exploited in apricots and with an annual production of 1500 tons / year, and 1000 hectares of fig trees with 1500 tons /year. The animal production of red meat reaches 1243 tons/year. The herd consists of 48,000 head of cattle, 181,000 head of sheep and 14500 head of goats.

The city of Ouazzane does not have any industrial zone structured, however it is necessary to note the existence of six oil mills of which five oil mills are of minor importance and a Moroccan Industrial Oil Company of Ouazzane (SIMOD) which is the most important oil mill of the city. It was founded in 1968 and covers an area of 3 hectares. The purpose of the said company is the crushing of olives and the conditioning of the oil. The company exports extra virgin oil to the United States and Europe. Finally, a carob crushing plant which is the company Medi of Caroube (SMEDCA) created in 1989, its activities include the crushing of carob, the production of pipe blanks and the production of medicinal plants [6].

Craft has long been an important sector of economic activity in the city of Ouazzane since it occupies more than a quarter of the workforce. Of all the activities, local commerce occupies a dominant place. This imbalance is accentuated by the predominance of the grocery store. The tourist potential of Ouazzane is quite important. It revolves around at least six axes: Zaouia, Lake Bou Déroua, the tomb of Rabbi Amran located 10 km away in the village of Asjen, hunting, Tangier - Fès road and handicrafts. Despite this, Ouazzane lives on the sidelines of the national tourist activity. The city has only six unclassified hotels and only a few dozen beds.

III. STUDY METHODS

3.1 Basic Data for the Design of the Treatment Plant

Before considering a project to install a wastewater treatment plant (WWTP), it is necessary to collect the most general information concerning the estimation of drinking water consumption, the flow of wastewater, the load in BOD_5, the content of suspended matter, and even the temperature and solar radiation according to the seasons [7,8].

The city of Ouazzane is fed from four boreholes made at the level of the water table of the plain of Bou Agba 40 km west of the city. Capture, adduction and distribution are provided by ONEE. Currently a project to reinforce the Ouazzane city water supply from the LouKous is being implemented by ONEP. It has a distribution network powered from:

* Very high floor network: tank with a capacity of 200 m^3;

* High-level network: two tanks with a capacity of 1000 m^3;

* Network beats floor: two tanks with a capacity of 1000 and 3000 m^3;

* Network very beating floor: a tank with a capacity of 750 m^3.

We need to know the current population of the Ouazzane region, and its growth rate and projection into the future. Also we need the rate of connection to drinking water and the connection rate to the sewerage network.

3.1.1 Consumption of drinking water:

Pcd = Pt x Tbp

Pcd: Population connected to drinking water expressed in inhabitant (hab).

Pt: Total population (forecast) expressed in inhabitant (hab).

Tcd: Connection rate to drinking water expressed in%.

3.1.2 wastewater discharges:

Pcs = Pt x Tcs

Pcs: Population connected to the sewerage network expressed in inhabitant (hab).

Pt: Total population (forecast) expressed in inhabitant (hab).

Tcs: Connection rate to the sewerage network expressed in%.

The daily consumption of the population connected to drinking water must be estimated in terms of (m^3 /day). The examination of the needs sheets established by ONEE made it possible to determine the calculation assumptions to evaluate the evolution of drinking water consumption. For the determination of future consumption, the following types of users were distinguished: connected domestic users, administrative users and industrial users. The Ouazzane AEP network connection rate increased from 96% in 2006 to 98% in 2020.

The average household consumption in 2004 is 60 L / person / day. For our forecasts, we take into account the average specific consumption of 65 L / person / day in 2006.

According to ONEP data on the overall consumption of Ouazzane administrations, an average consumption of 6L/person/day is deduced. For the forecasts of the consumption of the administrative users, we start from the forecasts of ONEP of 6L/hab/d. The definition of the industrial user of ONEP is very vast and goes from trade (restaurants, cafes ... etc) to the small industry, the craft industry and tourism. We consider a consumption, at present, of 6 L / hab / d for the manufacturers of Ouazzane.

Concp = Dpcd x Pcd / 1000

Conscp: Daily consumption of the population connected to drinking water expressed in (m^3 / d).

Dpcd: Daily allocation of the population connected to drinking water expressed in (L / hab / d).

Pcd: Population connected to drinking water expressed in inhabitant (hab).

The sewage flow rates are calculated from the daily consumption of drinking water affected by a sewage discharge rate. The average daily flow is that emanating from the drinking water consumption of the connected population multiplied by the rejection rate or refund rate. The rejection rate is a function of the type of habitat, in the villa zone, it can go down to 0.5 but it can exceed 100% of the consumption if the water used does not have for only origin the water distributed by ONEP, we can adopt an average rejection rate equal to 0.8.

3.1.3 Average flow of wastewater (Qww)

Qww = Conscp x Trejc = qkP. 10^{-3}

Qww: Wastewater flows expressed in (m^3 /day):

Trejc (k) : The rejection rate expressed in% (80 to 90%).

Conscp: Daily consumption of the population connected to drinking water expressed in (m^3 / d).

q: Consumption of water Liter/person P: Population connected

3.1.4 Peak hourly rate of wastewaters Qph: The hourly peak coefficient is given by the formula:

Qph = 1.5 + (2.5 / √Qww)

With Qww = average flow (in L / s)

3.1.5 Daily point flow of wastewater Qp

The daily peak flow Qp is expressed in cubic meter / day (m3 / d).

Qp = Cp x Qww

Qp: Wastewater point flow rate expressed in cubic meter / day (m3 / d)

Cp: The point coefficient, is taken equal to 1.3. It is given by the following formula:

Cp = 1.5 + 2.5 / √Qww

3.1.6 Pollutant load Cp:

Cp = Pcs x Ratio / 1000 (Kg/day)

Ratio (gDBO5 / hab / d): Pollution ratio

3.1.7 Concentration of BOD_5

BOD_5 is expressed in mg of O_2 / L.

Concentration in BOD_5 = pollutant load x 1000 / Qww

3.1.8 Equivalent inhabitant (EH)

EH = Polluting load X 1000 / Ratio

3.1.9 Calculating stormwater flows

Various formulas for evaluating stormwater flow exist. We will use, in the present study, the superficial formula of CAQUOT [9].

3.2 Dimensioning of Pretreatment

The purpose of the pretreatment is to remove the coarsest solids or particles, which may interfere with subsequent treatments or damage the equipment. Pre-treatment includes Screenings, Grit and Grease separator.

3.2.1 Dimensioning of the "Screening".

For the choice of the manual bar screens it is necessary to calculate its total area **St** and the area between the bars **Sb** (expressed in m^2), and the number of bars **n**, and their width **l** (expressed in m) by the following formula.

$$S_t = \frac{S_v}{(i/_{i+e})} \qquad n = \frac{S_b}{(e \times h)} \qquad l = \frac{S_t}{h}$$

$$S_b = \frac{S_v \times e}{i}$$

With:

St: total area St (m^2): **Sv**: Vacuum section

e: Thickness of the bar expressed in cm. **i**: Spacing between the bars expressed in cm.

n: The number of rungs **h**: The Height of the Degreaser expressed in cm.

l: the width of the bar (m) **Sb**: the area between the bars (m^2)

3.2.2 Design of the Grit/Grease

For the choice of the Grit/Grease separator one has to calculate its horizontal surface **Sh** (expressed in m^2), its vertical surface **Svt** (expressed in m^2), the width **l** (expressed in m), the length **L** (expressed in m), the Volume **V** (expressed in m^3), and the residence time **Ts** (expressed in s).

$$S_h = \frac{Q_p}{C_s} \qquad S_{vt} = \frac{Q_p}{V_h} \qquad l = \frac{S_{vt}}{H} \qquad L = \frac{S_h}{l}$$

$$V = L \times l \times H \qquad T_s = \frac{V}{Q_p}$$

With:

Sh : The horizontal surface (m^2) **Cs**: Surface load expressed in m / h

Qp: Wastewater point flow rate expressed in cubic meter / day (m^3 / d)

Svt : The vertical Surface (m^2) **Vh**: Horizontal flow velocity expressed in m / s.

l : The width (m): **H** : Height expressed in m. **L**: The length (m)

V: The Volume (m^3) **Ts**: The residence time (s):

3.2.3 The dimensioning of the Oil, Grease and Fat Traps

For the choice of the Grease separator one must calculate its horizontal surface **Sh** (expressed in m^2), its vertical surface **Svt** (expressed in m^2), the width **l** (expressed in m), the length **L** (expressed in m), the Volume **V** (expressed in m^3), and the residence time **Ts** (expressed in s).

$$S_h = \frac{Q_p}{C_s} \qquad S_{vt} = \frac{Q_p}{V_h} \qquad l = \frac{S_{vt}}{H} \qquad L = \frac{S_h}{l}$$

$$V = L \times l \times H \qquad T_s = \frac{V}{Q_p}$$

With:

Sh: The horizontal surface (m^2) **Cs**: Surface load expressed in m / h

Svt: The vertical Surface (m^2) **Vh**: Horizontal flow velocity expressed in m / s.

l: The width (m) **H**: Height expressed in m **L**: The length (m)

V: The Volume (m^3) **Ts**: The residence time (s)

3.2.4 Dimensioning of the Primary Decanter

The primary treatment with a circular decanter is intended to complete the removal of non-decanted fines by grit removal. The decanter is sized on the basis of the dry point flow rate according to the following equations:

Sdec = Qp x Va

Vdec = Sdec x Hdec

Sdec: surface of the decanter in m^2

Qp: peak flow in dry weather m^3 / h

Va: rate of climb limit set at 1.2 m / h

Hdec: the cylindrical height is fixed at 3 m.

R dec: decanter radius in m calculated from the Sdec surface

3.3 Dimensioning of Ponds

3.3.1 Dimensioning of the Anaerobic ponds

A. The volume load (Cv):

The primary treatment chosen is a natural lagoon. To size anaerobic lagoons, criteria based on the volume load, the residence time, the depth of the basins and the treatment efficiency are used. Gloyna has shown that the decrease in BOD_5 is a function of the retention time which is itself influenced by the temperature [10].

The volume load is expressed in g of BOD5 / m3 / day and must be between 50 <300 g / m3 / day [11]. According to Mara and Pearson [12] the volume load varies mainly with temperature (**Table 3**). It is recommended in general, volume loads of 100 g / m3 / day in winter to 300 g / m3 / day in summer.

TABLE 3
VARIATION OF VOLUMETRIC CHARGE CV AS A FUNCTION OF TEMPERATURE FOR ANAEROBIC BASINS

Temperature (°C)	Volumic load (g /m^3/jour)
$T \leq 10$	100
$10 < T \leq 20$	20*T -100
$T > 20$	300

B. Volume of the water slice

The volume of the water slice is calculated as follows:

$$Vt = \frac{Cp}{Cv}$$

$$V_A = \frac{C_{OX}\, Q_{mean}}{C_{V_A}}$$

With:

Ve: volume of the water slice **Cv**: Volume load (g / m3 / d) **Cp**: pollutant load g / d

C. Volume per basin

$$V_a = \frac{V_t}{n}$$

With:

Vt: total volume of anaerobic basins in m^3. **n**: number of basins chosen.

D. Total surface needed

Area **S**, anaerobic basins is calculated by the following formula:

$$S = \frac{C_o \times Q}{P \times C_v}$$

With:

S: basin area expressed in m^2.

Co: Incoming concentration of BOD5 (mg / L).

Cv: Volume load (g DBO5 / m3 / day).

Q: Wastewater flow (m^3 / day)

P: Depth of basin.

$$S_t = \frac{V_t}{P_a}$$

Vt: total volume of anaerobic basins **Pa**: basin depth of 3 to 4 m

E. Surface per anaerobic basin:

Sa= Va/Pa

$$S_a = \frac{S_t}{n}$$

With

n: Number of basins in parallel **Va**: volume of the anaerobic basin **Pa**: depth of the basin

F. Length halfway up the water:

$$L1 = (Sa)^{0,5}$$

G. Length of water:

L2= L1+ (2× P/2× Slope)

L1: length at mid-depth.

P: Depth adopted.

Slope: internal slope of bank.

H. Bottom length:

L3= L1-(2× P/2× Slope)

L1: Length at mid-depth.

P: Depth adopted.

Slope: internal slope of the bank**.**

I. Length at the peak:

L4=L2+ (2 × Cr × Slope)

L2: Length wire water.

Cr: adopted ridge.

Slope: internal slope of the bank.

J. Residence time:

$$T_s = \frac{V_a}{Q}$$

According to Ceremher [11] **Ts** must be between 3 to 5 days.

Va: Volume of anaerobic basin m^3.

Q: discharge of wastewater at the entrance of anaerobes (in m^3 / d)

K. Effluent charge:

$$C_e = \frac{C_a}{K_t \times T_s + 1}$$

Ce: Effluent charge

Ca: Tributary charge.

Kt: Elimination coefficient of BOD_5.

Ts: Residence time.

3.3.2 Dimensioning of Facultative Ponds

In order to size the optional basins, criteria based on the surface charge **Cs**, the residence time **Ts**, the depth of the basins **Pf** and the purification efficiency **Rf** are used. Two dimensioning criteria are used for the optional basins namely:

- The surface load in kg / ha / day: minimum 1000 kg / ha / d beyond which: anaerobiosis.
- Residence or retention time.

A. Surface charge Cs (in kg / ha / d).

According to Mc Garry & Pescod [13] the surface charge **Cs** is given by the following formula:

$$C_{s(F)} = \frac{(60.3 \times (1.0993)^T)}{1.3}$$

According to Mara and Pearson, [12] the **SF** surface is given by the following equation:

$$S_{(F)} = 10000 \times \frac{\text{Charge polluante}_{\left(Kg/j\right)}}{C_{S(F)}}$$

Cs: Surface load (in kg / ha / d). **T**: Residence time

SF : The required area (in m^2).

$$S_F = \frac{C_F}{C_s}$$

With :

SF: Total area needed (in ha).

CF: Load at the entrance of the optional pools.

Cs: Superficial charge.

B. Volume of basins:

$$VF = SF \times PF$$

C. Residence time (days).

According to Mara and Pearson, [12] the residence time is given by the following formula:

$$T_{S(F)} = \frac{S_{(F)} \times P_F}{Q}$$

If **Ts** <15 days: Take **Ts**(f) = 15 days and recalculate the depth **P** by the relation:

$$S_F = 15 \times \frac{Q}{P_F}$$

D. Depth of basins (m)

According to Mara and Pearson [12], the Depth of basins (in m) should be 1.2 to 2 m. $\mathbf{P_F}$= 1.5 m.

E. Purification performance

The BOD_5 of the effluent at the outlet of the optional pond is the same as that of the entrance of the ripening basin:

$$C_2 = \frac{C_1}{1 + T_{a(F)} \times T_{S(F)}}$$

The rate of abatement of BOD5 at the level of the optional pond depends solely on the temperature, it is determined by:

$$T_a = (1 - \frac{1}{1 + K \times T_{S(F)}}) \times 100$$

K according to Marais [14] and Demillac [15].

$$T_{a(F)} = 0.3 \times (1.05)^{(T-20)}$$

For wastewater that will be discharged into the natural environment, the BOD_5 at the outlet of the optional pond **C2** must be less than 120 mg / L, if this is not the case it will be necessary to increase the residence time $\mathbf{T_{SF}}$ to have **C2** = 120 mg / L.

3.3.3 Dimensioning of Maturation Ponds

The maturation pond is a shallow, aerobic basin whose role is the elimination of pathogens. The sizing of this basin is done by the following relations:

Volume of the maturation basin Vm in m^3

Vm = Q_{ww} x Tsm

Surface of the maturation basin Sm in m^2

Sm = Vm / Pm

Residence time in the maturation basin Tsm in days

Tsm = (1 / β x K) x log (Lsf / Lsm)

With:

Pm: depth of the maturation basin

Lsf: DBO_5 at the optional basin exit

Lsm: BOD_5 at the outlet of the maturation pond.

IV. RESULTS AND DISCUSSION

4.1 Evaluation of the Flow of Parasitic Water

After analysis of the results of the various characterization and consultation campaigns with ONEP, we selected 35% of the average discharge for the parasitic waters in 2006. This rate decreases to 20% in 2020 and 20% in 2040. This regression is explained by the improvement of the networks after completion of the project and intervention of ONEP for the management of the sanitation service.

4.2 Volume of Ouazzane Sewage

In Morocco, the discharge rates usually used for domestic wastewater are between 70% and 85% of the volume consumed (**Table 4**) ONEP / GTZ, [16]. According to the reconnaissance on the spot and in other cities of the country, we adopted for the city of Ouazzane a rate of rejection of 80% for the domestic, administrative and industrial uses.

The average connection rate is 91% for the year 2004. As hypothesis for the evolution of the connection rate, we consider an increase from 96% in 2008 to 98% in 2030. The total discharges of the city of Ouazzane are presented in **Table 5**. The calculation of wastewater discharges has been carried out for the River Rha and Rabat River basins, since the treatment plant will be sized only for the treatment of discharges of these two basins (**Table 6**).

4.3 Estimation of the Pollutant Load of Ouazzane

For the pollutant load calculation we adopted the national plan of liquid sanitation ratios for cities of similar size (27 to 30 g BOD_5 / hab / d). For the calculation of the polluting load coming from collectives and administrative users, high schools with boarding schools, hospitals, dispensaries and slaughterhouses were taken into account. The contribution of different users in the collective sector is as follows:

High school with internship: 25 g / pupil / day

Military (barracks): 40 g / effective / day

Hospital: 60 g / bed / day

Abattoirs: Sheep and goats: 500 g BOD5 / head / day; Cattle: 3000 g BOD5 / head / day; Moorish baths: 20 g / visitor / day.

The lagoon purification process recreates the conditions of self-purification of the natural environment. The proper functioning of a lagoon depends on the balance between different groups of animal and plant species (bacteria, zooplankton, algae and aquatic plants). Photosynthesis plays a driving role.

TABLE 4
OVERALL CONSUMPTION OF DRINKING WATER

	2006	2007	2008	2010	2015	2020	2025	2030	2035	2040	2048
Consumption											
population (hab)	59255	59907	60566	61905	65386	69386	72945	77046	81378	85953	93815
Connection Rate %	96	96	96	98	98	98	98	98	98	98	98
Population Connected (hab)	56885	57510	58143	60667	64078	67681	71486	75505	79750	84234	91939
Population Not Connected (hab)	2370	2396	2423	1238	1308	1381	1459	1541	1628	1719	1876
Endowments L/hab/d											
Population Connected (hab)	65	65	65	65	65	65	65	65	65	65	65
Population Not Connected (hab)	15	15	15	15	15	15	15	15	15	15	15
Administrative	6	6	6	6	6	6	6	6	6	6	6
Industrials	6	6	6	6	6	6	6	6	6	6	6
Consumptions (m^3/d)											
Population Connected	3697	2738	3779	3943	4165	4399	4647	4908	5184	5475	5976
Population Not Connected	36	36	36	19	20	21	22	23	24	26	28
Endowments L/hab/j	63	63	63	64	64	64	64	64	64	64	64
Consumption domestic	3733	3774	3816	3962	4185	4420	4668	4931	5208	5501	6004
Consumption administrative	356	359	363	371	392	414	438	462	488	516	563
Consumption industrial	356	359	363	371	392	414	438	462	488	516	563
Total Consumption m^3/d	4444	4493	4542	4705	4969	5249	5544	5856	6185	6532	7130
Net Endowments L/hab/d	75	75	75	76	76	76	76	76	76	76	76

Indeed, algae produce oxygen by photosynthesis. This oxygen is used by bacteria to mineralize and assimilate organic matter, hence the production of carbon dioxide, nitrates, and phosphates. Decantable materials are deposited at the bottom of the lagoon. They are regularly extracted from the system, in order to keep the installations running smoothly. To prevent coarse materials from accumulating in the basins, a screening facility is recommended upstream.

We have also taken into account the polluting flows of the businesses in the domestic expenses. For industrial companies, we consider only water consuming establishments and tourist establishments. In these cases, the costs are estimated by considering the specific conditions of the establishments, the industry or the industrial zone in question.

The specific pollutant fluxes in g / hab / day equivalent for the different parameters are presented in Table 6 below:

- **BOD_5: a** pollutant flux of 27 g BOD_5 / person / day in 2006 and 30 g / person / day for 2020 is adopted. This increase results from an improvement in the standard of living of the population of Ouazzane;
- **COD:** for the COD, it is adopted a value of 80 g / hab / d for the year 2006. We adopted the value of the National Scheme which increases proportionally with the value of BOD_5 as follows:

COD = 2.9 x BOD_5 to 89 g COD / inhab / day in 2030;

- **MES:** for MES, we adopted the values recommended in the National Scheme. The value of 27 g /hab /d is adopted for the year 2006, and 30 g / hab / d in 2020. This value corresponds to MES = 1x BOD_5.

TABLE 5
RESULTS OF THE GLOBAL WASTEWATER DISCHARGE OF OUAZZANE

	2006	2007	2008	2010	2015	2020	2025	2030	2035	2040	2048
WASTEWATER DISCHARGE											
DOMESTIC REJECTIONS											
POPULATIONS (inhabitant)	59255	59907	60566	61905	65386	69062	72945	77046	81378	85953	93815
Connection rate to the sewer %	91	91	91	92	93	95	96	97	97	98	98
Sewer return rate %	80	80	80	80	80	80	80	80	80	80	80
Domestic Rejection (m^3/d)	2718	2748	2777	2916	3113	3359	3585	3826	4042	4313	4707
ADMINISTRATIVE Rejection											
Sewer return rate %	80	80	80	80	80	80	80	80	80	80	80
Connection rate to the sewer %	100	100	100	100	100	100	100	100	100	100	100
Administrative Rejection (m^3/d)	284	288	291	297	314	331	350	370	391	413	450
Sewer return rate %	80	80	80	80	80	80	80	80	80	80	80
Connection rate to the sewer %	100	100	100	100	100	100	100	100	100	100	100
Industrial Rejection (m^3/d)	284	288	291	297	314	331	350	370	391	413	450
TOTAL REJECT (m^3/d)	2873	3324	3359	3510	3741	4021	4285	4566	4824	5139	5607

TABLE 6
RESULTS OF THE GLOBAL CONSUMPTION AND WASTEWATER DISCHARGE OF OUAZZANE

	2006	2007	2008	2010	2011	2012	2015	2017	2020	2025	2030	2035	2040
OUED REHA BASIN RABAT BASIN													
Totale Population EH	59152	59803	60461	61798	62478	63165	65273	66717	68943	72819	76913	81237	85805
Totale Consumption m^3/d	4436	4485	4535	4697	4748	4801	4961	5070	5340	5534	5845	6174	6521
Connection rate to the sewer %	91	91	91	92	92	92	93	94	95	96	97	97	98
Total population connected to the sewer EH	49994	54421	55020	56854	57479	58112	61093	63310	65906	70340	74835	79043	84089
Global specific flow DBO5 g / Eq.hab / d	27	27	27	28	28	28	29	29	30	30	30	30	30
Total Equivalent Inhabitants EH	59085	59715	60412	62316	63002	63695	67558	70387	72437	77238	81430	86008	91353
Overall average rate m^3/d	3281	3317	3353	3504	3543	3582	3735	3851	4015	4278	4558	4814	5129
Parasitic water level %	35	35	35	30	28	26	24	22	20	20	20	20	20
Average flow rate including parasitic water m^3/d	4429	4478	4527	4555	4535	4513	4631	4699	4818	5134	5470	5777	6155
// // // // L/s	51	52	52	53	52	52	54	54	56	59	63	67	71
Effluent charge of DBO5 kg/d	1440	1472	1489	1576	1593	1611	1739	1794	1962	2092	2234	2358	2531
// // // mg/L	325	329	329	346	351	357	375	382	407	407	408	408	411
EffluentCharge of DCO kg/d	4274	4368	4419	4679	4730	4782	5162	5327	5822	6210	6630	7000	7512
// // // // // mg/L	965	975	976	1027	1043	1060	1115	1134	1208	1210	1212	1212	1221
Effluent Charge of MES kg/d	1422	1453	1470	1557	1574	1591	1717	1772	1937	2066	2206	2329	2500
// // // // // mg/L	321	325	325	342	345	353	371	377	402	402	403	403	406

4.4 Dimensioning of the "Screening And Grit"

The sizing of the screening disposal is the same for most WWTPs. A coarse grid is provided for the discharge of sewage from the pipeline so that coarse material contained in the wastewater can be retained. It is recommended to use for this what is commonly called a cage grid.

In order to ensure operation that has the least possible problems, it is planned to distribute the effluent to be treated under normal operating conditions on two different paths. This will allow, in case of revision work on one of the grids, a certain screening of wastewater arriving at the treatment plant through the presence of a second grid. The two grilles will each be sized to support 50% of the maximum hydraulic load.

To avoid the occurrence of hydraulic problems in the event of a prolonged failure of a grid, it will be planned to set up parallel to the two grids a bypass. The spacing between the bars of the fine grids is generally between 5 mm and 20 mm. The smaller these distances, the greater the volume of materials retained.

Thus, the establishment of grids too fine makes the system more sensitive to mechanical failures caused by the jamming of solids. These considerations lead us to propose a screening chamber which will be equipped with a grid consisting of circular bars with a diameter of 10 mm, which will have an inclination of 1: 3 and a height of 0.8 m (**Table 7**).

Grid cleaning will be manual to avoid high operating and maintenance costs. To facilitate the continuous cleaning of the grids the screening chamber will have an access bridge equipped with a perforated channel. This channel will remove residues with a rake and evacuate the water in the channel screening. The collected residues are evacuated in a container ($1m^3$), which will be placed next to the screening chamber. The collected residues will be transported to the dump. It is proposed to size a manual screening unit, with manual cleaning (**Table 7**).

TABLE 7
CRITERIA OF DIMENSIONING OF SCREENING

Maximum speed of passage in rainy weather	<	2,0	m/s
Minimum speed of passage in dry weather	>	0,5	m/s
Guaranteed passing speeds required for a degree of clogging of the grid	=	25	%
Flow velocity in the approach and exit channels of the grid for Qph	>	0,5	m/s
Screening residues	=	env. 5	L/hab/a
Number of channels	1		
Type	Manual Cleaning		
Width	0,50	m	
Height	0,80	m	
Max hydraulic load	71	L/s	
Tilt of the bars	1 : 3		
Section of the bars	Circular		
Thickness of the bars	10	mm	
Spacing of the bars	12	mm	

The main function of the sand trap is to protect sand treatment facilities, so that sand deposit does not reduce the volume needed for effective treatment. In addition to this function, the grit eliminates the need to protect the pumps and other equipment from abrasion, thus significantly reducing maintenance costs.

The last important function is to allow a good separation of the sand and the organic matter in order to maintain the quantity of sand thus produced at a low level. This separation will avoid additional costs for the evacuation of large volumes of sand and will reduce the release of unpleasant odors associated with the evacuation of this material. However, a good separation of the organic and mineral fractions can be ensured in a grit chamber only by air insufflation. That's why we recommend the installation of a ventilated sand trap (**Table 8**).

The sand that settles in the grit chamber is driven by a scraper into the collecting hopper. The scraper moves with a scraper bridge mounted on rails. A mammoth pump sucks the sludge that settles into the hopper and drives it to a classifier. It is in the latter that the sand is separated from the water. This water is then reintroduced into the clarification process while the sand is led to a reservoir that must be emptied regularly.

TABLE 8
CRITERIA FOR SIZING THE GRIT/GREASE

Parameters		Value	Unit
Residence time for Q_{max}	>	5	min
Residence time for Q_{ph}	>	10	min
Horizontal speed in the grit chamber with Q_{max}	<	0,1	m/s
Specific energy for air insufflation	~	5	W/m³
Sand retained by the sand trap	~	0,06	L/m³
Dimensioning flow	=	71	L/s
Area	=	11	m^2
Length	=	5,64	m
Width	=	1,88	m

4.5 Dimensioing of Primary Decanter

The primary treatment with a circular decanter is intended to complete the removal of unwanted course materials by grit removal. The primary clarifier is sized on the basis of the dry point flow (Table 9). The settling lagoon has a circular geometry, the diameter is 16.00 m; the radius of 8.00 m and the depth of 3.00 m. The total volume is 602.88 m.

TABLE 9
CRITERIA OF DIMENSIONING OF PRIMARY DECANTER

	Unit	Q (m^3/h) Calculated Value	Value After correction
Débits	**Q (m3/d)** 7267	302,78	302,78
Taux de débordement	τ (m^3/ h / m^2)	1,5	1,33
Temps de rétention de l'eau dans le décanteur	tr (hour)	2	2
Depth	H (m)	3	3
Total Surface	S (m^2)	201,86	201
Diameter	D (m)	16,04	16
Ray	R (m)	8,02	8

4.6 Dimensioning of Lagoon Basins

For the "natural lagooning" process, there are numerous references and models for sizing basins without there finally being any that is universal. The most common sizing variant of the 3 types of ponds used in the natural lagoon system: anaerobic, optional, maturation.

4.6.1 Anaerobic Basins

These are settling basins with anaerobic conditions. Treatment consists mainly of sedimentation of suspended solids and partial digestion of readily biodegradable organic material. The volume of the pond is chosen large enough to ensure a storage of sludge of at least one year (**Table 10**). The residence time of the water must at least exceed the day, and the volume required for the deposit of sludge must be included. In addition, according to MARA [17] a volume load of 350 kg/m³ /d should not be exceeded to limit odor nuisance.

The pre-treated wastewater passes through the Venturi canal and will be distributed in the distribution zone on the two pipes that will bring the wastewater to the four anaerobic basins. The distribution system will be equipped with a cofferdam so that, in case of cleaning of an anaerobic basin, the effluent can be diverted to the other basins.

The basins will be rectangular in shape with a bottom length of 44.02 m with a slope of 1: 2 (V / H). The maximum length at the crest of the dike will be 60.02 m. In order to avoid overflows due to the wind, we reserve a freeboard of 0.5 m minimum. Feeding each basin will be provided by a DN250 pipe entering the basin at the first third of the depth, 2 meters below the water level. Communication from one basin to another will work through a look with a spillway (cofferdam) towards the connecting pipe to the proposed optional pond.

It is recommended to clean the ponds once a year that are to say to evacuate the sludge that has been decanted. Otherwise the additional volume of sludge will reduce the useful volume of the pond and the necessary retention time will no longer be respected. Then the sludge will be pumped off with a sludge pump and transported to the drying beds.

TABLE 10
SIZING CHARACTERISTICS OF ANAEROBIC BASINS

Parameters		Value	Unit
Volumic Load	=	30 - 300	$kg/m^3/d$
Depth	=	03-04	m
Residence time	=	03-05	day
Areal Load	=	1000	kg/ha/d
Number of basins		4	parallel basins
Dimensioning of basins at mirror		58,02 × 35,35	m
Depth of water		3,50	m
Minimum freeboard		0,50	m
Depth of basin		4,00	m
Basin Volume		8204,02	m^3
Interior slope		1 : 2	

4.6.2 Optional Basins

Wastewater treated in anaerobic basins is routed through DN 250 mm PVC pipes to two series structures that distribute the water to the entrances to optional lagoons. Like anaerobic basins, optional basins operate in parallel. The geometry of the lagoon aims to have a regular shape, the length is approximately 1.5 to 2 times the width (**Table 11**). The total depth of the basins is 2.00 m with a freeboard of 0.5 m. The dykes will have an inclination of 1: 2. The feeding of each basin will be done by a DN 250 pipe which returns to a height of 0.75 m compared to the coast of the bottom of the basin. The exit of the basin will be made through a dumping threshold formed of cofferdams. Thus, we will be able to adjust the water level in the basins. The cofferdams will be easily manipulated aluminum bars of height 5 cm.

TABLE 11
DIMENSIONING OF OPTIONAL BASINS

Parameters	Value	Unit
Number of basins	4	parallel basins
Dimensioning of each basin to mirror	106,84×192,31	m
Depth of Water	1,50	m
Basin Depth	2,00	m
Basin Volume	41092,8	m^3
Interior Slope	1:2	

4.6.3 Maturation/ Storage Basins

The maturation basins are shallow and aerobic basins whose role is the elimination of pathogens and will be used for the storage of treated wastewater for agricultural valorization. The sizing of these basins is summarized in **Table 11**. The wastewater treated in the optional basins passes through DN 250 mm pipes to four series of works which distribute the water to the inputs of the maturation lagoons. Like anaerobic and facultative basins, maturation basins operate in parallel.

The maturation lagoon has a rectangular geometry, the length is approximately 1.5 to 2 times the width. The total depth of the basins is 1.50 m with a freeboard of 0.50 m. The dikes will have a slope of 1: 2

TABLE 12
DIMENSIONING OF MATURATION LAGOON

Number of basins	4 parallel basins
Dimensioning of each basin to mirror	160.00 ×40.00 m
Depth of Water	1,00 m
Depth of Basin	1,50 m
Basin Volume	6400
Interior Slope	1:2

4.7 Drying Beds

The sludge will be dehydrated on drying beds corresponding to the usual methods in Morocco. Drying beds made of concrete with layers of gravel and sand are recommended. This configuration allows sufficient dewatering of the sludge which can then be used in agriculture. The beds will be provided with perforated PVC drainage pipes (DN 150) with 3/4 openings.

The pipes are laid in drain trenches and surrounded by gravel. The drainage pipes lead the dirty infiltrated water towards a DN 250 pipe, which brings them back gravity to the distributor upstream of the anaerobic basins. The number of drying beds was determined according to the interval and frequency of cleaning.

TABLE 10
DIMENSIONING OF DRYING BEDS

Parameters		Value	Unit
Quantity of sludge per drain		2993	m^3
Depth of beds		0,6	m
Length of beds		25	m
Width of the beds		10	m
Total number of beds		30	

V. CONCLUSION

When using an extensive process such as natural lagooning, the quantities of sludge produced are less than in the case of the use of an intensive process. However, sludge is not removed continuously but periodically. This is why we need to build important infrastructures for the evacuation of sludge. These infrastructures are not used regularly but must be maintained, they occupy space and require investments.

Natural lagooning requires the installation of very important infrastructures as well as the reasonable investment cost. Nevertheless it requires little maintenance and few qualified personnel compared to the bacterial bed and activated sludge. This process gives a very good robustness and reliability of treatment in addition it presents olfactory nuisance (smell), considerably in summer because of the presence of the wind Chergui having the direction of the EST towards the West).

According to the multi-criteria comparison of the available variants, it seems that lagooning is the most appropriate method for the treatment of wastewater from the city of Ouazzane.

REFERENCES

[1] Ministère de l'Intérieur et Ministère de l'Aménagement du Territoire, de l'Eau et de l'Environnement du Maroc. ''Programme National d'Assainissement Liquide et d'Epuration des eaux usées''. 2005.

[2] R. Medioni, ''L'oeuvre des géologues français au Maroc", Travaux du Comité français d'Histoire de la Géologie, Comité français d'Histoire de la Géologie, 2011, 3eme série (tome 25, 1), pp.1-52.

[3] Ministère de l'Intérieur, ''Monographie Générale de la région de Tanger, Tétouan et Al Hoceima," Rapport, 2015.

[4] R. Bourrier, ''Les réseaux d'assainissement," Tec . et Doc. Lavoisier, Paris, 1991.

[5] J. Rodier, ''L'analyse de l'eau naturelle, eaux résiduaires, eau de mer,'' 8éme édition, *Denod*, Paris, 1383p.

[6] J. Degrément, ''Mémento Technique de l'eau," huitième édition, 1978.

[7] W.W. Eckenfelder, "Gestion des eaux usées urbaines et industrielles," Technique et documentation Lavoisier, 503p. 1982.

[8] A. Shilton, ''Pond Treatment Technology," Edited by Iwa Publishing London Seatle.

[9] A.I. Caquot. ''Ecoulement des eaux pluviales," CR Acad. Sc. Paris, 1941.

[10] E.F. Gloyna, "Basis for waste stabilization pond designs," Advance in water quality improvement, water resources symposium. N°1, p379. University of Texas Austin.

[11] CEREMEHER, ''Optimisation du procédé d'épuration par lagunage sous climat tropical, expérimentation sur la station de Saint Louis,'' Rapport Final 1994 SIVOM R/ CEREMHER.

[12] D.D. Mara and H.W. Pearson,''Waste stabilization ponds: Design manual for Mediterranean Europe,'' World Health Organisation. 1987, 53 pages.

[13] M.G. McGarry and M.B. Pescod, ''Stabilization pond design criteria for tropical Asia,'' In proceeding of the Second International symposium for waste treatment lagoons. Edited by RE McKenney Laurence. University of Kansas, 1970, pp: 114-132.

[14] G. Marais,''Faecal Bacterial Kenitics in stabilization ponds,'' ASCE. J. EE Div. Vol. 100. 1974.

[15] R. Demillac and D. Burton, ‘‘Inactivation compare des virus hydriques et bacteries indicatrices de la contamination fécale en basins de lagunage,’’ Rennes Ecole Nationale de la santé publique. 1982.

[16] ONEP, ‘‘The typology approach of Moroccan wastewaters,’’ Moroccan German Technical cooperation, National Office of Drinking Water. ONEP/GTZ. 1998.

[17] D. Duncun Mara, ‘‘Domestic wastewater treatment in developing countries,’’ EarthScan. ISBN 1-84407-019-0. London. 1987.

Investigation of the surface morphology of ASD-4 powder, modified by V_2O_5

V.G. Shevchenko[1], D.A. Eselevich[2], N.A. Popov[3], D.K. Kuznetsov[4], V.Ya. Shur[5]

[1,2,3]Institute of Solid State Chemistry UB RAS, Ekaterinburg, Russia
[4,5]Institute of Natural Sciences and Mathematics UFU, Ekaterinburg, Russia

Abstract**—** *The changes in the surface layer of aluminum particles treated with V2O5 • nH2O hydrogel were studied by ellipsometry and raster electron microscopy methods. It was shown that at 0.8 wt.% content of metallic vanadium in the modified powder, the particle surface layer has a well developed relief, and a high degree of impregnation is achieved. The values of the thickness of this layer measured by different methods were compared, and the obtained deviations were analyzed.*

Keywords**— aluminum powder, surface modification, vanadium pentoxide, microscopy, ellipsometry.**

I. INTRODUCTION

The use of vanadium oxides for improving the combustion of metal powders has been studied for many years [1-4]. Due to vanadium polyvalence, a large amount of oxides and other compounds formed during its oxidation makes this metal a good oxygen carrier to the reaction zone. Being the most demanded material in this field, vanadium oxide (V) in itself is a strong oxidant and has a melting point close to aluminum, which promotes its use as an additive reducing the ignition temperature and increasing the speed and heat of combustion of powder aluminum. In the liquid state, vanadium pentoxide, due to a low surface tension [5], penetrates into the pores and cracks of the oxide film on the surface of aluminum particles [1, 6, 7], promoting active oxidation of aluminum with simultaneous formation of $AlVO_4$. The application of $V_2O_5 \cdot nH_2O$ gel on the surface of aluminum powders of the ASD-4 type [8] significantly increases their specific surface, without changing the shape of the metallic particles, which positively affects their rheological properties [6]. We have established that the aluminum powders modified with $V_2O_5 \cdot nH_2O$, $Na_2V_{12}O_{31} \cdot nH_2O$, $LiV_{12}O_{31} \cdot nH_2O$, $Na_2MoV_{11}O_{31} \cdot nH_2O$ and $6V_2O_5 \cdot B_2O_3 \cdot nH_2O$ had twice as large specific surface area as the initial ASD-4, a high storage stability and, according to thermogravimetric data, a high oxidation efficiency in air [6, 7]. It is known [2, 9, 10] that during dehydration of gels the obtained xerogels have a quasi-two-dimensional (2D) layered structure that is easily intercalated at room temperature by metal ions, molecules of organic solvents, organometallic complexes and other compounds. However, the characteristics of the modified powder surface, the geometric parameters of the oxide and modifying layers, the structure and stability of the modified layer remain unknown. Thus, the main aim of the present work is a more detailed study of the morphology, thickness of the oxide and modifying layers in the initial and modified particles of aluminum powder, as well as the stability of the modified layer during heating to the temperature close to the aluminum melting point.

II. EXPERIMENTAL

Aluminum powder ASD-4 with a specific surface area of 0.4 m^2/g was used in the study. The hydrogel $V_2O_5 \cdot nH_2O$ was synthesized by thermohydrolysis of V_2O_5 by pouring the melt into a heat-resistant beaker with intensively stirred distilled water [6]. To increase the vanadium content, the resulting hydrogel was concentrated by evaporation in a water bath. This allowed the samples with ~0.8 wt. % V content to be obtained by single impregnation of the gel.

The thickness of the oxide films on the surface of initial ASD-4 powder and the powder modified with vanadium pentoxide at room temperature in air was estimated using ellipsometry (ellipsometer LEF-3M, $\lambda = 0.638$ nm, angle of incidence $\varphi = 45°$). For the experiments, the powders were compacted in the form of tablets by pressing under pressure p = 29.4 MPa. The compressed tablets had a flat mirror surface. The surface of aluminum powders was shown with the use of electron microscopy. Using a focused ion beam of gallium, the powder particles were cut in a workstation AURIGA CrossBeam (Carl Zeiss, Germany) in vacuum to obtain a picture of their cross section. The beam current was 16 nA at an accelerating voltage of 30 kV. Delicate surface etching was carried out at an accelerating voltage of 30 kV and an ion beam current of 240 pA. The specific surface of the powders was evaluated by the low-temperature nitrogen desorption method (BET method) using a TriStar 3000 automatic analyzer (Micrometrics, USA).

III. RESULTS AND DISCUSSION

The specific surface area of ASD-4 powder after treatment with $V_2O_5 \cdot nH_2O$ gel increased two-fold and amounted to 0.873 m^2/g. Figure 1 shows the general view of a particle of the modified powder cut by ion beam; the surface of neighboring modified particles is also visible. It can be seen that the relief is highly developed and meshy. This provides an increased specific surface area of the particles, with their sphericity being preserved. The above-mentioned improvement in the flow rate of the powder is due, in our opinion, to the lack of moisture absorption by vanadium pentoxide and to the aggregation of metal powder particles during mixing with the hydrogel.

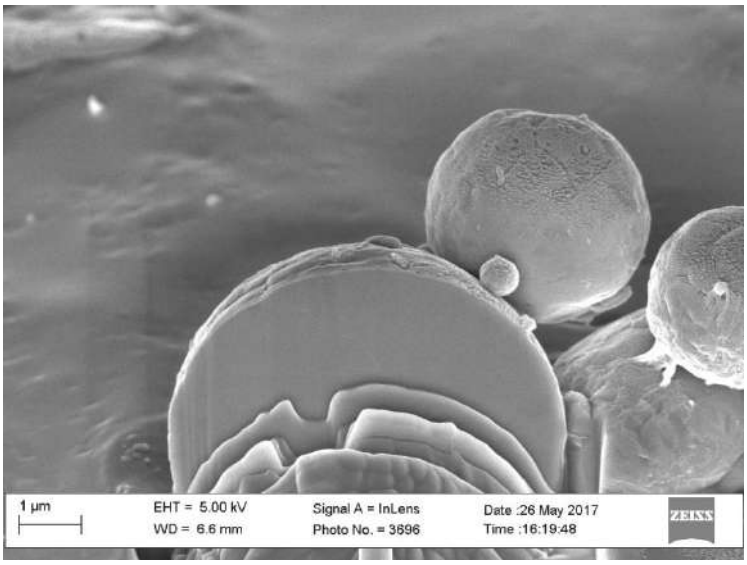

FIG. 1. Electron microscopic images of ASD-4 powder after impregnation with $V_2O_5 \cdot nH_2O$ gel

X-ray phase analysis using synchrotron radiation at the station of channel 4 of the Shared-Use Center "Siberian Synchrotron and Terahertz Radiation Center (SSTRC)" based on VEPP-3 of BINP SB RAS showed that the impregnation of the powder with vanadium pentoxide in the form of a gel does not lead to a variation in the chemical composition of the sample: besides the Al and Al_2O_3 peaks, invariably present on the X-ray patterns of ASD-4, there are weak signals from V_2O_5. The presence of a vanadium pentoxide xerogel in the modified layer is also confirmed by the IR spectra, where the bands at 1010-1005, 770-750 and 510-505 cm^{-1} are observed, which correspond to the frequencies of V-O bond vibrations in the structure of V_2O_5. nH_2O xerogels [6].

Figure 2 shows a cross-sectional view of a particle of the initial ASD-4 powder obtained by a high-resolution electron microscope provided with an ion beam.

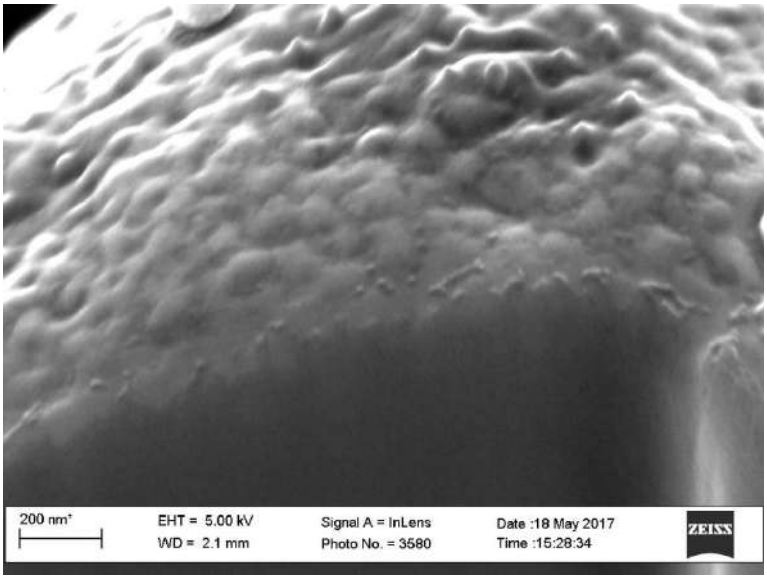

FIG. 2. A cross section of a particle of the initial ASD-4 powder

The upper part of the photomicrograph shows the particle surface relief, the lower part - a smooth ion beam cut deep into the particle interior. A lighter shade of the particle surface is due to the presence of a passivating oxide layer of Al_2O_3. However, due to hardware limitations, it was not possible to clearly distinguish the boundaries between the metal core and the oxide layer and to estimate the oxide layer thickness.

Figure 3 (a, b) displays a cross-section of a particle of modified ASD-4 powder. In this case, the surface film is seen more clearly, its average thickness is about 40 nm. The better contrast is due, first of all, to a larger thickness of the modified layer compared to the passivating film on the original ASD-4. Filming was also carried out in secondary electrons, and a lighter shade of the surface layer means that emission of secondary electrons from the surface layer is higher than from the aluminum core. The secondary electron emission coefficient for dielectric materials is higher than for conductors. An additional contribution to the emission is made by the backward reflected electrons, which, in turn, generate secondary electrons. Since the coefficient of electron reflection increases with increasing atomic number, it is possible in theory to see a varition in the light intensity as a function of the concentration of elements in depth. However, in the presented photographs this gradient is expressed very weakly, and for its detection a greater magnification and point chemical analysis (EDX) are required. The absence of a color intensity gradient in the film depth indicates the incorporation of aluminum and oxygen atoms into the crystal structure of the xerogel during ion etching.

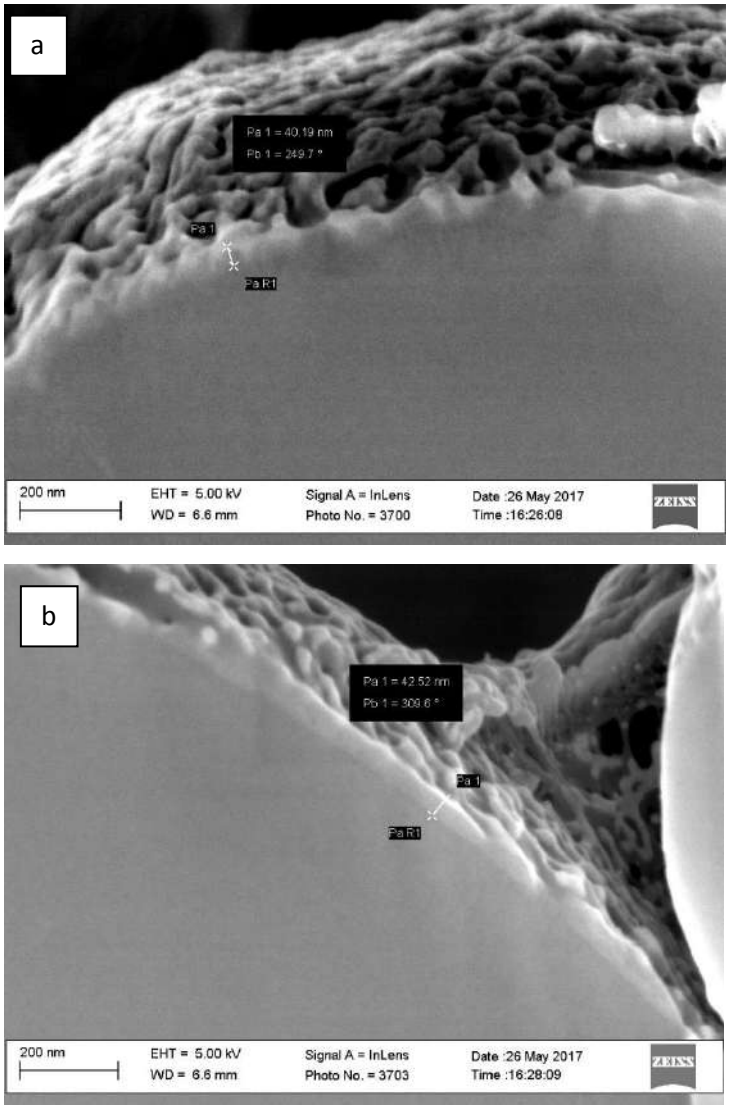

FIG. 3. A cross section of a particle of ASD-4 powder modified by vanadium hydrogel

Figure 3 (a, b) shows that the modified surface has a much more developed net-like relief than the original aluminum powder (Fig. 2). The formation of such a structure can be due to removal of water molecules during xerogel drying and to fixation of

the xerogel on the oxide film surface defects. Note also a rather firm adherence of the modified layer to the metallic core, which may also indicate the possibility of intercalation of the xerogel by aluminum ions.

The thickness of the surface layers on the powders was estimated by the ellipsometry method according to the procedure described elsewhere [11]. The object of investigation in this case was the surface of tablets obtained by pressing the investigated powders. The experimental data were processed using a modified nomogram Δ-ψ, intended for the calculation of the thickness (d) and the volume fraction of metal (q) in the powders during their oxidation. The horizontal lines on this nomogram (Fig. 4) correspond to the lines of equal oxide thickness, and the vertical lines – to the corresponding values of q. If the refractive indices of the components of the medium are known - in this case the metal and the oxide (n_{ox} and $N_2=n_{met} - ik_{met}$), then the relationship between them and their volume fractions is expressed by the Maxwell-Garnett equation for the polarizability of molecules [12]:

$$\frac{n^2-1}{n^2+2}=q\frac{n_1^2-1}{n_1^2+2}+(1-q)\frac{N_2^2-1}{N_2^2+2} \quad (1)$$

where q is the volume fraction of metal, (1-q) is the volume fraction of oxide; n is the refractive index of compressed powder (tablet); n_1 is the refractive index of oxide; $N_2=n_{met}-ik_{met}$ is the refractive index of metal (aluminum); *i* is the imaginary unit of a complex number; and k_{met} is the absorption coefficient of metal. By plotting the experimental points on the calculated nomogram, the thickness and volume fraction of metal in the tablet can be determined.

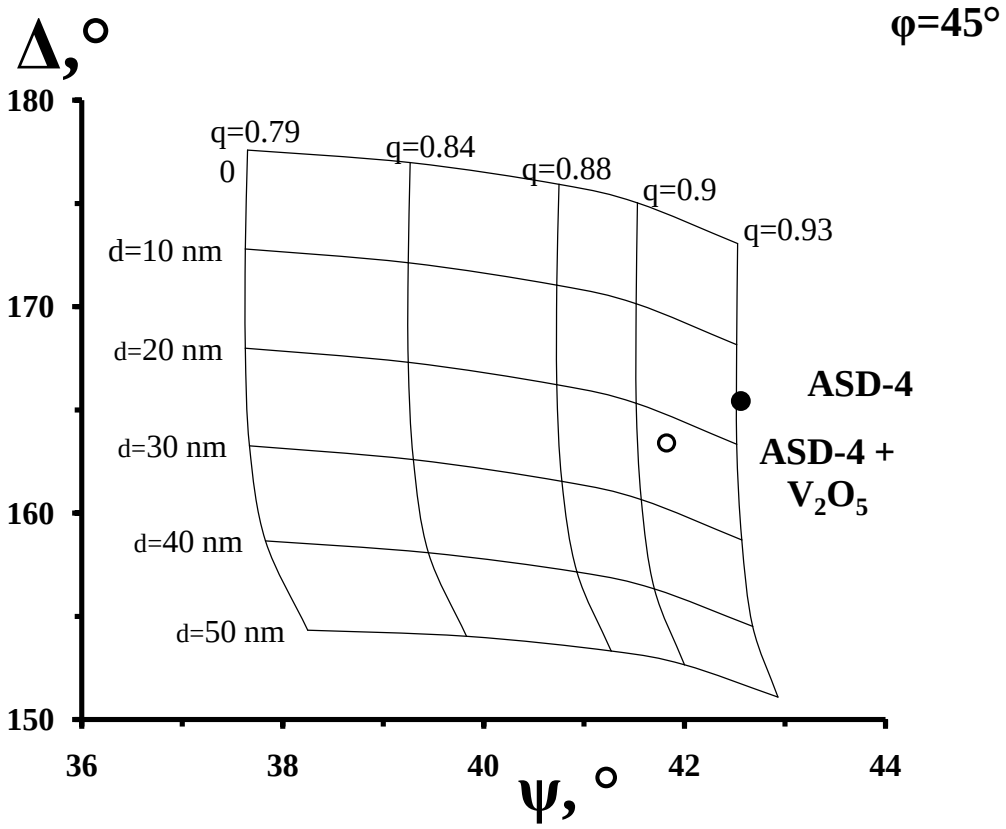

FIG. 4. The nomogram Δ-ψ for determining the thickness of the oxide film and the metal fraction in the compacted powder during oxidation, the angle of beam incidence is φ = 45°

Thus, for the initial ASD-4 powder, the average thickness of the oxide film was 16 ± 5 nm, which is in good agreement with the literature data [13], where the average thickness of the oxide film of ASD-4 particles is 17.9 nm. For ASD-4 + V_2O_5 powder, the average thickness of the modified layer (oxide + V_2O_5) was slightly higher, ~24 ± 5 nm. From formula (1) it is seen that only refractive indices of aluminum (n_{Al} = 1.65) and aluminum oxide (n_{Al2O3} = 1.6) were taken into account in the calculation of the nomogram, while the optical constants of the xerogel V_2O_5 and the porosity of the tablet were disregarded to simplify the calculations. In this connection, there is a certain error in determining the values of d and q for the modified

powder. However, this method makes it possible to reliably retrace the oxidation kinetics of the modified powder and compare this process with the oxidation of initial ASD-4.

Based on the geometric characteristics of the ASD-4 particles [13], the densities of aluminum, Al_2O_3 and V_2O_5 oxides (ρ = 2.7, 3.99, 3.357 g/cm^3, respectively) and also assuming that the layer of $V_2O_5 \cdot nH_2O$ xerogel is the outer shell covering the ASD-4 particle and not interacting with it, it is possible to calculate the thickness of this shell if the content of metallic vanadium in the modified powder is 0.8 wt.%. Ideally, the thickness of this shell is equal to:

$$d_{V_2O_5} = \sqrt[3]{\frac{3(V_{ASD-4} + \frac{m_{V_2O_5}}{\rho_{V_2O_5}})}{4\pi}} - r_{ASD-4} = 19.4nm, \quad (2)$$

where V_{ACD-4}, r_{ACD-4} are the volume and the radius of ASD-4 particle, and mV_2O_5 is the mass of the xerogel shell calculated from the molar mass of the oxide and the mass content of vanadium in the sample.

Hence, the total thickness of the modified layer will be 35-37 nm, which is close to the value obtained by electron microscopy (40 nm). However, as seen from the microphotographs (Fig. 3), the real surface of the modified particles has a much more complex relief, which allows us to speak of some effective thickness of the modified layer.

It should be noted that ellipsometric measurements were carried out on compressed powders, where the core and the surface film of the particles are mechanically deformed. In this connection, such geometric parameters as the average thickness of the surface film of pressed particles may differ from freely poured powder.

Thus, the obtained data on the surface of modified powders are indicative of the formation of a layer with a well-developed nanorelief and high adhesion caused by the possibility of intercalation of vanadium oxide xerogel with aluminum ions, its thickness is within 24-40 nm. These factors provide the powder with a combination of high rheological characteristics, storage stability in air and at the same time high energy characteristics due to close contact of the modifier with the particle surface.

IV. CONCLUSION

Using ellipsometry, microscopy and elemental analysis, it was shown that the samples, obtained by impregnation of aluminum powder with vanadium-containing hydrogel, after drying and calcination at 623 K in air represent a system, in which the deposited gel forms a nanosize layer impregnated with $V_2O_5 \cdot nH_2O$ on the particle surface. If the content of metallic vanadium in the modified powder is 0.8 wt. %, the surface layer is characterized by a highly developed relief with good adhesion due to the chemical bonding of the modifier with the surface of aluminum particles owing to the intercalation of aluminum ions in the xerogel structure.

The work was carried out in accordance with the state assignment and R&D plans of the Institute of Solid State Chemistry of the Urals Branch of the Russian Academy of Sciences (No. AAA-A16-116122810219-4).

REFERENCES

[1] L.D. Romodanova, P.F. Pokhil, E.S. Kadaner. On the mechanism of action of V_2O_5 additive on the burning rate of compositions based on ammonium perchlorate and metallic combustibles. // Fizika goreniya i vzryva (Physics of Combustion and Explosion). - 1968. - V. 3. - P. 330-333. [in Russian]

[2] Volkov, V.L. Interstitial phases based on vanadium oxides / V.L. Volkov. - Sverdlovsk: UNTs AN SSSR. - 1987. - 180 p. [in Russian]

[3] V.G. Shevchenko, V.L. Volkov, V.I. Kononenko [et al.]. Influence of sodium and potassium polyvinadates on the process of oxidation of aluminum powder // Combustion, Explosion, and Shock Waves). - 1996. - Vol. 32. - P. 91-94. [in Russian]

[4] Sharipova, N.S., Ksandopulo G.I. Phase and structure transformations and mechanism of propagation of self-propagating high-temperature synthesis in V_2O_5-Al mixture // Combustion, Explosion, and Shock Waves. - 1997. - Vol. 33. - P. 659-668.

[5] Physico-chemical properties of oxides. Reference book / G.V. Samsonov, A.L. Borisova. T.G. Zhidkova [et al.]. - Moscow: Metallurgiya. - 1978. - 472 p. [in Russian]

[6] Effect of vanadium-containing activating additives on the oxidation of aluminum powders/ Shevchenko V.G., Eselevich D.A., Konyukova A.V., Krasilnikov V.N. // Russian Journal of Physical Chemistry B. - 2014. – V. 8. - № 5. – PP. 634-640.

[7] Effect V_2O_5 on the oxidation mechanism of ASD-4 powder / Shevchenko V.G., Krasilnikov V.N., Eselevich D.A. [et al.] // Combustion, Explosion, and Shock Waves. - 2015. – V. 51. – № 5. – P. 572-577.

[8] RU Patent No. 2509790. Method of activation of aluminum powder / V.G. Shevchenko, D.A. Eselevich, A.V. Konyukova, V.N. Krasilnikov. Published on 03/20/2014. [in Russian]

[9] Intercalation of conducting poly (N-propane sulfonic acid aniline) in V2O5 xerogel / Zhao J., Wang G., Li X., Li C. // J. Appl. Polymer Sci, 2007. - V. 103. - P. 2569-2574.

[10] Synthesis and characterization of sodium vanadium oxide gels: the effects of water (n) and sodium (x) content on the electrochemistry of NaxV2O5*nH2O / Lee C. Y., Marschilok A. C., Subramanian A., Takeuchi K. J., Takeuchi E. S. // Phys. Chem. Chem. Phys. - 2011. - V. 13. - P. 18047-18054.

[11] Pu Patent No. 2463554. A method for determining the thickness of a thin transparent film / L.A. Akashev, V.G. Shevchenko, V.A. Kochedykov, N.A. Popov. - Published on 10.10.12. [in Russian]

[12] Ioffe, B.V. Refractometric methods in chemistry / B.V. Ioffe - Leningrad: Khimiya, Leningradskoe otdelenie. - 1983. - 352 p. [in Russian]

[13] Combustion of metal nanopowders / Gromov A.A., Khabas T.A., Il'in A.P. [et al.]. Ed. A.A. Gromov. - Tomsk: Deltaplan. - 2008. - 382 p. [in Russian].

Determining Important Grade of Environmental Risk Factors at Slopes

Baki Bagriacik[1], Hakan Guneyli[2], Suleyman Karahan[3]

[1]Department of Civil Engineering, Cukurova University, TURKEY
[2,3]Department of Geology Engineering, Cukurova University, TURKEY

Abstract— *Both, natural and man-made slopes formed for various purposes may cause numerous permanent problems in engineering applications. Therefore, it is important to know composition and mechanical behavior of soil environment leading to geotechnical problems on slope surfaces. The risk analyzes of natural and artificial slopes, realized detailed, can lead to reliable results. Based on those results, it is possible to produce optimal technical solutions with respect to an acceptable risk level. The researches on these subjects give new opportunities to improve the existing knowledge by reviewing them. The main aim of this study is objectively to evaluate the parameters caused slope stability problems. In this regard, the parameters of slope angle, internal friction angle and cohesion of soil, and groundwater level, which are main risk factors for a slope, and should contribute to raise awareness about this issue, were investigated.*

Keywords— Factor of safety, risk factors, slope stability.

I. INTRODUCTION

Surfaces that are oriented horizontally at a certain angle are defined as slopes. If angle of earth surface is great enough, soil moves downward due to gravity. Thus, slope loses its stability and this event caused an environmental risk situation. In order to assess the environmental risk of slopes, it is necessary to know the safety factor of natural slopes, on which are frequently encountered in the natural ear surface, excavation slopes and slopes compacted as controlled against landslide. The all factors affecting displacements need to be considered for a slope, which the environmental risk ratio (slope safety) will be determined. The safety of soil structure is often defined by a parameter called the safety factor (the environmental risk factor). This parameter can be described as the ratio of strength of soil to the load applied to it. Since this is a mathematical term, which represents the stability of the structure examined, this ratio varies based on the shear strength and stresses examined in the slope stability. A number of safety factor (environmental risk factor) definitions are available in engineering literature. The safety factor is a ratio of resistive forces along the sea surface to the shear forces; of the existing shear strength of soil along the potential shear surface to the mean shear stresses; and is a factor that the shear strength parameters decrease to maintain slope at limit equilibrium condition along a specific shear surface. For complete stability of a soil depending on these descriptions mentioned above, the safety factor F is defined as:

SF=available shear strength/shear stress required for equilibrium

It is stated that the minimum value of the safety factor given as a basic formula above should be 1.0 on a sliding surface not only for fail but also for stable condition. In following years, lots of studies on both analyzes of slope and their movement characteristics were conducted (Bishop [1]; Spencer [2]; Spencer [3]; Maksimovic [4]; Ching and Fredlund [5]; Fredlund [6]; Brinkgreve and Bakker [7]; Duncan [8]; Griffiths and Lane [9]; Cheng [10]; Hammah and diğ. [11]; Cheng and Lansivaara [12]). The main objective of many studies in the literature on slopes is to obtain economical and safe solutions to avoid an environmental risk (an adequate safety factor value) in ground structure, excavations and fills. The slope-based environmental risk studies on this subject cover a detailed investigation of the environment, material on the environment and economical parameters. In recent years, slope stability analysis has gained importance due to rapid population growth, increase of motorways based on technological development, dams, and deep and large excavation.

The finite element method was developed for stress analysis of aircraft bodies in 1956 and has later been started to use in solution of engineering problems in the following years. This method has been developed rapidly over the years, and used in many engineering applications. Numerical analyzes are effective mathematical methods used to solve complex engineering problems. The finite element method the most commonly utilized among the numerical analysis methods is one of the mathematical methods. In this method, the engineering problems can be solved by dividing the continuous environment into various geometric subspaces called the finite element. The finite element method is a numerical analysis technique widely used in many engineering applications both for research and in design (Köksal, [13]).Since the stress analysis in soil mass is approximation in conventional slope stability analysis, calculation has some difficulties for different loading conditions and

geometries. The finite element method has increasingly been used in slope stability analysis with the spread of computer use in engineering as well as in all areas. The advantage of finite element approach over the other conventional limit equilibrium methods is that there is no need for an assumption for the location and shape of slide (shear) surface, and properties and orientations of the slices. The finite element method as with two or three dimensions can be applied to all types of failure mechanism in complex slope geometries and conditions of various soil boundary and loading. It is possible to obtain the knowledge of material structure behavior in close to present conditions, and of accurately stress and replacements in soil. Moreover, the method can be used easily in long and short stability analyzes, and in conditions of slope reinforcement by materials such as geotextile or soil nail, and availability of ground water.

II. MATERIAL AND METHOD

In this study, numerical analysis by using finite element method (Plaxis 2D) [14]were carried out in order to investigate the effect of parameters of cohesion, internal friction angle, slope angle and groundwater level on the slope failure mechanism in sloped areas. Therefore, two-dimensional analyses using finite element method were performed by considering plane strain state. The finite element model used in analyzes is presented in Figure 1.

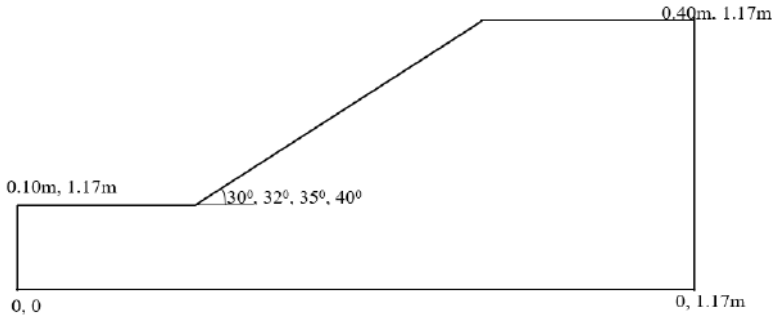

FIGURE 1. THE MODEL OF FINITE ELEMENT USED IN THE ANALYZES

In this context, MC (Mohr-Coulomb) soil model, which can model elasto-full (complete) plastic soil behavior and is widely available in the literature, was selected. MC model contains five different parameters of elasticity modulus (E), Poisson ratio (v), cohesion (c), internal friction angle (ϕ) and dilation angle (ψ). In addition, advanced parameters such as Eincrement and cincrement are also included in the model. The analyzes were carried out by choosing the most fine mesh selected from the five different mesh types in Plaxis 2D software.

III. FINDINGS AND DISCUSSION

In the study, the results of analyzes using the finite element method to determine the effect of the parameters such as slope angle, internal friction angle and cohesion of soil, and groundwater level on the safety factor (environmental risk factor) of a slope are presented below.

3.1 Influence of Slope Angle

Analyzes performed by the finite element method were also conducted to investigate the effect of slope angle change on the safety factor of a slope. Internal friction angle (ϕ=350), unite weight (γ=17.2 kN/m^3), cohesion (c=0.01 kN/m^2), elasticity modulus (E=24000 kN/m^2), poisson ratio (v=0.20) as constant parameters, and slope angle (β) values ranging from 300 to 400 as variable parameter were selected in the calculations. The determined results of the safety factors (environmental risk factors) vs. the slope angle values are seen in Figure 2 and Table 1.

TABLE 1
THE VALUES OF THE SAFETY FACTORS

Slope Angle, β	Safety Factor
Model 1. β=30°	1.270
Model 2. β=32°	1.192
Model 3. β=35°	1.022
Model 4. β=40°	0.914

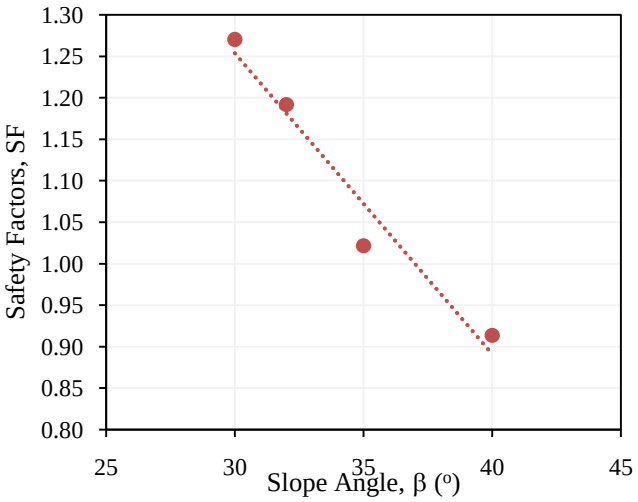

FIGURE 2. THE VALUES OF THE SAFETY FACTORS FOR SLOPE ANGLE

As a result, it was determined that the safety against landslide (failure) decreases due to the increase of slope angle, and obtained a strong (R=0.98) relationship between the slope angle and the safety factor. The data from the analyzes by the finite element method indicate that an increase in slope angle of 100 causes an decreases in the safety factor as per 28%, and thus it has been emphasized analytically that the slope angle change is very important parameter in terms of the slope stability.

3.2 Influence of Internal Friction Angle

Analyzes based on the finite element method were also carried out in order to evaluate the effect of internal friction angle change on the safety factor of a slope. The soil model parameters used in the analyzes were selected as constant values of slope angle ($\beta=30^0$), unite weight ($\gamma=17.2$ kN/m^3), cohesion ($c=0.01$ kN/m^2), elasticity modulus (E=ranging from 22000 to 28000 kN/m^2), poisson ratio (v=0.20), and as the variable parameter of internal friction angle (ϕ) values ranging from 30^0 to 43^0. The results obtained from these analyzes are seen in Figure 3 and Table 2.

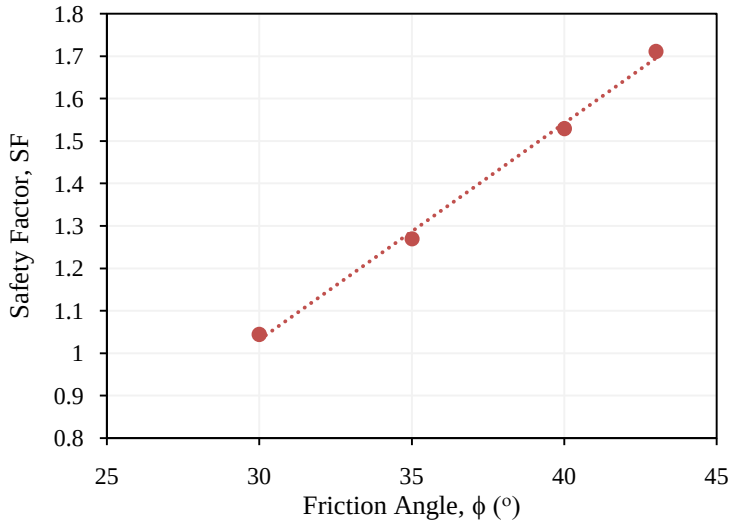

FIGURE 3. THE VALUES OF THE SAFETY FACTORS FOR FRICTION ANGLE

TABLE 2
THE VALUES OF THE SAFETY FACTORS FOR FRICTION ANGLE

Friction Angle, ϕ	Elasticity modulus	Safety Factor
Model 1. ϕ=30°	22000 kN/m^2	1.044
Model 2. ϕ=35°	24000 kN/m^2	1.270
Model 3. ϕ=40°	26000 kN/m^2	1.529
Model 4. ϕ=43°	28000 kN/m^2	1.711

The results from the analyzes by the finite element method indicate that the increase of internal friction angle increases the safety against sliding (failure) of slope, and the relationship between the internal friction angle and the safety factor has a strong (R=0.99) correlation coefficient. It was also found that an increase in internal friction angle of 43^0 at a constant slope angle leads an increase in the safety factor as per 39%. On the other hand, the degree of importance of internal friction angle for slope stability analyzes was revealed as well.

3.3 Influence of Cohesion

Analyzes made using the finite element method were conducted to assess the effect of cohesion change on the safety factor of a slope, as well. Internal friction angle (Φ=10), slope angle (β=32^0), unite weight (γ=17.2 kN/m^3), elasticity modulus (E=24000 kN/m^2), poisson ratio (v=0.20) as constant parameters, and cohesion values ranging from 0.500 to 1.500 kN/m^2 as variable parameter were selected in the calculations. The determined safety factor (environmental risk factor) values depending on cohesion values of a soil are shown in Figure 4 and Table 3.

TABLE 3
THE VALUES OF THE SAFETY FACTORS FOR COHESION

Finite Element Method, c (kN/m^2)	Safety Factor
c=0.500	0.624
c=0.625	0.764
c=0.750	0.901
c=0.780	0.932
c=0.820	0.976
c=0.850	1.006
c=0.875	1.036
c=1.000	1.173
c=1.125	1.312
c=1.250	1.720
c=1.500	2.200

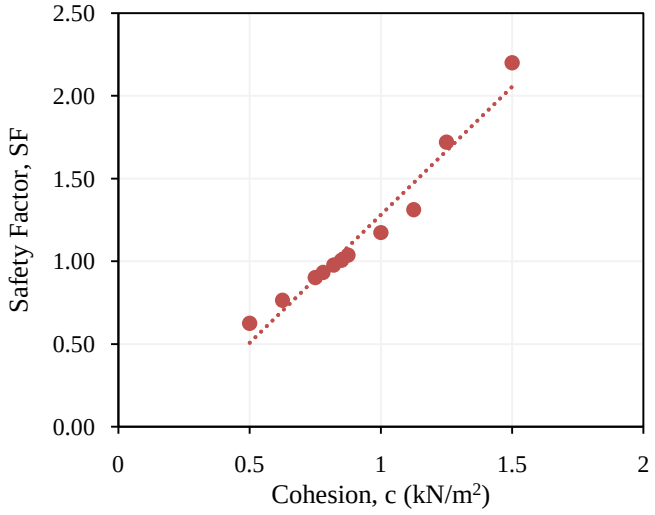

FIGURE 4. THE VALUES OF THE SAFETY FACTORS FOR COHESION

As a result of the analyzes, it was exhibited that the safety factor increases depending on increasing of cohesion of soil, and was acquired a strong (R=0.98) relationship between the cohesion and the safety factor. The data from the analyzes by the finite element method point out that an increase in cohesion value of 1 kN/m^2 leads an enhancement in the safety factor as per 72%. Moreover, it was revealed from the analyzes that how cohesion of soil forming slope affected stability of slope.

3.4 Influence of Groundwater Level

Analyzes performed by the finite element method were also conducted to investigate the effect of groundwater level change on the safety factor of a slope. Internal friction angle (ϕ=10), slope angle (β=32^0), and unite weight (γ=17.2kN/m^3), cohesion (c=0.85kN/m^2), elasticity modulus (E=24000 kN/m^2), poisson ratio (v=0.20) as constant parameters, and groundwater level

values ranging from 0 to 0.45 m as variable parameter were selected in the calculations. The determined results of the safety factors (environmental risk factors) vs. the groundwater level values are seen in Figure 5 and Table 4.

TABLE 4
THE VALUES OF THE SAFETY FACTORS FOR WATER GROUND LEVEL

Water Ground Level (m)	Safety Factor
0	1.006
0.05	1.002
0.10	1.000
0.15	1.000
0.20	1.044
0.25	1.134
0.30	1.275
0.35	1.492
0.40	1.822
0.45	2.312

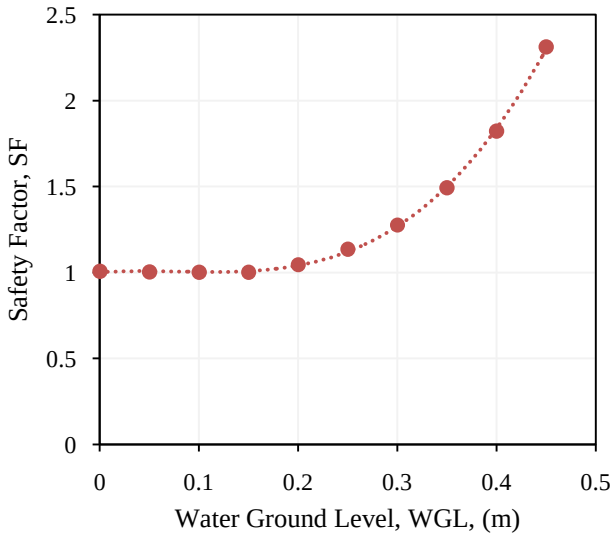

FIGURE 4. THE VALUES OF THE SAFETY FACTORS FOR WATER GROUND LEVEL

There is an asymptotic negative relationship with a strong correlation coefficient between the groundwater level and the safety factor according to the analyzes. While a significant change in safety factor does not occur at depth of the groundwater level from 0 to 0.2m, the deepening of groundwater level from 0.2m leads to an increase in the safety factor at much larger values.

IV. CONCLUSION

Series of numerical analysis by using finite element method (Plaxis 2D) [14] were performed to investigate the effect of a change of cohesion, internal friction angle, slope angle and groundwater level on the safety factor of slope failures. From the data and assessments presented in this paper the following conclusions can be drawn:

Based on increasing of slope angle, the safety of slope against landslide (failure of slope) decreases. An increasing in the slope angle of range from 30 to 400 leads to an average 28% reduction in the safety factor.

It was determined that the safety of slope against to failure decreases depending on the increment of the internal friction angle. An increase of the internal friction angle ranging from 30^0 to 43^0 causes an increment in the safety factor as per 39%.

The enhancement of cohesion value of soil forming a slope causes significantly the safety of slope against to failure. An increase of the cohesion ranging from 0.500 to 1.500 kN/m2 leads to an increment in the safety factor as per 72%.

In case of lowering groundwater level from top of the slope, there is no significant change in safety factors up to a certain depth (0.20 m from the top of slope), and distinct changes in safety factor occur from 0.2 meter by deepening the ground

water level. The relationship between the safety factor and the groundwater level has an asymptotic with strong correlation coefficient.

REFERENCES

[1] Bishop, A.W.,"The use of slip circle in the stability analysis of slopes", Geotechnique, 5, pp. 7-17, http://dx.doi.org/10.1680/geot.1955.5.1.7, 1955.

[2] Spencer, E., " Effect of tension on stability on embankments", Journal of Geotechnical and Geoenvironmental Engineering ASCE, 94, SM5, pp.1159-1173, 1968.

[3] Spencer, E., "Thrust line criterion in embankment stability analysis", Geotechnique, 23, pp. 85-100, http://dx.doi.org/10.1680/geot.1973.23.1.85.-, 1973.

[4] Maksimovic, M., "Limit equilibrium for nonlinear failure envelope and arbitrary slip surface", Proc. 3rd Int. Conf. on Numerical Methods in Geomechanics, Aachen, pp. 769-777, 1979.

[5] Ching, R.K.H., Fredlund, D.G., "Some difficulties associated with the limit equilibrium method of slices", Canadian Geotechnical Journal, pp. 661-672, http://dx.doi.org/10.1139/t83-074, 1983.

[6] Fredlund, D.G., "State of the Art Lecture-Analytical methods for slope stability analysis", IV Int. Symposium on Landslides, Toronto, 1984.

[7] Brinkgreve, R.B.J., Bakker, H.L., "Non-linear finite element analysis of safety factors", Proc. of the 7th Int. Conf. on Comp. Methods and Advances in Geomechanics (IACMAG), Cairns, pp. 1117-1122, 1991.

[8] Duncan, J.M., "State of the art: limit equilibrium and finite-element analysis of slopes", Journal of Geotechnical and Geoenvironmental Engineering ASCE,22, 7, 577-596, 1996.

[9] Griffiths, D.V., Lane, P.A., " Slope stability analysis by finite elements", Geotechnique, 49, 3, pp. 378-403, 1999.

[10] Cheng, Y.M., " Location of critical failure surface and some further studies on slope stability analysis", Computers and Geotechnics 30 (2003), pp. 255-267, http://dx.doi.org/10.1016/S0266- 352X(03)00012-0, 2003.

[11] Hammah, R., Jacoub, T., Corkum, B., Curran, J., "A comparison of finite element slope stability analysis with conventional limitequilibrium investigations", Rocscience, 2005.

[12] Cheng, Y.M., Lansivaara, T., Wei, W.B., "Two-dimensional slope stability analysis by limit equilibrium and strength reduction methods", Computers and Geotechnics, 34, pp. 137-150, 2007.

[13] Köksal, T., " Sonlu Elemanlar Metodu", Yıldız Teknik Üniversitesi Yayını, No:304, İstanbul, 1995.

[14] Plaxis 2D, "Finite Element Code For Soil Rock Analyses", User Manual, Delf, 2006.

Clear-Water Experimental Scour Depths at Abutments

Evangelia Farsirotou[1], Nikolaos Xafoulis[2], Theofanis Athanasiou[3], Georgia Katsaridou[4]

Department of Civil Engineering T.E., Faculty of Applied Sciences, Technological Educational Institute of Thessaly, 411 10 Larissa, Greece.

Abstract**—***Laboratory experiments on local scour process at wing wall bridge abutments were conducted for different hydraulic conditions and compared with measurements on local scour depths around vertical wall abutments, under the same flow and sediment transport conditions. The study reports an extensive experimental investigation performed in a laboratory flume in the Technological Educational Institute of Thessaly, whose findings are used to describe the effects of different hydraulic parameters on local scour depth variation in the vicinity of the constructions. Three different sizes of wing wall abutment's lengths, transverse to the flow direction, were used in order to investigate the impact of this parameter to local scour variation. The expected bed erosion and the maximum scour depth at the upstream edge of the wing wall abutments are satisfactorily simulated by the experimental procedure. All the experimental results are graphically presented and comparisons between clear-water scour depths around the vertical wall and the wing wall abutments show lower values of scour depths in the vicinity of the wing wall abutments, under the same hydraulic and sediment transport conditions and for the same abutment widths. The experimental data of clear-water scour conditions were used to determine an equation of maximum equilibrium scour depth through regression analysis. The estimated scour depths were in agreement with the experimental values for each abutment geometry.*

Keywords**—***Abutments, Laboratory experiments, Open channels, Scour depth.***

I. INTRODUCTION

Realistic estimation of scour depth around bridge abutments in alluvial rivers is important for safe and economic design of their foundations. The scour hole just downstream of the head of the abutment can endanger the stability of the structure and led to the failure of the construction. The basic mechanism causing local scour at piers or abutments is the formation of vortices at their base which removes bed material from around the base of the construction. From the engineering view point, an accurate quantitative estimation of local scour process around hydraulic structures is necessary for the prevention of severe environmental problems un natural rivers.Extensive research has been conducted to determine the depth and location of the scour hole that develops around abutmentsand numerous abutment scour equations have been developed to predict this maximum scour depth [5].

Numerous experimental investigations have been performed on the study of the flow, the bed level variation and mainly the scour mechanisms in rivers and especially around bridge piers and abutments. Laboratory investigations of local scour at bridge piers and abutments were presented [7] and [6]. Development of local scour depths at vertical wall bridge abutments of varying lengths was investigated in several series of experiments of ranges of uniform sediments and clear-water flow intensities[1].Local scour experiments were performed around a trapezoidal abutment [9] and experimental measurements to simulate bed variation near a trapezoidal bridge abutment and investigation of the impact of water depth and flow discharge on scour depths were also performed [3].

The objective of this research work is to investigate local scour process around wing wall abutments and compare the experimental results of equilibrium scour depths around vertical wall and wing wall abutments, under the same hydraulic and sediment transport conditions. For this purpose, a laboratory experimental procedure was established to simulate local scour around wing wall abutmentsin uniform sediments under clear-water scour conditions. The impact of flow discharge and width of the abutment, for each abutment geometry, is also investigated and the findings are used to describe the effects of various parameters on scour depth and to determine an equation of maximum equilibrium scour depth.

II. EXPERIMENTAL LABORATORY PROCEDURE

The experiments were conducted in a 6.0m long, 0.078m wide and 0.25m deep research flume at Hydraulics Laboratory of Civil Engineering T.E. Larissa Department, Technological Educational Institute of Thessaly.As the object of the current work is the comparison of scouring procedure around vertical wall and wing wall abutments, three differentsizes of abutment models, for each geometry, were used and a parametric investigation of local scour depth evolution around the obstructions

was conducted.Each abutment model was placed on the plexi-glass wall of the flume, parallel to the flow direction. The abutment projected into the main flow and was located at a distance of 2.0 m from the inlet test section. The streamwise length of each vertical wall abutment was equal to 0.10m while for the wing wall abutment it depends on the abutment width according to the angle of the abutment walls, which was equal to 80^{o}.The lengths of the abutmentstransverse to the flow, abutment width, b, were constructed equal to 0.036m, 0.045m and 0.051m.All the experiments on local scour were conducted at short abutments as the ratio of abutment width to approaching flow depth was less than unity. The bottom slopes of the tested flume, in longitudinal and transverse directions, were set equal to zero.Fig. 1 shows a schematic illustration of the total experimental set-up. The bottom of the tested experimental area was carefully covered with material, consisted of sand, producing a uniform layer of sediment of 0.15 m thickness. The used bed material had a mean diameter D_{50} of 2.0 mm, a specific weight $S_g$of 1.60 and was assumed to be uniform as the geometric standard deviation, computed by $(D_{84}/D_{16})^{0.5}$ was equal to 1.26. The experimental inflow discharges, Q, were equal to 0.0004 m^3/s, 0.0005 m^3/s, 0.0006 m^3/s, 0.0007 m^3/s, 0.0008 m^3/s and 0.00095 m^3/s.The same laboratory hydraulic conditions, bed sediment load characteristics and the experimental procedure for the simulation of local scour process around vertical wall abutments were also used for the current experimental investigation of scouring procedure around wing wall abutments.Clear-water scour conditions were maintained for all the experiments [4].In order to maintain the condition of short abutments, with respect to the flow depth upstream of the abutment, h, the ratio b/h was restricted to $b/h \leq 1$ for all experiments.

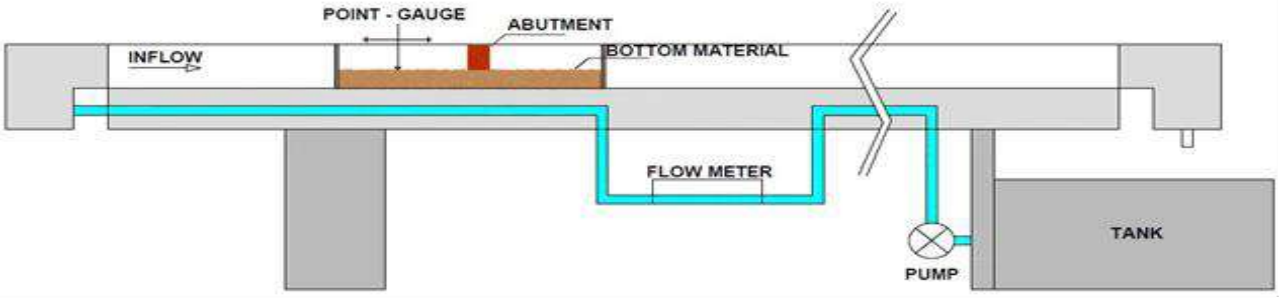

FIG. 1. SCHEMATIC VIEW OF THE LABORATORY EQUIPMENT

After the required time duration period is reached, the bed elevation measurements data, under equilibrium conditions, were recorded using a water-level gauge moving in longitudinal and in transverse directions of the flume introducing an optical error of ~0.1mm. Measurement data were obtained along the ¨flow lines¨ presented in Fig. 2. ¨Flow line¨ 1is located at a constant distance of 0.005m to the streamwise face of the abutment parallel to the flow direction.All measurements along the hypothetical ¨flow line¨ 1 were obtained at successive distances of 0.02m for the verticalwall abutments and are presented along the red ¨flow line¨ 1 while the measurements,for the wing wall abutment, along the hypothetical ¨flow line¨ 1 were obtained at successive distances of 0.02 and 0.01m and are presented along the blue ¨flow line¨ 1 in Fig. 2.

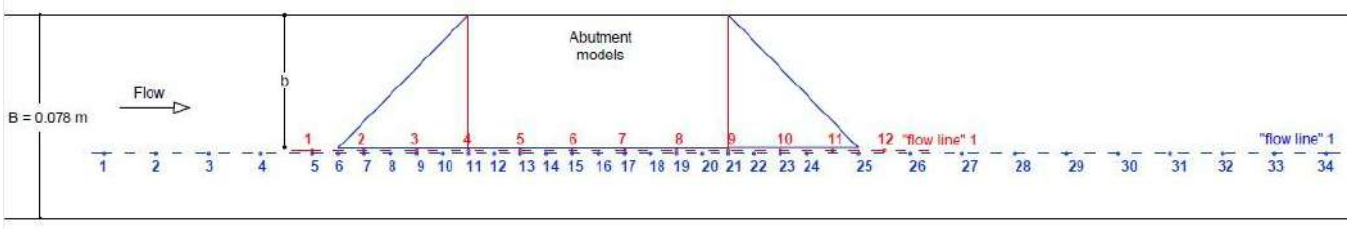

FIG. 2. MEASUREMENT DATA LOCATIONS FOR THE TWO ABUTMENT GEOMETRIES

III. ANALYSIS OF SCOURING PROCESS

Fig. 3 presents the experimental equilibrium local scour depths along the aforementioned ¨flow line¨ 1 for the vertical wall and for the wing wall abutment, with abutment width equal to b=0.035m, under different hydraulic conditions for six different inflow discharges. Maximum local scour depth measurements along the ¨flow line¨ 1 for the same hydraulic conditions and for abutment's lengths, transverse to the flow, equal to 0.045m and 0.051m, are given in Figs 4 and 5, respectively.Experiments show that along the upstream to the abutment region and close to the upstream side of the abutment erosion increases and a scour hole develops. The maximum scour depth occurs upstream of each abutment, at the upstream corner of the construction. At the downstream side of the abutment, the previously eroded material is deposited there and the scour depth is relatively small. Analyzing the experimental measurements, it is obviously that for each abutment width the

maximum depth of scour and the scour hole area are always greater in the region of the vertical wall abutments than around the wing wall abutments, for the same hydraulic conditions. Moreover, the plots demonstrate that for the same hydraulic and sediment transport conditions maximum local scour depth increases with increase in the abutment width, normal to the flow direction, for each experimental simulation.

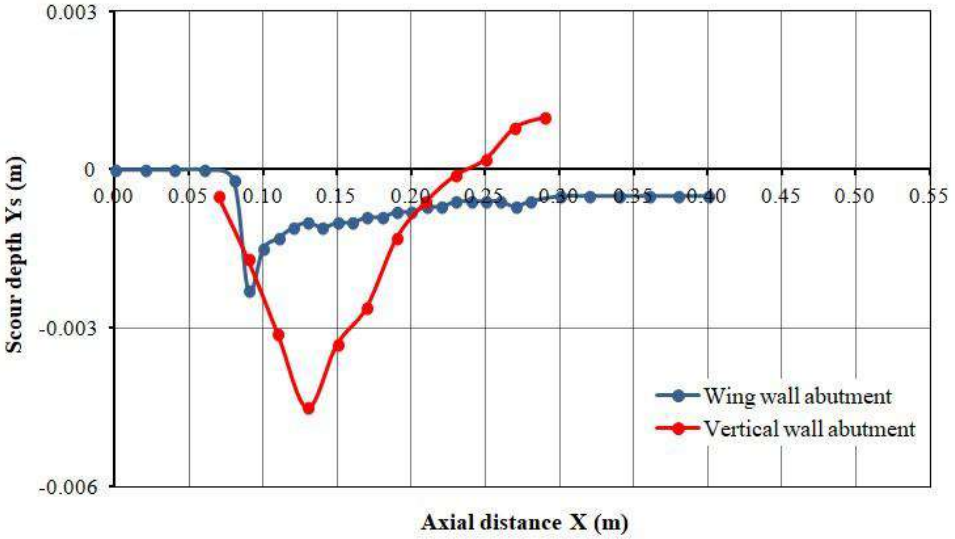

(a) Q=0.0004 m^3/s

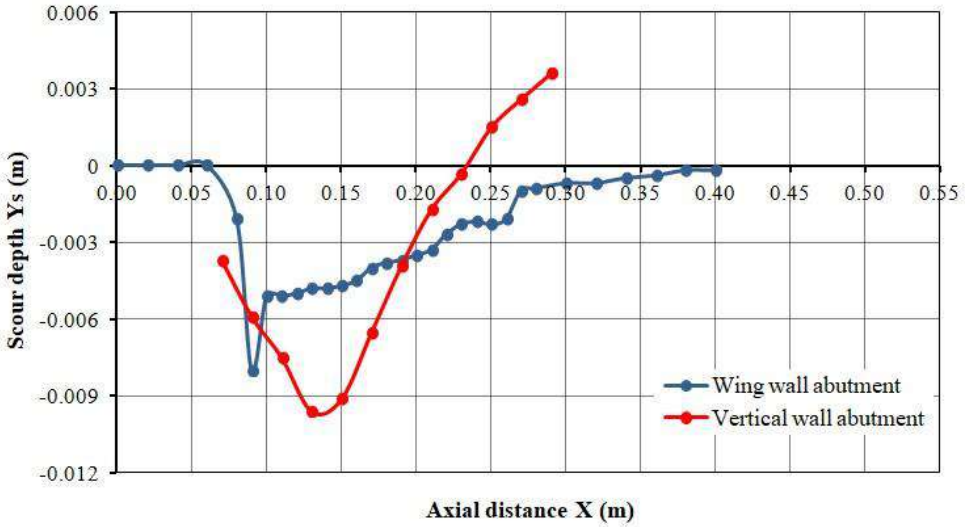

(b)Q=0.0005 m^3/s

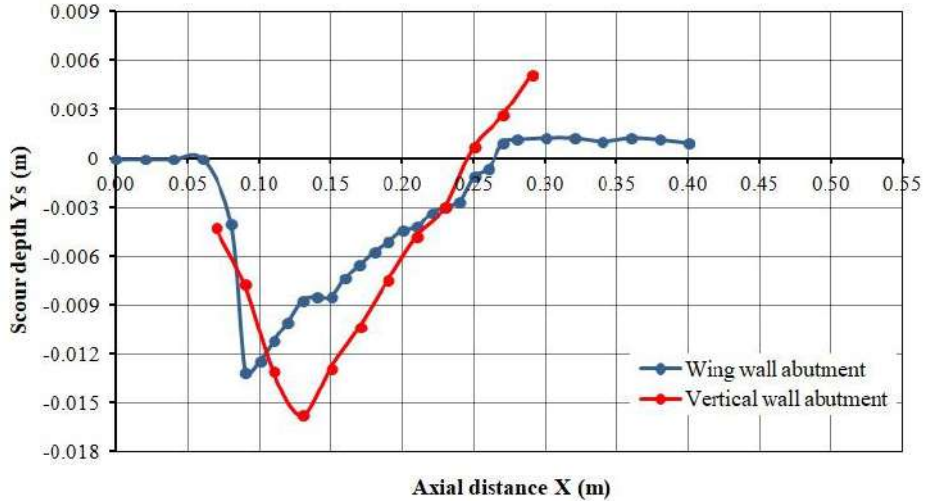

(c)Q=0.0006 m^3/s

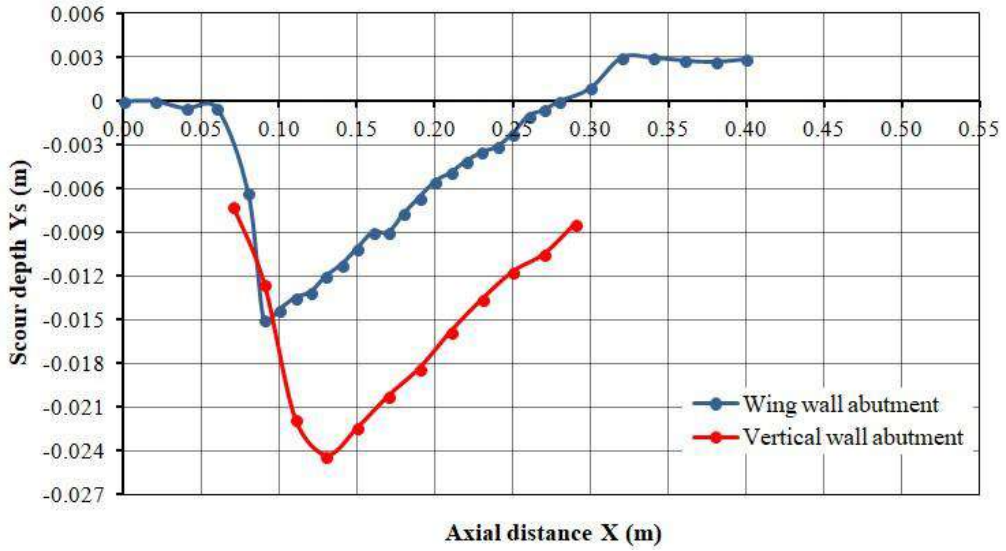

(d)Q=0.0007 m^3/s

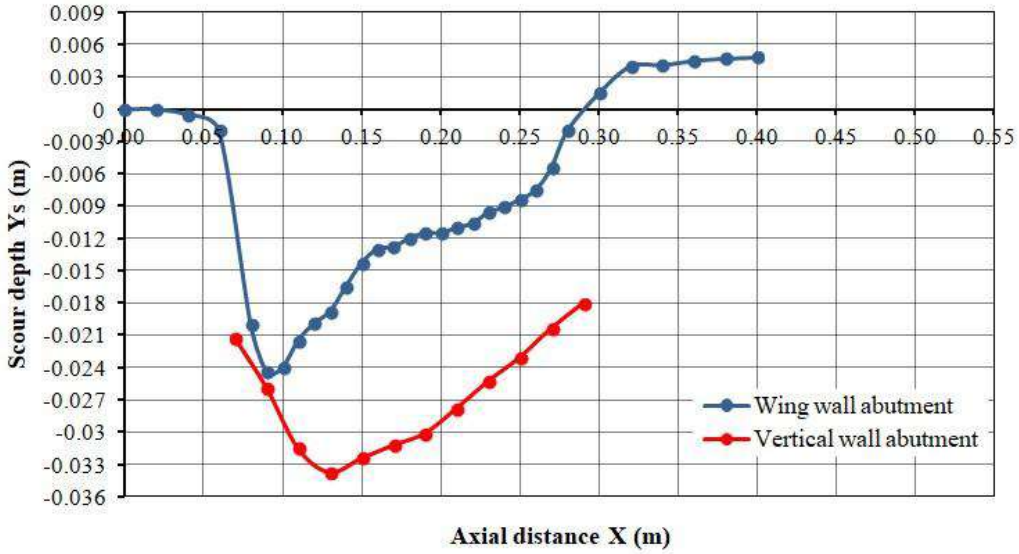

(e)Q=0.0008 m^3/s

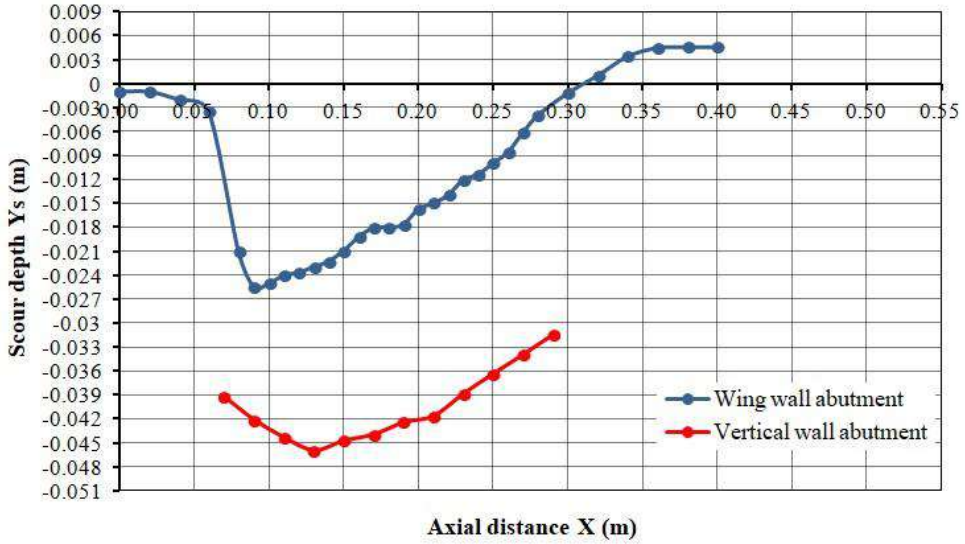

(f)Q=0.00095 m^3/s

FIG. 3 COMPARISON BETWEEN MEASURED LOCAL SCOUR VARIATION ALONG THE STREAMWISE FACE OF THE ABUTMENTS, FOR B=0.036M AND DIFFERENT INFLOW DISCHARGES

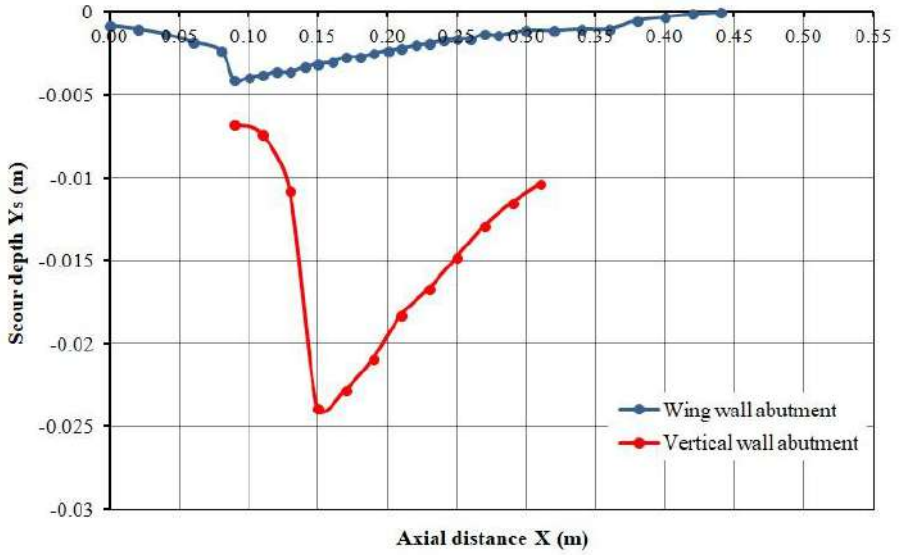

(a)Q=0.0004 m^3/s

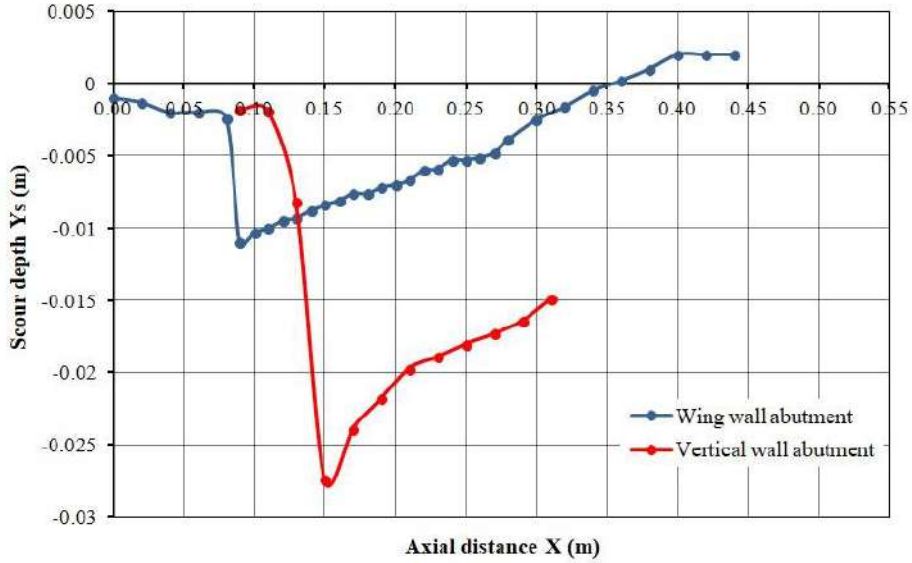

(b)Q=0.0005 m^3/s

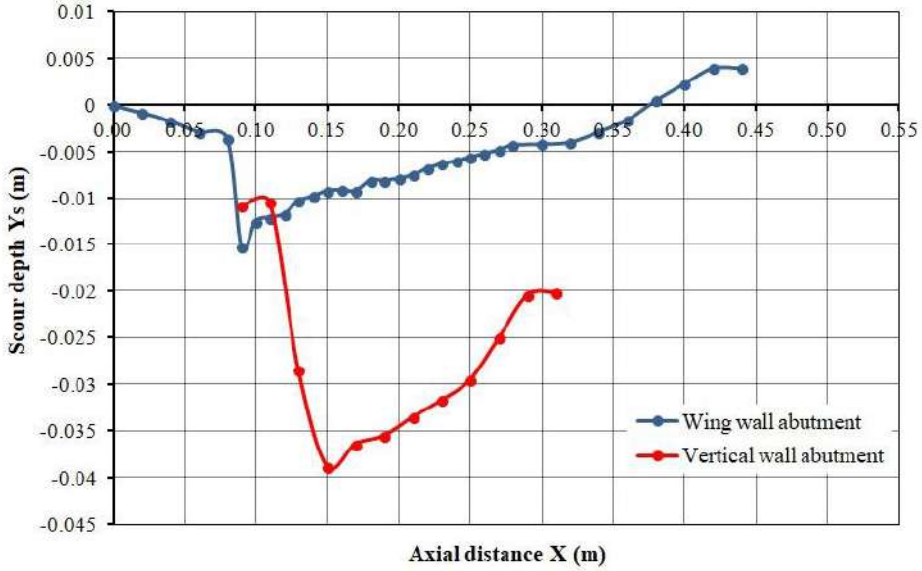

(c)Q=0.0006 m^3/s

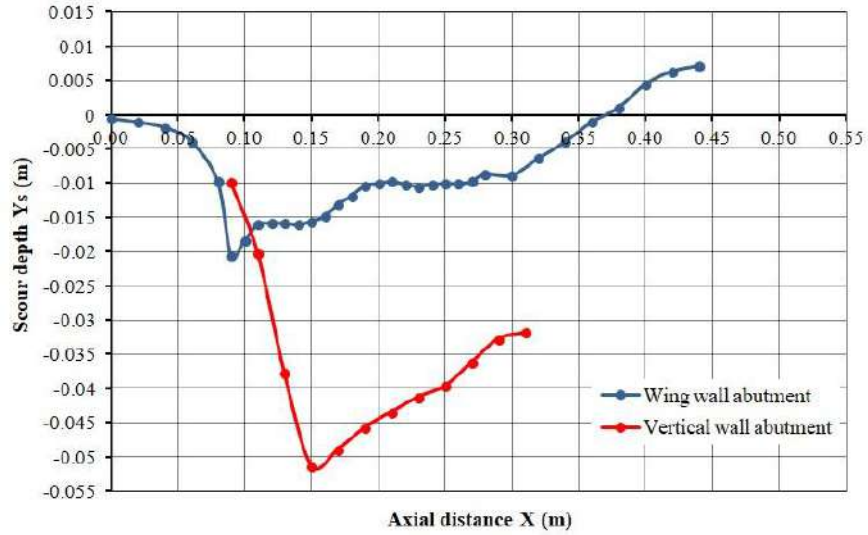

(d)Q=0.0007 m^3/s

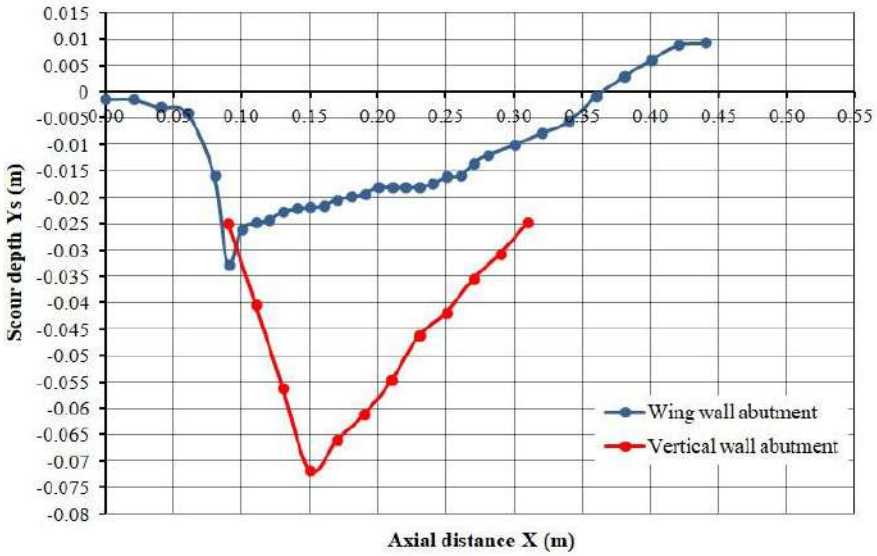

(e)Q=0.0008 m^3/s

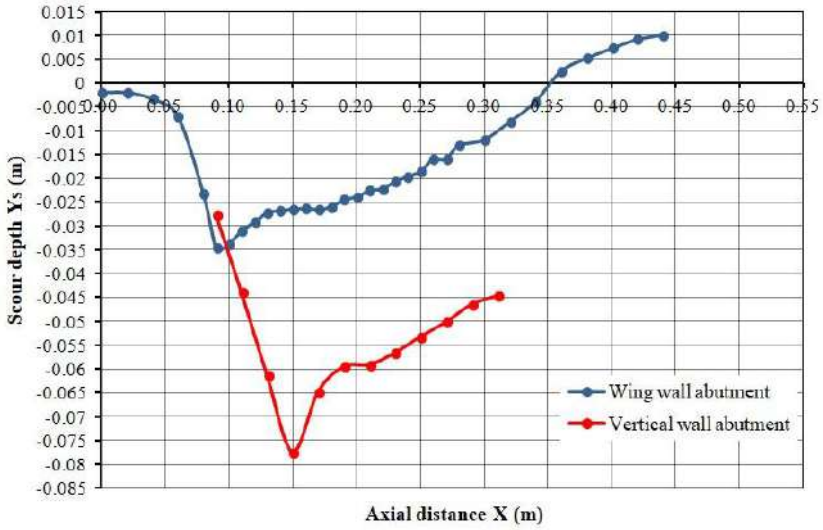

(f)Q=0.00095 m^3/s

FIG. 4 COMPARISON BETWEEN MEASURED LOCAL SCOUR VARIATION ALONG THE STREAMWISE FACE OF THE ABUTMENTS, FOR B=0.045M AND DIFFERENT INFLOW DISCHARGES

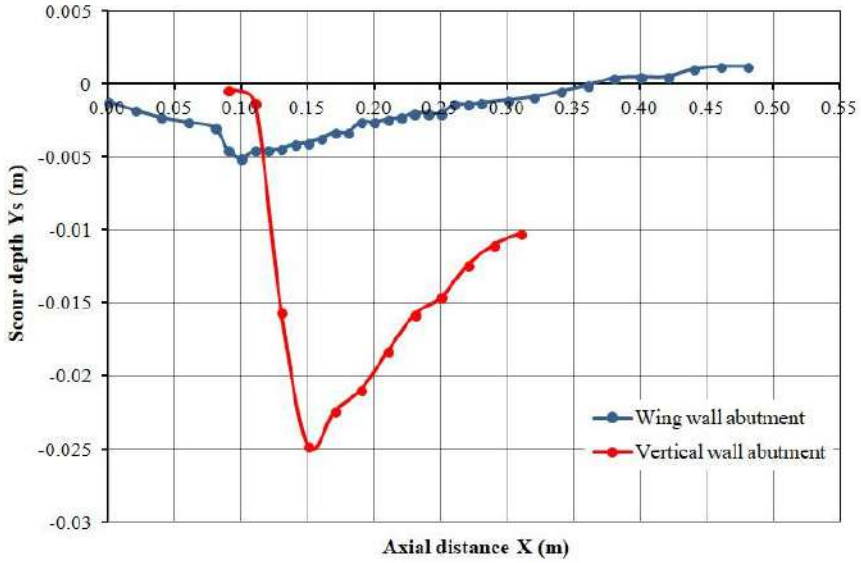

(a)Q=0.0004 m^3/s

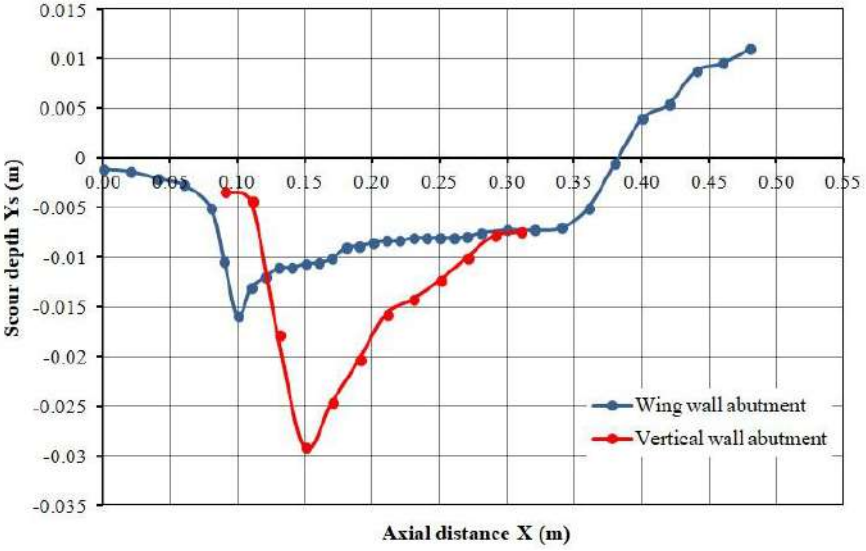

(b)Q=0.0005 m^3/s

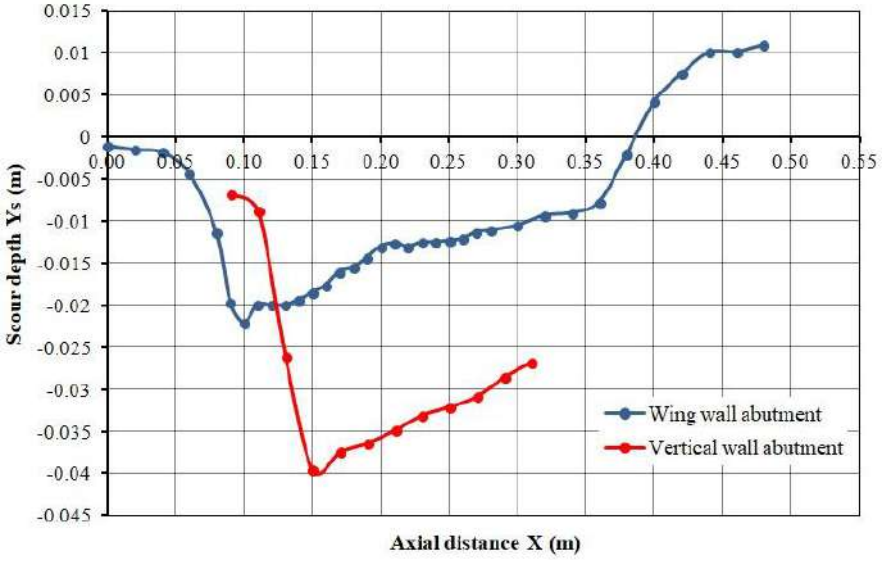

(c)Q=0.0006 m^3/s

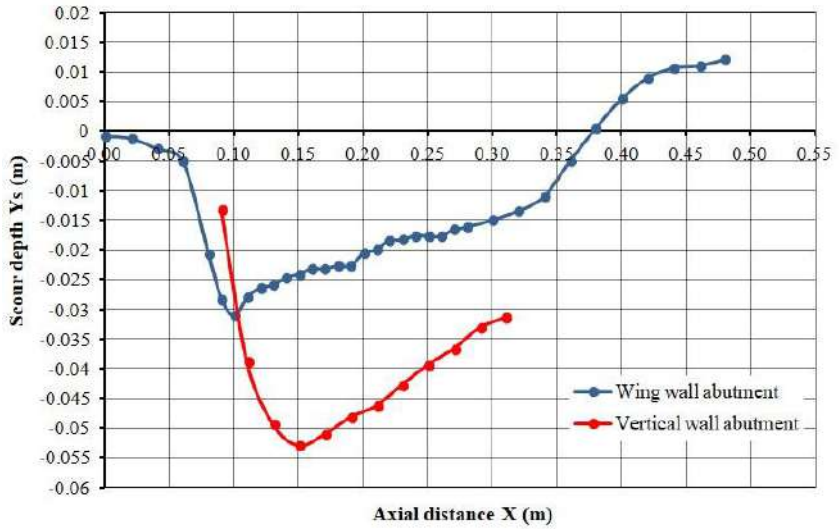

(d)Q=0.0007 m^3/s

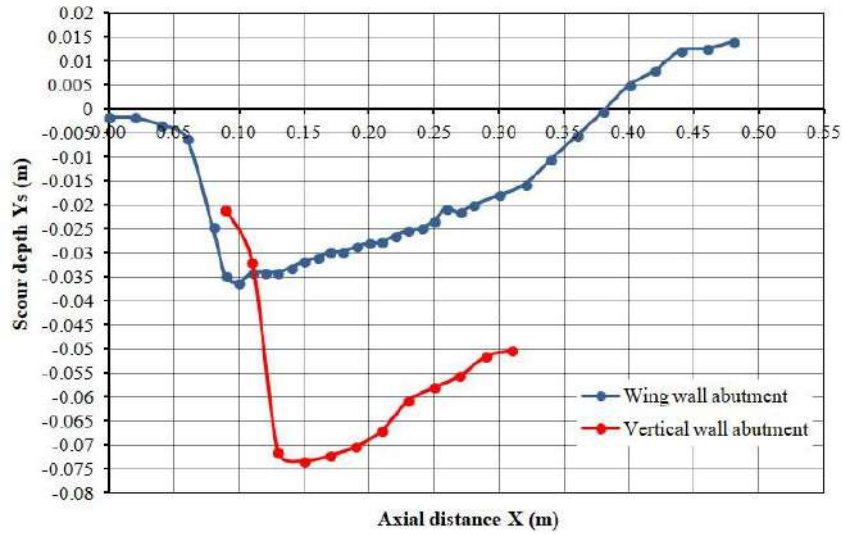

(e)Q=0.0008 m^3/s

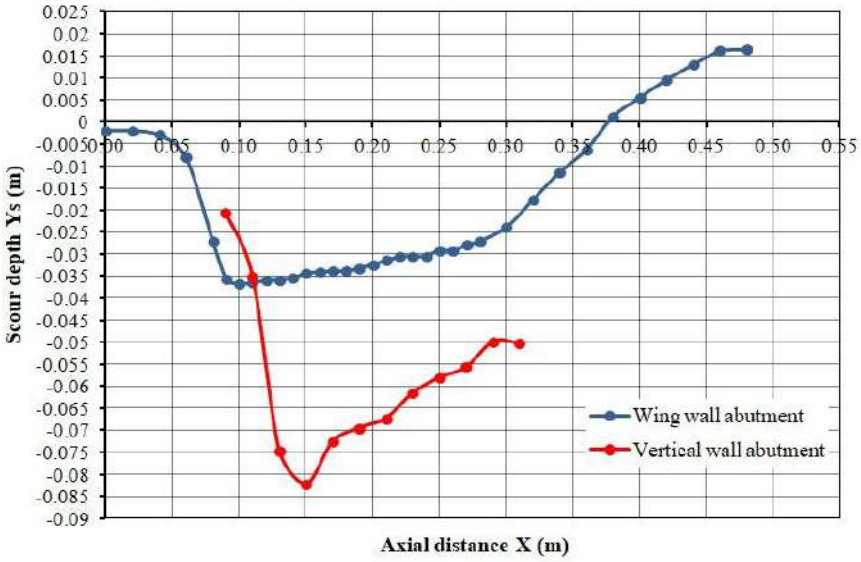

(f) Q=0.00095 m^3/s

FIG. 5. COMPARISON BETWEEN MEASURED LOCAL SCOUR VARIATION ALONG THE STREAMWISE FACE OF THE ABUTMENTS, FOR B=0.051M AND DIFFERENT INFLOW DISCHARGES

IV. MAXIMUM EQUILIBRIUM SCOUR DEPTH

Dey at al [2]performed a regression analysis of their experimental data and proposed the following equation of non-dimensional maximum scour depth for different short abutments:

$$\frac{Y_{s\max}}{b} = 6.18K_s F^{0.26}\left(\frac{h}{b}\right)^{0.18}\left(\frac{D_{50}}{b}\right)^{-0.15} \quad (1)$$

where K_s is abutment shape factor, being equal to 1 for vertical wall abutments [8] and equal to 0.82 for wing wall abutments [10], F is the Froude number according to the hydraulic conditions upstream of the abutment and h is the relative flow depth.The comparison of maximum scour depths obtained from the equation (1) with the current experimental data of vertical wall and wing wall abutments indicates that the above equation fits well with the experimental data. The value of correlation coefficient between the experimentally obtained and the computed maximum scour depths for the vertical wall abutment models is equal to 0.955 and for the wing wall abutment models is equal to 0.965 and indicates the accuracy of the experimental procedure. An extensive presentation of the hydraulic conditions used in the current parametric study is given[4]. Equation (1) indicates that the maximum scour depth increases with increase in Froude number and in flow depth.

V. CONCLUSION

The current research work presented bed level experimental measurements to produce data base intended as support in the development of new and the refinement of existing codes for computing free-surface flows with movable beds specifically around bridge abutments and generally on bed level evolution due to sediment transport. All measurements were carried out in a laboratory open channel flume and the test case geometry is formed from wing wall abutments. Experimental measurements on scour depths around the wing wall abutments were obtained at various locations near the abutments, for different inflow discharges and abutment widths, in uniform sediments, under clear-water scour conditions and were compared with available measurements on vertical wall abutments. Analyzing the experimental data it is obviously that for each abutment width the maximum scour depth and the scour hole area are always greater in the region of the vertical wall abutments than around the wing wall abutments, for the same hydraulic and sediment transport conditions. The experimental results in clear-water scour conditions have been used to determine an empirical equation of maximum equilibrium scour depth and the estimated values are in good agreement with the experimental measurements.

REFERENCES

[1] S. Coleman, Ch. Lauchlan and B. Melville, ¨Clear-water scour development at bridge abutments¨, Journal of Hydraulic Research, vol. 41, 2003, pp. 521-531.

[2] S. Dey and A. Barbhuiya, "Clear-water scour at abutments in thinly armored beds", Journal of Hydraulic Engineering, ASCE, vol. 130, 2004, pp. 622-634.

[3] E. Farsirotou, V. Dermissis and J. Soulis, "Test case for bed morphology computations", Journal of Computational Methods in Sciences and Engineering, vol 7, 2007, pp. 105-131.

[4] E. Farsirotou and N. Xafoulis, "An experimental study of local scour depth around bridge abutments*",* International Journal of New Technology and Research, vol. 3(9), 2017, pp. 01-10.

[5] Federal Highway Administration U.S. Department of Transportation, "Evaluating Scour at Bridges", Publication No. FHWA-HIF-12-003, 2012.

[6] J. Kandasamy and B. Melville, ¨Maximum local scour depth at bridge piers and abutments¨, Journal of Hydraulic Research, vol. 36, 1998, pp. 183-198.

[7] R. Kw An and B. Melville, ¨Local scour and flow measurements at bridge abutments¨, Journal of Hydraulic Research, vol. 32, 1994, pp. 661-673.

[8] B. Melville, "Local scour at bridge abutments", Journal of Hydraulic Engineering, vol. 118(4), 1992, pp. 615-631.

[9] A. Radice, F. Ballio and G. Porta, ¨Local scour at a trapezoidal abutment: sediment motion pattern¨, Journal of Hydraulic Research, vol. 49, 2009, pp. 250-262.

[10] E. Richardson and S. Devis, "Evaluation scour at bridges", HEC18 NHI-001, FHWA, Federal Highway Administration, U.S. Department of Transportation, Washington, D.C. 2001.

Application of the Factorial Design Technique for the Optimization of the Chemical Isolation Process of Lead in Environmental Analyzes

Gonçalves, MCP[1], Rodrigues, FW[2], Romanelli, JP[3]

[1]Science and Technology Institute, Federal University of Alfenas, José Aurélio Vilela Road 11999, Km 533, CEP 37715-400, Poços de Caldas, MG, Brazil.
[2,3]Federal University of São Carlos, 13565-905, São Carlos-SP, Brazil.

Abstract*—Nuclear energy plays a key role in long-term development plans and can guarantee the supply of electricity to some regions. On the other hand, the implementation of these projects tends to require long maturation periods, require high investment costs and may be a source of pollutants, such as Lead (Pb). For this reason, the periodic environmental monitoring of the concentration of pollutants becomes necessary, according to the current legislation. Thus, the present work presents as a proposal a method of optimization of Pb quantification in environmental analyzes. The study was developed through the monitoring of wastewater samples from INB – Indústrias Nucleares do Brasil. From the Fractional Factorial Design(FFD) the most representative variables of the Pb isolation process were determined, and through the Central Composite Design (CCD) the response surface was found, generating a regression model that represents the system. The results indicated that the optimization of the chemical yield of Pb is associated to the higher dosages of Nitrilotriacetic Acid (NTA) and Sulfuric Acid (H_2SO_4) in the samples. The optimum yield condition was obtained in the region of 200 ml of H_2SO_4 and 4.0 g of NTA, considering the range tested. The proposal proved to be effective for the validation tests of the model, obtaining an increase of up to 32% in the Pb yields of the analyzes.*

Keywords*—*Chemical Yield, Environmental Analyzes, Lead, Nuclear Power, Response Surface.

I. INTRODUCTION

The generation of electricity from nuclear sources can be considered advantageous and represent a viable strategy of diversification of the energy matrix in some countries [1,2], meeting the goals of reducing greenhouse gas emissions compatible with the Kyoto Protocol [3,4]. Nuclear energy plays a key role in long-term development plans and can guarantee energy supply for some regions [5]. On the other hand, the implementation of these projects tends to require long maturation periods, from the installation of the plant until its operation, in addition to requiring high investment costs and representing sources of environmental degradation [4,6,7].

Currently in Brazil nuclear sources have little expressiveness in the electric matrix, but this scenario tends to undergo changes until the year 2050 [8]. The Brazilian government plans to build new nuclear plants by 2030 [6,9], which should represent an increase of approximately 6 GW in capacity country [6,10].

The process of generating energy from nuclear sources occurs through nuclear fission in reactors, which are fed by fuels from the extraction of uranium ore [11,12,13,14,15]. From the mining stage to the production of nuclear fuel, innumerable pollutants from soil, air and water, especially heavy metals, such as lead, which has high toxicity and may cause serious social and environmental impacts [16,17,18,19,20,21,22].

In the case of wastewater from nuclear activities, there is a demand for specific treatments so that they can meet the quality adjustments [23,24], as established by Resolution No. 430 of the Conselho Nacional de Meio Ambiente – CONAMA [25]. According to this resolution, release of effluents containing Pb to water bodies or collection systems must comply with the maximum acceptable limit of 0,5 $mg.L^{-1}$ [25]. Therefore, periodic environmental analyzes must be carried out to monitor and control the concentration of Pb according to current legislation [26,27,28,29]. Such analyzes involve a methodology of isolation and quantification, having as principle the separation of the lead from the other elements, besides the separation between them by selective precipitation aiming the determination of the yield of Pb in the samples.

Thus, the present study proposes the optimization of the lead insulation process in environmental analyzes, as a way to improve the efficiency of the quantification of Pb yields, in order to guarantee reliable results that comply with the norms of the current legislation. The Fractional Factorial Design (FFD) was used to determine the most representative variables of the process [30,31,32,33,34], in order to verify the relevant sources of interference of the method employed. The Central

Composite Design (CCD) was used to find the response surface where the yield of Pb is maximum, generating a regression model that represents the system [35,36,37,38,39,40].

II. MATERIAL AND METHODS

The execution of the factorial design was started with the collection of a sample composed of water (60 liters), collected from several monitoring points of the company Indústrias Nucleares do Brasil (INB), a unit of Caldas-MG. The sample was filtered and reduced in hotplate up to 30 liters. In the first step of the optimization, four variables were selected to be tested in the chemical insulation of lead (Pb): i) addition order of Nitrilotriacetic Acid (NTA), Sodium Hydroxide (NaOH) 6 $mol.L^{-1}$, Ammonium Sulfate (NH_4SO_4) 25 $mg.L^{-1}$ and heated distilled water; ii) NTA dosage; iii) dosage of Sulfuric Acid (H_2SO_4) 3 $mol.L^{-1}$, and iv) dosage of Sodium Sulphide (Na_2S) 1 $mol.L^{-1}$.

According to the Fractional Factorial Design procedures, the number of experiments to be performed is of the order of 2^{n-1}, where n represents the number of variables listed [30]. Thus, in this study, 8 experiments (2^{4-1}) were performed in triplicate, totaling 24 tests. The FFD codifies the possibilities to be tested in the level tests. In this case, the level -1 represents the currently applied conditions and the level +1 the new conditions tested. Table 1 shows the cataloged variables and their respective levels.

TABLE 1
VARIABLES LISTED AND THEIR RESPECTIVE LEVELS.

Variable	Level
A) Order of addition of the reagents: nitrilotriacetic acid (NTA), sodium hydroxide (NaOH) 6 $mol.L^{-1}$, ammonium sulfate (NH_4SO_4) 25 $mg.L^{-1}$ and heated distilled water	**Level (-1):** 1º NTA, 2º NaOH, 3º NH_4SO_4, 4º heated distilled water (current order). **Level (+1):** 1º heated distilled water, 2º NaOH, 3º NTA, 4º NH_4SO_4 (new order).
B) Dosing of NTA	**Level (-1):** 2,0 g of NTA (current dosage). **Level (+1):** 4,0 g of NTA (new dosage).
C) Dosing of H_2SO_4 3 $mol.L^{-1}$	**Level (-1):** 50 ml of H_2SO_4 0,1 $mol.L^{-1}$ (current volume). **Level (+1):** 150 ml of H_2SO_4 0,1 $mol.L^{-1}$ (new volume).
D) Dosing of Na_2S 1 $mol.L^{-1}$	**Level (-1):** 1,0 ml of Na_2S (current volume). **Level (+1):** 3,0 ml of Na_2S (new volume).

The next step consisted in inserting all variables and their respective levels into Minitab software (version 16.2.4.4), in order to obtain an array with all possible combinations of experimental tests (Table 2) [41].

TABLE 2
EXPERIMENTAL MATRIX OF THE FRACTIONAL FACTORIAL DESIGN FOR Pb.

Experiment	Level	NTA (g)	H_2SO_4 (ml)	Na_2S(ml)
1	+1	2	50	3
2	-1	2	50	1
3	-1	4	150	1
4	+1	4	150	3
5	+1	4	50	1
6	-1	2	150	3
7	+1	2	150	1
8	-1	4	50	3

From the matrix obtained, the tests of isolation and quantification of Pb with the 24 samples were performed, following the analysis procedures described below:

1. After the filtration initially described, the sample was transferred to 24 beakers of 2 liters, each containing 1 liter of sample;
2. Then 1 mL of 20 $mg.mL^{-1}$ Barium solution and 1 mL of 20 $mg.mL^{-1}$ Lead solution were added with a micropipettor;
3. With dispensing, 5 mL of Citric Acid solution ($C_6H_8O_7$) 1 $mol.L^{-1}$ and 2 drops of 0.1% Methyl Red in each beaker were added. The pH of the sample was adjusted between 6.0 and 7.0 with Ammonium Hydroxide (NH_4OH) and Nitric Acid (HNO_3) 5 $mol.L^{-1}$ slowly, until turning from red to yellow, using calibrated Phmetro;
4. To each beaker were added 50 ml of Sulfuric Acid solution (H_2SO_4) 3 $mol.L^{-1}$, with stirring, and the solution was heated to boiling and allowed to settle until the following day;
5. The supernatant was then drained by siphoning and the precipitate transferred quantitatively into the glass centrifuge tube using osmosis purified water;
6. The sample was centrifuged for 10 minutes at 2000 RPM and the supernatant discarded by siphoning. This was done with 20 ml of H_2SO_4 solution 0.1 $mol.L^{-1}$ added to the precipitate, while the supernatant was centrifuged and discarded by siphoning again;
7. To the precipitated was added 2.0 g of Nitrilotriacetic Acid (NTA), 10 mL of Sodium Hydroxide solution (NaOH) 6 $mol.L^{-1}$, 50 mL of distilled water and 5 mL of Ammonium Sulfate $(NH_4)_2SO_4$) 25 $mg.mL^{-1}$;
8. The tubing solution was heated in a water bath at approximately 90 °C for 15 minutes until the precipitate dissolved completely. Then, the pH of the sample was adjusted by adding glacial Acetic Acid to pH between 4.0 and 4.5 and the solution was held until the following day;
9. The solution obtained was centrifuged, the supernatant was transferred to a 250 mL beaker to separate it from the precipitate and it was reserved in tubes;
10. In each of the supernatants obtained was added 1 mL of Sodium Sulfate (Na_2S) solution 1 $mol.L^{-1}$. These were then left in a water bath at 90 °C for approximately 15 minutes;
11. After cooling the samples in the chambers, the solutions obtained were centrifuged, the supernatant was discarded by siphoning and the precipitate was washed with 50 ml of distilled water. The sample was then centrifuged again and the supernatant discarded by siphoning. To the precipitate was added 10 mL of HNO_3 solution 5 $mol.L^{-1}$;
12. The solution was taken in a water bath at approximately 90 °C and waited from 100 to 120 minutes until the total Lead Sulphide formation reaction occurred, which is indicated by the absence of dark, sulfur-forming spots. Each of the samples was screened on white strip paper and the filter was washed 3 times with heated distilled water. They were then left in a water bath for 10 minutes;
13. The pH of the resulting solution was adjusted between 4.0 and 4.5 with Ammonium Acetate solution (NH_4CH_3COO) 40%. To each sample was added 1 mL of Bismuth solution 5 $mg.mL^{-1}$ and 2 mL of Sodium Chromate solution (Na_2CrO_4) 30%;
14. The material was filtered using a vacuum filtration kit, with 0.45 μm membrane filter and diameter Ø = 47 mm, previously weighed in analytical balance. The precipitate was washed with distilled water, the filter was removed from the Kit and stoved at 60 °C for 90 minutes;
15. Finally, the filter was removed from the oven and placed in desiccator for 10 minutes. The samples were taken from the desiccator, weighed and the yield was calculated considering the added standard mass equal to 31 mg. The gravimetric yield was calculated from the Equation:

$$Y_{grav}\ (\%) = 100\frac{M_p - M_f}{M_a} \quad (1)$$

Where: M_p is the mass of the filter with precipitate;

M_f is the mass of the filter;

M_a is the theoretical mass of Lead standard (31 mg).

16. After the previous tests were carried out to determine the response surface of the CCD, the filters were digested in a microwave oven and then analyzed in an Inductively Coupled Plasma Atomic Emission Spectrometer (ICP). The chemical yield was calculated from the Equation:

$$Y_{chem}\ (\%) = \frac{C_{Pb}\ .V_f}{\frac{MM_{Pb}\ .\ m_{PbCrO\ 4}}{MM_{PbCrO\ 4}}}\ .100 \quad (2)$$

Where: C_{Pb} is the concentration of Pb ($g.L^{-1}$);

V_f is the volumetric flask volume (0.05 L);

MM_{Pb} is the molar mass of Pb (207.19 $g.mol^{-1}$);

m_{PbCrO_4} is the mass of Lead Chromate (0.031 g);

MM_{PbCrO_4} is the molar mass of Lead Chromate (323.2 $g.mol^{-1}$).

2.1 Validation of the model

To validate the model found by the response surface of the Central Composite Design (CCD), new tests were performed for four different samples of wastewater under the current conditions (50 mL of H_2SO_4 and 2 g of NTA) and under the optimum conditions established by the model. The assays followed the same procedure described previously for the chemical isolation of Pb by selective precipitation.

III. RESULTS AND DISCUSSION

After the Pb isolation for the 24 samples of FFD, the average gravimetric yields were obtained in each of the experimental conditions (Equation 1). In the next step, the variables were coded at levels -1 and +1, as described in Table 1, obtaining a new coefficient matrix. From the possible combinations between the four variables selected in the coded levels, the contrasts involved in the design and their respective percentages of contribution were calculated (Table 3).

TABLE 3
CONTRASTS CALCULATED FOR THE DEVELOPMENT OF THE FRACTIONAL FACTORIAL DESIGN FOR Pb.

Combinations	A+BCD	B+ACD	C+ABD	D+ABC	AB+CD	AC+BD	AD+BC
Contrasts	-5,88	-3,88	1,04	-2,29	1,79	0,04	-1,29
Contrasts (%)	56,82	24,72	1,78	8,64	5,28	0,003	2,746

To verify which of the selected variables have a significant effect on the system, the confidence interval of the contrast error was calculated. First, the number of degrees of freedom (DF) and the quadratic sum of the pure error (QSPE) were calculated. From the DF and QSPE values we found the experimental variance (S^2), the experimental error (S), the contrast error (S_c) and finally the confidence interval of the contrast error (I_{S_c}) for a 95% confidence interval, as shown in Equations (3), (4), (5) and (6), respectively. All statistical data obtained are presented in Table 4.

$$S^2 = \frac{\sum GL \cdot SQEP}{\sum GL} \quad (3)$$

$$S = \sqrt{S^2} \quad (4)$$

$$S_c = \frac{\sqrt{S^2}}{3} \quad (5)$$

$$I_{S_c} = t \cdot S_c \quad (6)$$

TABLE 4
STATISTICAL DATA FOUND FOR Pb ANALYSIS

Experimental Variance (S^2)	10,20
Experimental Error (S)	3,20
Contrast Error (S_c)	1,80
Confidence Interval of the Contrast Error (I_{S_c})	3,30

As the confidence interval for the Contrast Error found was 3.30, only the contrasts larger than this value in modulus will be significant. Thus, as shown in Table 4, only the interactions A+BCD (contrast: -5.88) and B+ACD (contrast: -3.88) are relevant.

As the probability of occurrence of a third-order interaction is minimal, it is considered that only A and B are influencing the analysis, only the dosage of H_2SO_4 (56.8%) and NTA (24.7%). According to researches by Ozer and Guçer (2011) [42], the volume of Sulfuric Acid presented as a relevant variable in the digestion process of Pb samples, since it can participate in the formation of Lead Sulphate precipitate. Studies by Sakurai et al. (2006) [43] also reported the significant effect of H_2SO_4 on the plastic digestion for the determination of Pb in a microwave oven. No results were found for NTA in the literature.

To visualize what was found by the previous calculations, a graph of cubes was constructed (Fig. 1), with the aid of the software OriginPro 9.1.0, which presents the variables under study and their respective levels coded as a function of the obtained Pb yield [44].

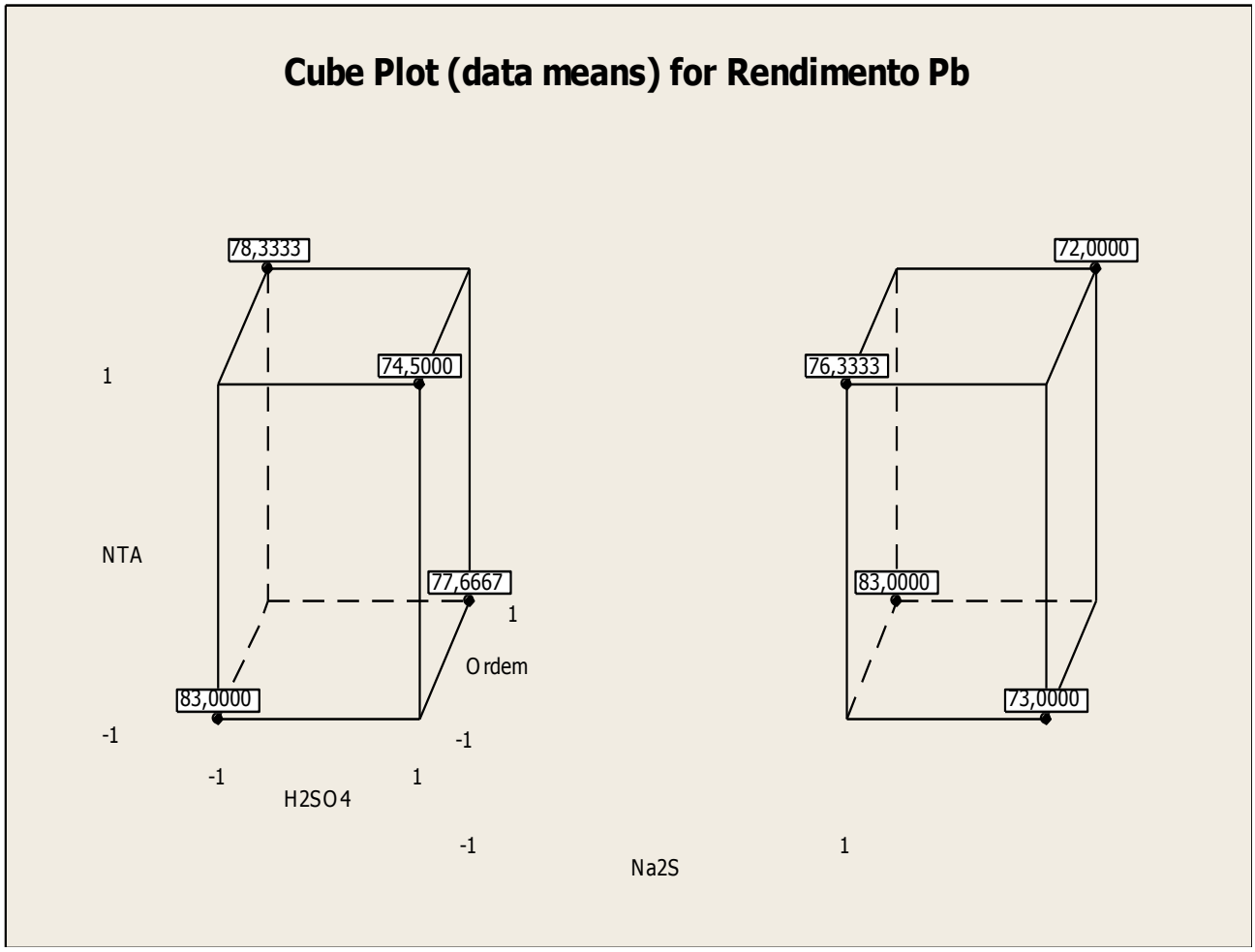

FIGURE 1. CUBE PLOT FOR Pb YIELD.

Fig. 1 shows that level -1 (current dosage) for H_2SO_4 has a higher average yield than level +1 (new dosage) for the same reagent, thus contributing to the maximization of Pb yield at level -1. For the NTA dosage, the level -1 also has an average yield greater than the level +1, evidencing that the level -1 is more advantageous for the increase of the Pb yield.

3.1 Response surface

The initial proposal to define the response surface of the FFD in question was to employ a Central Composite Design (CCD) with two variables (dosage of Sulfuric Acid and NTA). This type of experiment employs compounds with a central point in order to identify the best working conditions of an analytical method. The variables are tested in 5 different levels, ranging from $-\sqrt{2}$ to $\sqrt{2}$ [30].

By the established method, the coded interval (Ic) should be 2.83 for both H_2SO_4 and NTA dosage. The actual interval (Ir) was defined as 200 ml for H_2SO_4 and 3.5 g for NTA. From the values of Ic, Ir and the levels coded according to the Central Composite Design were calculated the actual levels. Table 5 shows the actual and coded levels defined by the CCD technique.

TABLE 5
CODED AND ACTUAL LEVELS ESTABLISHED BY THE CENTRAL COMPOSITE DESIGN METHOD.

Experiment	Coded Levels		Real Levels	
	Sulfuric Acid 3 mol.L^{-1}	NTA	Sulfuric Acid 3 mol.L^{-1} (ml)	NTA (g)
1	-1	-1	29,3	1,0
2	0	0	100,0	2,3
3	0	-1,4142	100,0	0,5
4	-1	1	29,3	3,5
5	-1,4142	0	0,0	2,3
6	1	-1	170,7	1,0
7	0	1,4142	100,0	4,0
8	1	1	170,7	3,5
9	1,4142	0	200,0	2,3

After the experiments were carried out by the method described for the lead insulation, the filters were obtained in a microwave oven and afterwards an Atomic Emission Spectrometer with Inductively Coupled Plasma (ICP). This procedure was performed in order to verify if the filters only have Lead Chromate (resulting from the analysis), or if any interfering substances are still present that were not totally removed in the isolation procedure and are contributing to the different gravimetric yield got from the chemical, obtained by quantification of Pb in the ICP, masking the true result of the analysis.

After the tests, the gravimetric yields were calculated by the Equation (1) and the chemical yields by Equation (2) of the methodology. The results indicated differences ranging from 5.6 to 33.6% among the yields obtained by gravimetry and quantification of Lead. The systematic difference observed, always with the gravimetric yield greater than the chemical, made it possible to list some possibilities on the origin of the difference, such as the addition of Bismuth solution 5 mg.L^{-1} in the Pb insulation and the residual moisture contained in the due to their drying temperature (60 °C), which may be contributing to a larger mass in the filter. Because the results obtained by quantifying Pb in ICP are more accurate than those found only by gravimetry, it was decided to use the results of chemical yield for the realization of the CCD.

With the execution of the method, it was verified that only the variables NTA and the interaction Sulfuric Acid*NTA are significant for the model. In this way, the other variables and interactions were extracted, being possible to obtain in the software Minitab 16.2.4.4 the following response surface model, which results in the conditions that provide the highest yields [41].

$$\text{Pb Yield } (\%) = 63{,}6828 + 3{,}7383.X_1 + 3{,}4385.(X_1X_2) \quad (7)$$

Where X_1 and X_2 are the coded levels of NTA and Sulfuric Acid, respectively.

Analyzing the model obtained, the greatest influence of the NTA variable (higher coefficient) is verified, although the interaction between the variables was also significant, evidencing that the response presents a distinct tendency, according to the established levels. Both variables show a positive coefficient, indicating that the higher the levels, the higher the yield. It is noteworthy that Sulfuric Acid alone was not significant.

Studies by Ozer and Guçer (2011), Savic et al. (2014) and Zare-Dorabei et al. (2016), involving Pb analyzes, also demonstrated the direct proportionality relation in their response surface models, since the variables were significant and positive coefficients, therefore, the higher their levels, the greater the associated response [42,45,46]. The response surface graph for the maximization of the chemical yield of Pb was elaborated as a function of the NTA and H_2SO_4 dosage, through the OriginPro 9.1.0 software, as shown in Fig. 2 [44].

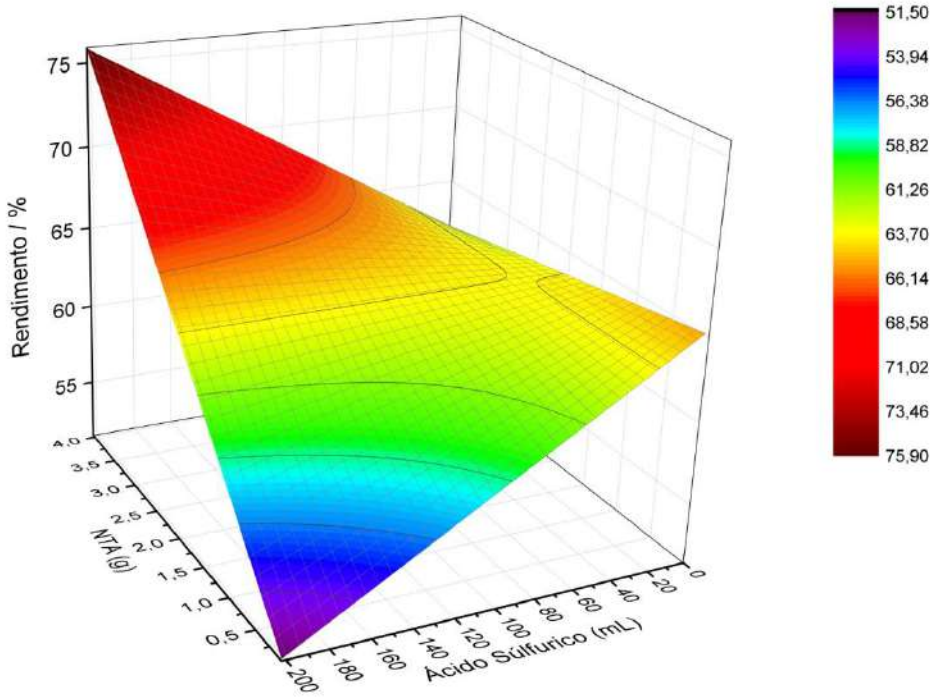

FIGURE 2. RESPONSE SURFACE OBTAINED FOR THE CHEMICAL LEAD YIELD AS A FUNCTION OF THE NTA AND SULFURIC ACID 3 mol.L^{-1} DOSAGES.

Fig. 2 shows that higher concentrations of H_2SO_4 and NTA lead to higher yields, so the optimum condition in which the highest chemical yield of Pb for the range tested would be obtained in the region of 200 ml of H_2SO_4 and 4.0 g of NTA. It is worth mentioning that the current methodology makes the dosage of 2 g of NTA and 50 mL of Sulfuric Acid, which corresponds to a yield of about 62%.

3.2 Validation of the model

The results found for the validation tests of the response surface model for the current dosage (50 ml of H_2SO_4 and 2 g of NTA) and for the new dosage (200 ml of H_2SO_4 and 4 g of NTA) showed that after applying the optimum conditions established by the response surface model obtained there was an increase of up to 32% in the chemical yields of those samples. These results can validate the model found and confirm the significant improvement that the application of the Factorial Design provides to the chemical isolation of Lead and optimizes the yields resulting from the analyzes.

IV. CONCLUSION

- The results of the optimization of the chemical isolation of Pb through the FFD showed that only the H_2SO_4 dosage and the NTA dosage of the isolation methodology influenced the analysis;
- By performing the CCD to obtain the response surface, it was verified that only the variation in the NTA dosage and in the NTA/Sulfuric Acid interaction were significant;
- After the exclusion of the non-significant variables, the response surface showed that the higher the NTA and H_2SO_4 dosage, the higher the associated chemical Pb yield. The optimal condition at which the highest chemical yield of Pb is obtained for the range tested is the region close to 200 ml of H_2SO_4 and 4.0 g of NTA;
- The variable H_2SO_4 dosage alone was not significant in obtaining the response surface, only the NTA/H_2SO_4 association showed influence in the analysis;
- Validation tests of the response surface model showed an increase of up to 32% in the chemical yields of the samples. These results confirm the optimization of the yields that the application of the Factorial Design provided to the chemical isolation of Pb.

ACKNOWLEDGMENTS

The authors thank Indústrias Nucleares do Brasil S.A. for the support offered for the development of the work.

REFERENCES

[1] D.S. Siqueira,"Análise energética e exergética de uma usina nuclear com reator PWR",Msc. Thesis, Federal University of Itajubá, 2016.

[2] K. Vellingiri, K.H. Kim, A. Pournara, A. Deep, "Towards high-efficiency sorptive capture of radionuclides in solution and gas", Progress in Materials Science, vol. 94, pp. 1-67, 2018.

[3] Intergovernmental Panel on Climate Change - IPCC. "Contribution of Working Group III to the Fifth Assessment Report of the Intergovernmental Panel on Climate Change",Available in:
<https://www.ipcc.ch/pdf/assessment-report/ar5/wg3/ipcc_wg3_ar5_full.pdf>. Access in:August 18, 2017.

[4] Y. Fukaya,M. Goto,"Sustainable and safe energy supply with seawater uranium fueled HTGR and its economy". Annals of Nuclear Energy, vol. 99, pp. 19-27, 2017.

[5] K. Saidi, B. Mbarek, "Nuclear energy, renewable energy, CO_2 emissions, and economic growth for nine developed countries: Evidence from panel Granger causality tests", Progress Nuclear Energy vol. 88, pp. 364, 2016.

[6] Empresa de Pesquisa Energética – EPE,"Plano Nacional de Energia 2030: Geração Termonuclear. Ministério de Minas e Energia (MME)",Available in: <http://www.epe.gov.br/PNE/20080512_7.pdf>. Access in: January 11, 2017.

[7] Z.M. Baskurt, C.C. Aydin, "Nuclear power plant site selection by Weighted Linear Combination in GIS environment, Edirne, Turkey", Progress in Nuclear Energy, vol. 104, pp. 85-101, 2018.

[8] A.F.P. Lucena, L. Clarke, R. Schaeffer, A. Szklo, P.R.R. Rochedo, L.P.P. Nogueira, K. Daenzer, A. Gurgel, A. Kitous, T. Kober, "Climate policy scenarios in Brazil: A multi-model comparison for energy", Energy Economics vol. 56, pp. 564, 2016.

[9] R.L.P. Dos Santos, L.P. Rosa, M.C. Arouca, A.E.D. Ribeiro, "The importance of nuclear energy for the expansion of Brazil's electricity grid', ENERGY POLICY, vol. 60, pp. 284-289, 2013.

[10] Eletronuclear, "Panorama da energia nuclear no mundo",Available in:
<http://www.eletronuclear.gov.br/LinkClick.aspx?fileticket=SG_9CnL80wM%3d&tabid=40>. Access in: January 25, 2017.

[11] G. Nyalunga, V. Naicker, M. Toit,"Developing skills for neutronic modelling of nuclear power reactors in South Africa", Journal of energy in Souther Africa, vol. 4, pp. 27, 2016.

[12] A.M. Xavier, A.G. Lima, C.R.M. Vigna, F.M. Verbi, G.G. Bortoleto, K. Goraieb, C.H. Collins, M.I.M.S. Bueno, "Landmarks in the history of radioactivity and current tendencies", Química Nova, vol. 1, pp. 30, 2007.

[13] S.V. Yudintsev, S.V. Stefanovsky, B.S. Nikonov, "A pyrochlore-based matrix for isolation of the REE-actinide fraction of wastes from spent nuclear fuel reprocessing", Doklady Earth Sci., vol. 454, pp. 54-58, 2014.

[14] J.P. Ackerman, L.S.H. Chow, S.M. McDeavitt, C. Pereira, R.H. Woodman, "Isolating wastes in the electrometallurgical treatment of spent nuclear fuel", JOM, vol. 49, pp. 26-28, 1997.

[15] T.B. Kirchner, J.L. Webb, S.B. Webb, R. Arimoto, D.A. Schoep, B.D. Stewart, "Variability in background levels of surface soil radionuclides in the vicinity of the US DOE waste isolation pilot plant", J. Environmental Radioactivity, vol. 60, pp. 275-291, 2002.

[16] S. Ullah, Z. Hussain, S. Mahboob, K. Al-ghanin, "Heavy Metals in Garragotyla, Cyprinuscarpio and Cyprinionwatsoni from the River Panjkora, District, Lower Dir, Khyber Pakhtunkhwa, Pakistan", Brazilian Archives of Biology and Technology, vol. 59, 2016.

[17] S.M.S.G. Nascimento, A.P. Souza, V.L.A. Lima, C.W.A. Nascimento, J.J.V.R. Nascimento, "Phytoextractor Potential of Cultivated Species in Industrial Area Contaminated by Lead", Revista. Brasileira de Ciência do Solo, vol. 40, 2016.

[18] F.R. Moreira, J.C. Moreira, "Os efeitos do chumbo sobre o organismo humano e seu significado para a saúde", Revista Panamericana de Salud Publica, vol. 15, pp. 119, 2004.

[19] Z. Said, A.A. Alshehhi, A. Mehmood, "Predictions of UAE's renewable energy mix in 2030", Renewable Energy, vol. 118, pp. 779-789, 2018.

[20] C.C. Azubuike, C.B. Chikere, G.C. Okpokwasili, "Bioremediation techniques-classification based on site of application: principles, advantages, limitations and prospects", World J. Microbiol. Biotechnol., vol. 32, 2016.

[21] N. Velmurugan, G. Hwang, M. Sathishkumar, T.K. Choi, K.J. Lee, B.T. Oh, Y.S. Lee, "Isolation, identification, Pb(II) biosorption isotherms and kinetics of a lead adsorbing Penicillium sp. MRF-1 from South Korean mine soil", J. Environmental Sci., vol. 22, pp. 1049-1056, 2010.

[22] X. Luo, X.C. Zeng, Z. He, X. Lu, J. Yuan, J. Shi, M. Liu, Y. Pan, Y.X. Wang, "Isolation and characterization of a radiation-resistant bacterium from Taklamakan Desert showing potent ability to accumulate Lead (II) and considerable potential for bioremediation of radioactive wastes", Ecotoxicology, vol. 23, pp. 1915-1921, 2014.

[23] Y.J. Park, Y.C. Lee, W.S. Shin, SJ Choi, "Adsorptive removal of cobalt, strontium and cesium using AMP-PAN in laundry wastewater from nuclear power plant", Abstracts of Papers of the American Chemical Society, vol. 237, pp. 193, 2009.

[24] R. Zarrougui, R. Mdimagh, N. Raouafi, "Highly efficient extraction and selective separation of uranium (VI) from transition metals using new class of undiluted ionic liquids based on H-phosphonate anions", J. Hazardous Mat., vol. 342, pp. 464-476, 2018.

[25] Ministério do Meio Ambiente - Conselho Nacional do Meio Ambiente, "Resolução n° 430, de 13 de maio de 2011",Available in: <http://www.mma.gov.br/port/conama/legiabre.cfm?codlegi=646>. Access in: September 8, 2017.

[26] K.L. Plathe, F.V.D. Kammer, M. Hassello, J.N. Moore, M. Murayama, T. Hofmann, M.F. Hochella Jr, "The role of nanominerals and mineral nanoparticles in the transport of toxic trace metals: Field-flow fractionation and analytical TEM analyses after nanoparticle isolation and density separation", Geochimica et Cosmochimica Acta, vol. 102, pp. 213-225, 2013.

[27] Y. PAN, M.E. FLEET, N.D. MACRAE, "Late alteration in titanite (CaTiSiOS): Redistribution and remobilization of rare Earth elements and implications for U/Pb and Th/Pb geochronology and nuclear waste disposal", Geochimica et Cosmochimica Acta, vol. 57, pp. 355-367, 1993.

[28] J. Huang, K. Nara, C. Lian, K. Zong, K. Peng, S. Xue, Z. Shen, "Ectomycorrhizal fungal communities associated with Masson pine (Pinus massoniana Lamb.) in Pb-Zn mine sites of central south China", Mycorrhiza, vol. 22, pp 589-602, 2012.

[29] E.S. Eitrheim, "Characterization of wastes pertaining to naturally occurring radioactive materials (NORM) and the nuclear fuel cycle", Msc. Thesis, University of Iowa, 2017.

[30] E.R. Pereira Filho, "Planejamento fatorial em química: Maximizando a obtenção de resultados", 1ª. ed., UFSCAR: São Carlos, 2015.

[31] R.F. Gunst, R.L. Mason, "Fractional factorial design", Wiley Online Library, vol. 1, pp. 234-244, 2009.

[32] N. AlMasoud, E. Correa, D.K. Trivedi, R. Goodacre, "Fractional Factorial Design of MALDI-TOF-MS Sample Preparations for the Optimized Detection of Phospholipids and Acylglycerols", Anal. Chem., vol. 88, pp 6301-6308, 2016.

[33] J.A. Barminko, N.I. Nativ, R. Schloss, M.L. Yarmush, "Fractional factorial design to investigate stromal cell regulation of macrophage plasticity", Wiley Online Library, vol. 111, pp. 2239-2251, 2014.

[34] J. Yu, Q. Wang, Z. Zhang, X. Li, "Multi-objective optimizations of multidirectional forming mold based on fractional factorial design", The International J. Advanced Manufacturing Technol., vol. 88, pp 1151-1160, 2017.

[35] M.W.M. Cunico, M.M. Cunico, O.G. Miguel, S.F. Zawadzki, P. Peralta-Zamora, N. Volpato, "Planejamento fatorial: uma ferramenta estatística valiosa para a definição de parâmetros experimentais empregados na pesquisa científica", Visão Acadêmica, vol. 1, pp. 9, 2008.

[36] S. Olivier, V.L. Silva, M. Motta, J.E. Silva, "Emprego de planejamento fatorial no desenvolvimento de uma metodologia para extração de zinco de resíduos galvânicos", Química nova, vol. 7, pp. 30, 2007.

[37] A. Rai, B. Mohanty, R. Bhargava, "Supercritical extraction of sunflower oil: A central composite design for extraction variables", Food Chemistry, vol. 192, pp. 647-659, 2016.

[38] P. Izadiyan, B. Hemmateenejad, "Multi-response optimization of factors affecting ultrasonic assisted extraction from Iranian basil using central composite design", Food Chemistry, vol. 190, pp. 864-870, 2016.

[39] J. Meijide, E. Rosales, M. Pazos, M.A. Sanromán, "p-Nitrophenol degradation by electro-Fenton process: Pathway, kinetic model and optimization using central composite design", Chemosphere, vol. 185, pp. 726-736, 2017.

[40] F. Nemati, R. Zare-Dorabei, M. Hosseini, M.R. Ganjali, "Fluorescence turn-on sensing of thiamine based on Arginine - functionalized graphene quantum dots (Arg-GQDs): Central composite design for process optimization", Sensors and Actuators B: Chemical, vol. 255, pp. 2078-2085, 2018.

[41] Minitab, versão 16.2.4.4, "Statiscal Software", Minitab Inc., 2013.

[42] E.T. Ozer, S. Guçer, "Central composite design for the optimisation of Cd and Pb determination in PVC materials by atomic absorption spectrometry after Kjeldahl digestion", Polymertesting, vol. 30, pp. 773, 2011.

[43] H. Sakurai, J. Noro, A. Kawase, M. Fujinami, K. Oguma, "Digestion of plastic materials for the determination of toxic metals with a microwave oven for house hold use", Anais. Sci., vol. 22, pp. 225, 2006.

[44] OriginPro, versão 9.1.0, "Data analysis and graphing software", Origin Lab Corporation, 1991-2013.

[45] I.M. Savic, S.T. Stojiljkovic, D.G. Gajic, "Modeling and optimization of energy-efficient procedures for removing lead(II) and zinc(II) ions from aqueous solutions using the central composite design", Energy vol. 77, pp. 66, 2014.

[46] R. Zare-Dorabei, S.M. Ferdowsi, A. Barzin, A. Tadjarodi, "Highly efficient simultaneous ultrasonic-assisted adsorption of Pb(II),Cd(II), Ni(II) and Cu (II) ions from aqueous solutions by graphene oxidemodified with 2,20-dipyridylamine: Central composite designoptimization", Ultrasonics Sono Chemistry, vol. 32, pp. 265, 2016.

Image Based Visual Servoing for Omnidirectional Wheeled Mobile Robots in Voltage Mode

Armando Saenz[1], Victor Santibañez[2], Eusebio Bugarin[3]

[1,2]Tecnológico Nacional de México - Instituto Tecnológico de la Laguna, Blvd. Revolucion y Av. Instituto Tecnologico de La Laguna S/N Torreon Coah., Mexico. CP 27000

[3]Tecnologico Nacional de Mexico - Instituto Tecnologico de Ensenada, Blvd. Tecnologico No. 150, Ex-ejido Chapultepec, 22780 Ensenada, B.C.

Abstract*—This paper presents a new image based visual servoing (IBVS) control scheme for omnidirectional wheeled mobile robots with four swedish wheels. The contribution is the proposal of a scheme that consider the overall dynamic of the system; this means, we put together mechanical and electrical dynamics. The actuators are direct current (DC) motors, which imply that the system input signals are armature voltage applied to DC motors. In our control scheme the PD control law and eye-to-hand camera configuration are used to compute the armature voltages and to measure system states, respectively. Stability proof is performed via Lypunov direct method and LaSalle's invariance principle. Simulation and experimental results were performed in order to validate the theoretical proposal and to show the good performance of the posture errors.*

Keywords—IBVS, posture control, omnidirectional wheeled mobile robot, dynamic actuator, Lyapunov direct method.

I. INTRODUCTION

Wheeled mobile robots (WMR) are robotic systems with free motion in a plane, and they have capacity to reach every position on the same plane. WMR issues are about how to move them, because they may have or not may have limited trajectories to perform. In our case, we are going to study the omnidirectional mobile robots (OMR)[1] whose trajectories are not limited. In a more particular way, it is emphasized in OMR with four swedish wheels [2]. The methodology proposed in [3], was chosen to obtain the dynamic model, together with the direct current (DC) motor equations presented in [4].

In order to acquire WMR posture by means of computer vision, it is possible to implement global vision systems (GVS). The GVS fits in the *intelligent space* concept [5], [6]. An intelligent space is comprised by sensors (e.g. cameras, microphones, ultrasound or laser range finder), computer, actuators and communication devices. The sensors are used to identificate and track the objects in the space and/or to receive orders from operators. The computer acquires information from sensors, performs image processing, computes control law and communicates with actuators. The intelligent space interacts with objects through robotic platforms (e.g. WMR) that provide services like carrying or delivering loads. GVS are used in robotics soccer competitions to acquire the posture of every robot on the playground [7], [8]. So, GVS are a good option to obtain the posture measurement of WMR.

The contribution of our paper is the proposal of a new control scheme to OMR posture control in voltage mode, requiring only vision system measurements. Furthermore, in our control scheme, the DC motors do not require encoders or drivers with current loop or velocity loop. Document is structured as follow. Section 2 presents the problem statement and the dynamic model in image space too. Control law and stability proof is presented in Section 3. Simulation and experimental results are showed in Section 4. Finally, Section 5 shows our conclusions.

II. PROBLEM STATEMENT

First, the dynamic model of the OMR including actuator dynamics is presented. After, camera model (*thin lens*[9]) and camera configuration (*Eye-to-Hand*[10]) are explained.

2.1 Dynamic model

Consider an OMR with a two dimensional cartesian coordinate frame called Σ_W whose center is O_W and its axes are labeled as $W_1$and W_2. These axes describe a plane where the OMR has free motion. OMR posture on the plane is denoted by $\boldsymbol{\xi} = [x\ y\ \theta]^\top$ (seeFig.1).

Let$\dot{\boldsymbol{\xi}} \in \mathbb{R}^{\boldsymbol{3}}$ and $\ddot{\boldsymbol{\xi}} \in \mathbb{R}^3$are the velocity and acceleration vector of the OMR respectively,$\boldsymbol{u} = [u_1 \quad u_2 \quad u_3 \quad u_4]^\top$ isthe armature voltages vector applied to DC motors. The wheels and actuators (DC motors) are labeled as it is depicted in

Fig.2**Error! Reference source not found.**.The dynamic model is an Euler-Lagrange system, given by the following state space representation:

$$\frac{d}{dt}\boldsymbol{\xi} = \dot{\boldsymbol{\xi}} \tag{1}$$

$$\frac{d}{dt}M\dot{\boldsymbol{\xi}} = \frac{k_a}{R_a}R_R^W(\theta)E^\top \boldsymbol{u} - C(\dot{\theta})\dot{\boldsymbol{\xi}} - D\dot{\boldsymbol{\xi}} \tag{2}$$

Where $M \in \mathbb{R}^{3\times3}$ is the diagonal positive definite inertia matrix, $C: \mathbb{R} \to \mathbb{R}^{3\times3}$ is the skew-symmetric gyroscopic matrix, $D \in \mathbb{R}^{3\times3}$ is the symmetric damping matrix, $E \in \mathbb{R}^{4\times3}$ is the jacobian matrix, $R_R^W(\theta)$ is the rotation matrix from Σ_R to Σ_W, $R_a \in \mathbb{R}$ is the armature resistance constant and $k_a \in \mathbb{R}$ is the torque constant for each DC motor.

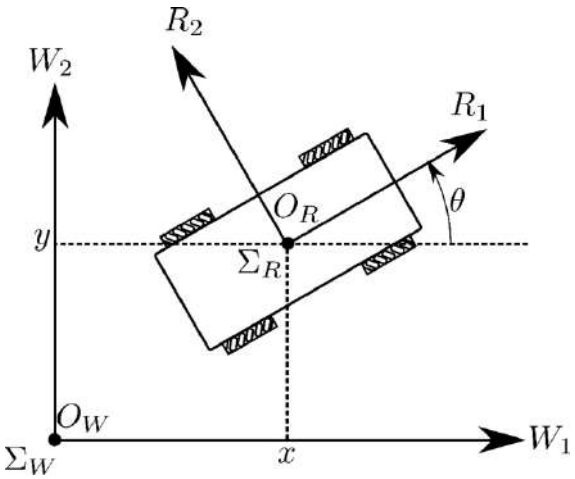

FIG.1: OMR free body diagram

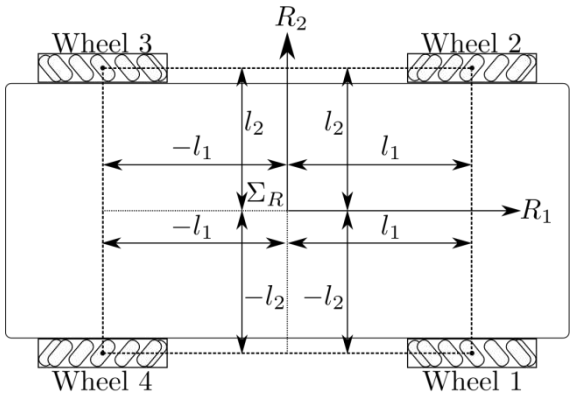

FIG.2: Wheel configuration

2.2 Camera model

Consider the scene depicted in Fig.3. The camera is fixed on the ceiling and oriented to see the robot. The configuration of the camera in Fig.3 is called Eye-to-Hand, in the literature[10]. A photoelectric sensor inside of the camera acquires the scene image. In order to obtain the construction model of the scene image, it is necessary to have the knowledge of *extrinsic parameters* and *intrinsic parameters*. First, the coordinate frame $\Sigma_C$is engaged on the sensor surface, the distance Z_{C3} and angle$\gamma$of $\Sigma_c$respect to Σ_W are the *extrinsic parameters*. Let $\lambda \in \mathbb{R}_+$ be the distance between camera lens and photoelectric sensor, $\alpha_u, \alpha_v \in \mathbb{R}_+$ be the constants that convert from cartesian space to image space. These latter parameters are called: *intrinsic parameters*.

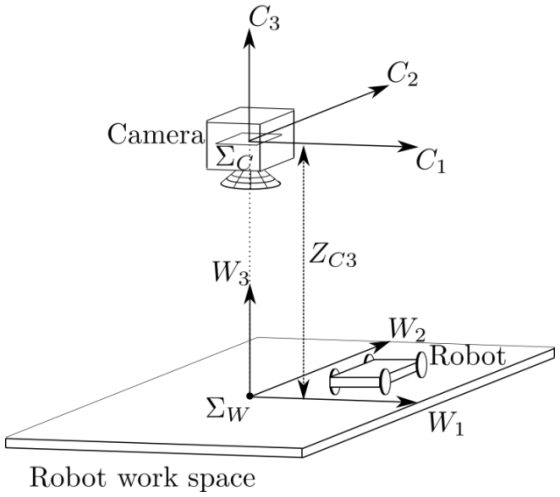

FIG.3: Configuration *Eye-to-Hand*

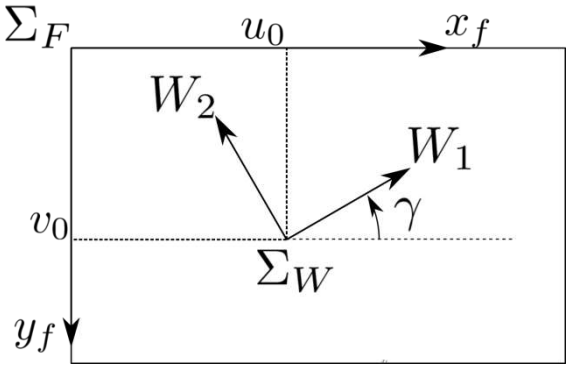

FIG.4: Computer screen

In order to convert from cartesian space to image space (see Fig.4), we define $\boldsymbol{\xi}_f \in \mathbb{R}^3$ forthe OMR posture in image space and it is obtained as follow:

$$\boldsymbol{\xi}_f = \begin{bmatrix} x_f \\ y_f \\ \theta_f \end{bmatrix} = K_C R_W^F(\theta_c) \begin{bmatrix} x \\ y \\ \theta + \gamma \end{bmatrix} \tag{3}$$

With

$$K_c = \begin{bmatrix} \frac{\alpha_u \lambda}{Z_{c3} - \lambda} & 0 & 0 \\ 0 & \frac{\alpha_v \lambda}{Z_{c3} - \lambda} & 0 \\ 0 & 0 & 1 \end{bmatrix}, \qquad R_W^F(\gamma) = \begin{bmatrix} \cos(\gamma) & -\sin(\gamma) & 0 \\ -\sin(\gamma) & -\cos(\gamma) & 0 \\ 0 & 0 & 1 \end{bmatrix}.$$

In order to express the dynamic model (1) and (2) in image space, first and second time derivatives from (3) are computed as follow:

$$\dot{\boldsymbol{\xi}}_f = \begin{bmatrix} \dot{x}_f \\ \dot{y}_f \\ \dot{\theta}_f \end{bmatrix} = K_C R_W^F(\gamma) \dot{\boldsymbol{\xi}}, \qquad \ddot{\boldsymbol{\xi}}_f = \begin{bmatrix} \ddot{x}_f \\ \ddot{y}_f \\ \ddot{\theta}_f \end{bmatrix} = K_C R_W^F(\gamma) \ddot{\boldsymbol{\xi}}. \tag{4}$$

Solving for $\dot{\boldsymbol{\xi}}$y $\ddot{\boldsymbol{\xi}}$, we have

$$\dot{\boldsymbol{\xi}} = K_C^{-1} R_F^W(\gamma) \dot{\boldsymbol{\xi}}_f, \qquad \ddot{\boldsymbol{\xi}} = K_C^{-1} R_F^W(\gamma) \ddot{\boldsymbol{\xi}}_f \tag{5}$$

where $R_F^W(\gamma) = \left(R_W^F(\gamma)\right)^\top$. Pre-multiplying (2) with $R_W^F(\gamma)$and substituting equation (5) the state space representation is rewritten as follows:

$$\frac{d}{dt} \boldsymbol{\xi}_f = \dot{\boldsymbol{\xi}}_f \tag{6}$$

$$\frac{d}{dt} M K_C^{-1} \dot{\boldsymbol{\xi}}_f = \frac{k_a}{R_a} R_R^F(\theta_f) E^\top \boldsymbol{u} - C(\dot{\theta}) K_C^{-1} \dot{\boldsymbol{\xi}}_f - D K_C^{-1} \dot{\boldsymbol{\xi}}_f \tag{7}$$

with

$$R_R^F(\theta_f) = \begin{bmatrix} \cos(\theta_f) & -\sin(\theta_f) & 0 \\ -\sin(\theta_f) & -\cos(\theta_f) & 0 \\ 0 & 0 & 1 \end{bmatrix}.$$

Note that (6) and (7) are the open loop dynamic model of a time invariant system, the input signal $\boldsymbol{u}$ is a vector with the four armature voltage of actuators; and the mechanical, electrical and camera parameters are involved in (7).

III. POSTURE CONTROL

3.1 Controller

Let $\boldsymbol{\xi_f^*} \in \mathbb{R}^3$ be the desired posture vector in image space,$\tilde{\boldsymbol{\xi}}_{\boldsymbol{f}} \triangleq \boldsymbol{\xi_f^*} - \boldsymbol{\xi_f}$be the posture error vector. The aim of our proposed control scheme is to lead the posture error toward zero (i.e. $\lim_{t \to \infty} \tilde{\boldsymbol{\xi}} = 0$). The proposed control law is given by

$$\boldsymbol{u} = G R_R^F(\theta_f) \left[K_p \tilde{\boldsymbol{\xi}}_f - K_d \dot{\boldsymbol{\xi}}_f \right] \tag{8}$$

with

$$G = \begin{bmatrix} 1 & 1 & 1 \\ 1 & -1 & -1 \\ 1 & 1 & -1 \\ 1 & -1 & 1 \end{bmatrix}, \qquad K_p = \begin{bmatrix} k_{p1} & 0 & 0 \\ 0 & k_{p2} & 0 \\ 0 & 0 & k_{p3} \end{bmatrix}, \qquad K_d = \begin{bmatrix} k_{d1} & 0 & 0 \\ 0 & k_{d2} & 0 \\ 0 & 0 & k_{d3} \end{bmatrix},$$

where $k_{p1}, k_{p2}, k_{p3}, k_{d1}, k_{d2}, k_{d3} \in \mathbb{R}$ are positive gains. Substituting the control law (8) in dynamic model (7) we obtain closed loop dynamics. It is shown as follows

$$\frac{d}{dt}\tilde{\boldsymbol{\xi}}_f = -\dot{\boldsymbol{\xi}}_f \tag{9}$$

$$\frac{d}{dt}MK_C^{-1}\dot{\boldsymbol{\xi}}_f = \Lambda\left[K_p\tilde{\boldsymbol{\xi}}_f - K_d\dot{\boldsymbol{\xi}}_f\right] - C\left(\dot{\theta}\right)K_C^{-1}\dot{\boldsymbol{\xi}}_f - DK_C^{-1}\dot{\boldsymbol{\xi}}_f \tag{10}$$

With $\Lambda = \frac{k_a}{R_a}R_R^F\left(\theta_f\right)E^T G R_R^F(\theta_f) = \frac{k_a}{R_a}E^\top G$ a diagonal positive definite matrix. The closed loop dynamics (9)-(10) has a unique equilibrium in $\tilde{\boldsymbol{\xi}}_{\boldsymbol{f}} = \mathbf{0} \in \mathbb{R}^3and\dot{\boldsymbol{\xi}}_f = \mathbf{0} \in \mathbb{R}^3$.

3.2 Stability proof

The control law (8) is a PD control law to been implemented in over actuated systems (the number of the degree of freedom is lower than the number of actuators or number of control signals). In order to demonstrate stability of the equilibrium, we use the following Lyapunov function candidate

$$V\left(\tilde{\boldsymbol{\xi}}_f, \dot{\boldsymbol{\xi}}_f\right) = \frac{1}{2}\dot{\boldsymbol{\xi}}_f^\top MK_C^{-1}\dot{\boldsymbol{\xi}}_f + \frac{1}{2}\tilde{\boldsymbol{\xi}}_f^\top \Lambda K_p\tilde{\boldsymbol{\xi}}_f \tag{11}$$

whose total time derivative along of the trajectories of the closed loop equations (9) and (10) is:

$$\dot{V}\left(\tilde{\boldsymbol{\xi}}_f, \dot{\boldsymbol{\xi}}_f\right) = -\dot{\boldsymbol{\xi}}_f^\top(\Lambda K_d + D)\dot{\boldsymbol{\xi}}_f \tag{12}$$

By satisfying the inequality $\Lambda K_d + D > 0$, the equilibrium stability is guaranteed. Thus, in order to study asymptotic stability we can apply the LaSalle's invariance principle [11]. Toward this end, notice that in the set

$$\boldsymbol{S} = \left\{\begin{bmatrix}\tilde{\boldsymbol{\xi}}_f \\ \dot{\boldsymbol{\xi}}_f\end{bmatrix} : \dot{\boldsymbol{V}}\left(\tilde{\boldsymbol{\xi}}_f, \dot{\boldsymbol{\xi}}_f\right) = \mathbf{0}\right\} = \left\{\tilde{\boldsymbol{\xi}}_f \in \mathbb{R}^3 \text{and} \dot{\boldsymbol{\xi}}_f = \mathbf{0} \in \mathbb{R}^{\mathbf{3}}\right\} \tag{13}$$

the largest invariant set $\overline{\boldsymbol{S}}$ is the origin of the closed loop system (9)-(10); i.e., $\overline{\boldsymbol{S}} = \left\{\tilde{\boldsymbol{\xi}}_f = \mathbf{0} \in \mathbb{R}^3 \text{and} \dot{\boldsymbol{\xi}}_f = \mathbf{0} \in \mathbb{R}^{\mathbf{3}}\right\}$. So, in accordance with the Corollary 4.2 of[11](see page 129 of [11]) the equilibrium $\left[\tilde{\boldsymbol{\xi}}_f \quad \dot{\boldsymbol{\xi}}_{\boldsymbol{f}}\right]^\top = [\mathbf{0} \quad \mathbf{0}]^\top \in \mathbb{R}^6$ is globally asymptotically stable.

IV. SIMULATIONS AND EXPERIMENTAL RESULTS

Our proposed control scheme is depicted in FIG.5. Simulation was performed in MatLab/Simulink. Used notation and parameter values, are shown in TABLE 1. The dynamic model matrices are as follow:

$$M = \text{diag}\{m_R + 4\,m_{R1},\, m_R + 4\,m_{R1}, 4\,(m_{R1}l_1^2 + m_{R1}l_2^2 + I_{Rz1}) + I_{Rz}\} + \left(I_{Ry1} + J_m r_e^2\right)E^\top E$$

$$E = \frac{1}{r}\begin{bmatrix}1 & 1 & L\\ 1 & -1 & -L\\ 1 & 1 & -L\\ 1 & -1 & L\end{bmatrix}, \quad C\left(\dot{\theta}\right) = \left(\frac{4}{r^2}I_{Ry1} + J_m r_e^2\dot{\theta}\right)B, D = r_e^2\left(\frac{k_a k_b}{R_a} + k_v\right)E^\top E,$$

$$B = \begin{bmatrix}0 & -1 & 0\\ 1 & 0 & 0\\ 0 & 0 & 0\end{bmatrix}, \qquad L = l_1 + l_2\,.$$

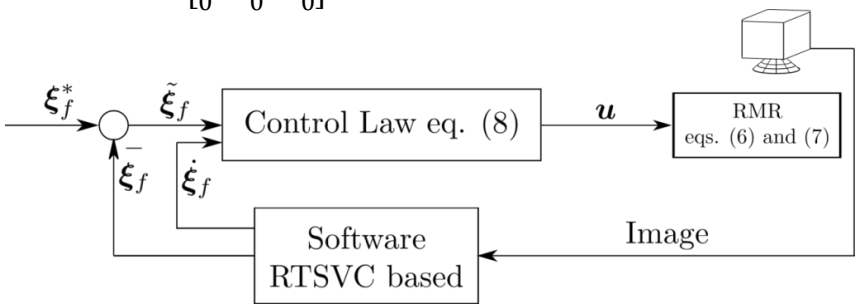

FIG.5: PROPOSED CONTROL SCHEME

Experimental results were performed with a RTSVC based software[12] in order to capture and process the images; the desired posture vector is $\boldsymbol{\xi}_f^* = [43 \quad 53 \quad 0]^\top$ with initial condition given by$\boldsymbol{\xi}_{f0} = [280 \quad 210 \quad 176]^\top$. Gain values are

$k_{p1} = 0.5,\ k_{p2} = 0.5,\ k_{p3} = 10.0,\ k_{d1} = 0.005,\ k_{d2} = 0.005$ and $k_{d3} = 1$. The experiment was carried out during 10 seconds with a sample time of 10 milliseconds. Obtained results are depicted in FIG.6, where blue lines are the reference, red lines are the experimental results and green lines are the simulation results. The position (i.e. x_f and y_f) achieves the reference in simulation and experimentation in 1.5 seconds and 3 seconds, respectively. In contrast, the simulation result in orientation (i.e., θ_f) is achieved around 2.5 second and the experimental result has a steady value error reached at 4 seconds, because voltage armature computed by the control law is lower for moving the OMR; this is due to the non-modeled static friction in the DC motor axes. FIG.7 shows the accomplished path, where red dots represent the position of OMR geometric center and green dots represent the position of OMR front part.

TABLE 1
MECHANICAL AND ELECTRICAL PARAMETERS

Parameter	Symbol	Value	Units
Mass of the body	m_R	2.8	Kg
Mass of the wheels	m_{R1}	0.38	Kg
Inertia of the body	I_{Rz}	0.060848	$\text{Kg} - \text{m}^2$
Wheels inertia in axis rotor	I_{Ry1}	0.000324	$\text{Kg} - \text{m}^2$
Wheels inertial in perpendicular axis rotor	I_{Rz1}	0.000469	$\text{Kg} - \text{m}^2$
Distance in R_1	l_1	0.1524	m
Distance in R_2	l_2	0.1505	m
Wheels radius	r	0.42	m
Rotor Inertia	J_m	5.7×10^{-7}	$\text{Kg} - \text{m}^2$
Back-EMF Constant	k_b	0.01336	$\text{N s}/\text{rad}$
Torque Constant	k_a	0.0134	$\text{N m}/\text{A}$
Armature resistance	R_a	1.9	Ω
Viscous friction	k_v	0.001	$\text{N m s}/\text{rad}$
Gear ratio	r_e	64	1

V. CONCLUSIONS

We have presented a new IBVS scheme for OMR with four swedish wheels. The PD control law was implemented with errors in image space. Stability was proven via Lyapunov direct method, and globally asymptotically stability of the closed loop system was established by using the LaSalle's invariance principle. Positive PD gains of the controller are sufficient to guarantee asymptotic stability in accordance with the stability proof. Simulations show satisfactory results because the states achieved the desired states. Experimental results show a steady state error in the orientation variable, the position reaches to desired position. Steady state error is due to non-modeled static friction in the DC motors axes. As long as, the states are brought closer to desired states, the computed armature voltage by control law decreases. The above implies that the voltage is insufficient to move the remaining angle. A possible solution could be to implement functions like hyperbolic tangent to keep a higher voltage near of desired posture.

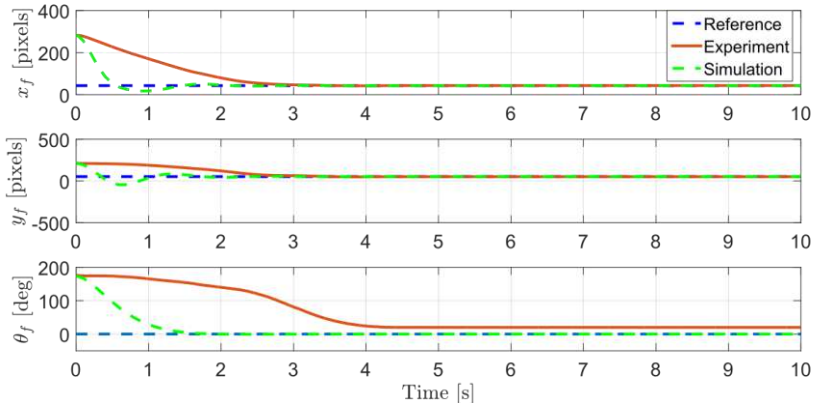

FIG.6: SIMULATION AND EXPERIMENTAL RESULTS

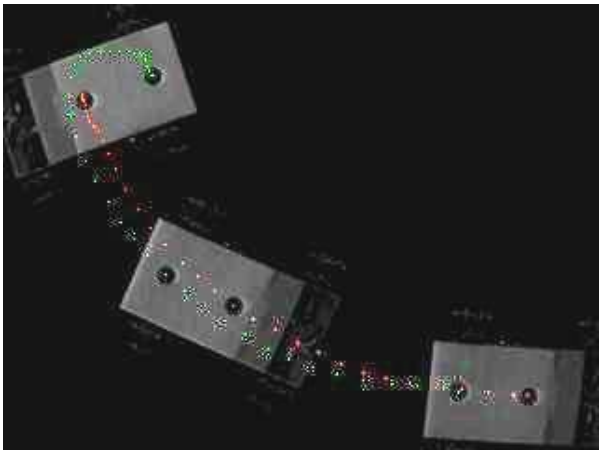

FIG.7 PERFORMED PATH ACQUIRED BY THE CAMERA

ACKNOWLEDGEMENTS

This project has been partially supported by the TecNM, PRODEP and CONACYT 134534 projects.

REFERENCES

[1] K. Watanabe, "Control of an omnidirectional mobile robot," in *Second International conference on Knowledge-Based Intelligent Electronic System*, 1998, no. April, pp. 503–508.

[2] B. E. Ilon, "Wheels for a course stable selfpropelling vehicle movable in any desired direction on the ground or some other base," 3876255, 1972.

[3] G. Campion, G. Bastin, and B. D'Andréa-Novel, "Structural Properties and Classification of Kinematic and Dynamic Models of Wheeled Mobile Robots," *IEEE Trans. Robot. Autom.*, vol. 12, no. 1, pp. 47–62, 1996.

[4] R. Kelly, V. Santibañez, and A. Loría, *Control of Robot Manipulator in Joint Space*. Springer, 2005.

[5] H. Hashimoto, "Present state and future of Intelligent Space - Discussion on the implementation of RT in our environment," *Artif. Life Robot.*, vol. 11, no. 1, pp. 1–7, 2007.

[6] J. H. Lee and H. Hashimoto, "Intelligent space - Concept and contents," *Adv. Robot.*, vol. 16, no. 3, pp. 265–280, 2002.

[7] M. Brezak, I. Petrović, and E. Ivanjko, "Robust and accurate global vision system for real time tracking of multiple mobile robots," *Rob. Auton. Syst.*, vol. 56, no. 3, pp. 213–230, 2008.

[8] M. Brezak and I. Petrovic, "Global Vision Based Tracking of Multiple Mobile Robots in Subpixel Precision," *2007 5th IEEE Int. Conf. Ind. Informatics*, pp. 473–478, 2007.

[9] R. Kelly, "Robust asymptotically stable visual servoing of planar robots," *IEEE Trans. Robot. Autom.*, vol. 12, no. 5, pp. 759–766, 1996.

[10] S. Hutchinson, G. D. D. Hager, and P. I. I. Corke, "A Tutorial on Visual Servo Control," *IEEE Trans. Robot. Autom.*, vol. 12, no. Octubre, pp. 651–670, 1996.

[11] H. K. Khalil, *Nonlinear Systems*, 3a ed. 2002.

[12] E. Bugarin and R. Kelly, "RTSVC: Real-time system for visual control of robots," *Int. J. Imaging Syst. Technol.*, vol. 18, no. 4, pp. 251–256, 2008.

Determination of 3-chloropropanediol in soy sauce samples by liquid phase extraction coupled with microwave-assisted derivatization and high performance liquid chromatography-ultraviolet detection

Hui-Ying Chung[1], Vinoth Kumar Ponnusamy[2], Jen-Fon Jen[3]*

[1,2,3]Department of Chemistry, National Chung Hsing University, Taichung 402, Taiwan
[2]Department of Medicinal and Applied Chemistry, Kaohsiung Medical University, Kaohsiung, 807 Taiwan.

Abstract**—***3-Chloro-1,2-propanediol (3-chloropropanediol) is a well-known food processing contaminant found in a wide range of foods and ingredients and there has been recent concern about the levels of carcinogenic 3-chloropropanediol (3-MCPD) in some soy sauces. This paper reports on the development of an analytical method for the fast determination of 3-MCPD at trace level in commercial soy sauce using novel liquid phase extraction (LPE)/cleanup coupled with microwave-assisted derivatization (MAD) method followed by high performance liquid chromatography-ultraviolet (HPLC-UV) detection. In this method, 3-MCPD was first isolated from soy sauce sample matrix by LPE/cleanup with Extrude NT3 column cartridges and the isolated (eluent) solution was subjected to MAD with acetophenone to form 2-methyl-2-phenyl-4-(chloromethyl)-1,3-dioxolane under microwave irradiation using a specially modified domestic microwave oven, then the derivatizeddioxolane was directly analyzed with a HPLC-UV system. The optimum conditions for MAD such as the ratio of reagents, acidic catalyst, microwave irradiation power and time, as well as the chromatographic conditions were thoroughly investigated. Experimental results indicated that maximum derivatization can be achieved in 10 min under microwave irradiation at 362 watts when compared to 18 hours by conventional refluxing reaction. The proposed method provided a simple and rapid analytical procedure for 3-MCPD analysis in soy sauce with the detection limit of 80 ng mL-1. The relative standard deviations were all below 3.0 % (n = 7). Application was illustrated by the analysis of commercial sauce sample obtained from a local traditional store in central Taiwan.*

Keywords—3-Chloropropanediol,liquid phase extraction,microwave-assisted derivatization,sample preparation, soy sauce.

I. INTRODUCTION

Chlorinated propanols are toxic compounds, often found in various foods containing protein hydrolysates, like seasonings and savoury food products. 3-chloro-1,2-propanediol (3-MCPD) is a well known contaminant, which was first identified in 1982 in various foods [1-3]. It has been classified as non-genotoxic carcinogen but its carcinogenic potential in rodents has been controversial. 3-MCPD presented in certain oriental soy sauces and oyster sauces has triggered considerable public health and consumer safety concerns in recent years [4]. Its occurrence in hydrolyzed vegetable proteins (HVP) is related to the production process that uses acid hydrolysis and as a result of the high temperature chlorination of lipids present in the protein starting materials [5-6]. It is a suspected carcinogen in assays [7]. Because of its toxicity, several countries had set maximum levels for 3-MCPD in food products. In China and Canada, 3-MCPD is found to contain up to 177.5 mg L-1 in soy sauces. The maximum permission limit of 1 mg L-1 for 3-MCPD in HVP and soy sauces has been set in USA and Japan, and the same limit has been stipulated in Taiwan [8-12].

Most analytical methods for determining 3-MCPD are based on gas chromatography (GC) with different detectors such as flame ionization detector [13], electron capture detector [14] and mass spectrometry (MS) [12,15-20]. The Association of Official Analytical Chemists (AOAC) has published a method for the extraction, separation and identification of 3-MCPD in foods and ingredients using GC-MS [21]. Prior to GC analysis, appropriate sample pretreatment steps are usually required to clean up and enrich the target species, as well as the derivatization reactions with powerful agents such as acetone [18], n-butaneboronic acid [22], phenylboronic acid [13], and heptafluorobutyrylimidazole[14], etc. Although these methods offer

efficient and precise results, they are relatively time-consuming and relative expensive with respect to the derivated agent. Moreover, GC-MS is an expensive instrument and not popular in the soy sauce industries. Recently Lam et al. [23] used molecular imprint-based (MIP) chemosensor as semi-quantitative analytical tool to screen 3-MCPD in food products. However, the complicate matrix of soy sauce still interfered the binding of 3-MCPD on the MIP sensor.

High performance liquid chromatography-ultraviolet (HPLC-UV) is a widely used instrument with advantages of simplicity, inexpensive, convenient, and has diverse applications. It has potential to be an alternative to GC-MS method for determining 3-MCPD in soy sauce for analytical quality control purpose due to its popularity in food industries. However, to the best of our knowledge, the application of HPLC-UV to determine 3-MCPD has not been reported so far. In general, the high polarity of 3-MCPD limits its retention on a reversed-phase HPLC column and the lack of strong characteristic absorption in UV spectrum limits its detection by an UV detector. Therefore, a derivatization reaction is required to decrease the polarity of 3-MCPD as well as to create a characteristic UV-absorption. For this purpose, in this study, a derivatization reaction with acetophenone to form 2-methyl-2-phenyl-4-(chloromethyl)-1,3-dioxolane was examined to decrease the polarity of 3-MCPD and create a characteristic UV-absorption for HPLC-UV measurement. Moreover, the derivatization reaction by conventional heating/reflux method was usually a time-consuming process, thus the application of microwave irradiation is worth to investigate to speed-up the derivatization reaction. In our previous research publications, we demonstrated novel and rapid sample preparation/derivatization methods based on microwave irradiation and which has been successfully applied for the analysis of several pollutants in different aqueous samples matrix [24-26]. In continuation of our research work, we report here for the first time, a HPLC-UV method coupled to microwave-assisted derivatization (MAD) was established for fast determination of 3-MCPD in soy sauce posterior to the liquid phase column cartridge extraction/clean-up.

II. MATERIALS AND METHODS

2.1 Chemicals and Reagents

Deionized water was produced using a Barnstead Nanopure water system (Barnstead, New York, USA) for all aqueous solutions. All chemicals and solvents were of ACS reagent grade. 3-MCPD was purchased from Fluka (FlukaChemieGmbh, Switzerland), acetophenone was from Acros Organics (Belgium), p-toluenesulfonic acid monohydrate was from Showa Chemicals (Japan), dypnone was from Wako pure chemical industries, LTD (Japan), and Toluene was from Tedia Company (USA). Sodium hydroxide, sodium chloride, ammonium acetate, and diethyl ether were from Riedel-deHäen (Hannover, Germany). Acetonitrile was obtained from Mallinckrodt (Kentucky, USA). Standard stock solutions (1000 μg mL^{-1}) of acetophenone and dypnone were prepared by dissolving 0.100 g in 95 mL acetonitrile and then adding acetonitrile to adjust the volume to 100 mL. The solutions were stored in brown glass bottles, and kept at 4 ºC. Fresh working solutions were prepared daily by appropriate dilution of the stock solutions. The HPLC eluents were prepared as 50% and 80% acetonitrile in 0.01 M ammonium acetate buffer (pH 6.9). The eluents were filtered through a 0.45 μm poly (vinylidene difluoride) (PVDF) membrane filter and degassed ultrasonically. An Extrelut NT3 column (EM Science, Gibbstown, NJ, USA) was used to clean the sample matrix.

2.2 Apparatus and Instrumentation

HPLC used in this work was an Agilent 1100 series system equipped with a vacuum degasser, quaternary pump, and variable wavelength UV detector with a 20-μL flow cell (Agilent, Palo Alto, CA). A Waters reversed-phase LC-18 column (15 cm x 4.6 mm id. 5-μm particle) was used for separation. A Rheodyne 7125 injector (Rohnert Park, CA, USA) was used for sample injection. The detection wavelength was set at 241 nm. The microwave oven used to achieve the derivatization of 2-MCPD was a modified home-made version of the domestic SHARP R-340D system (2450 MHz, SHARP, Taipei, Taiwan) with a maximum power of 650 Watts, equipped with a cooling condenser connecting to tap water [24-25]. After the modification, the powers of microwave were 105, 188, 362, and 502 Watts for weak, medium low, medium, and medium high irradiation, respectively. The MAD system was set-up as shown in **Fig. 1**. In order to keep from the leak of microwave irradiation, aluminum foils was tacked on the inner-wall and the outer-wall of microwave body in the interface part. A microwave leak detector (MD-2000, Less EMF Inc., NY, USA) was used to check the safety aspects before the running.

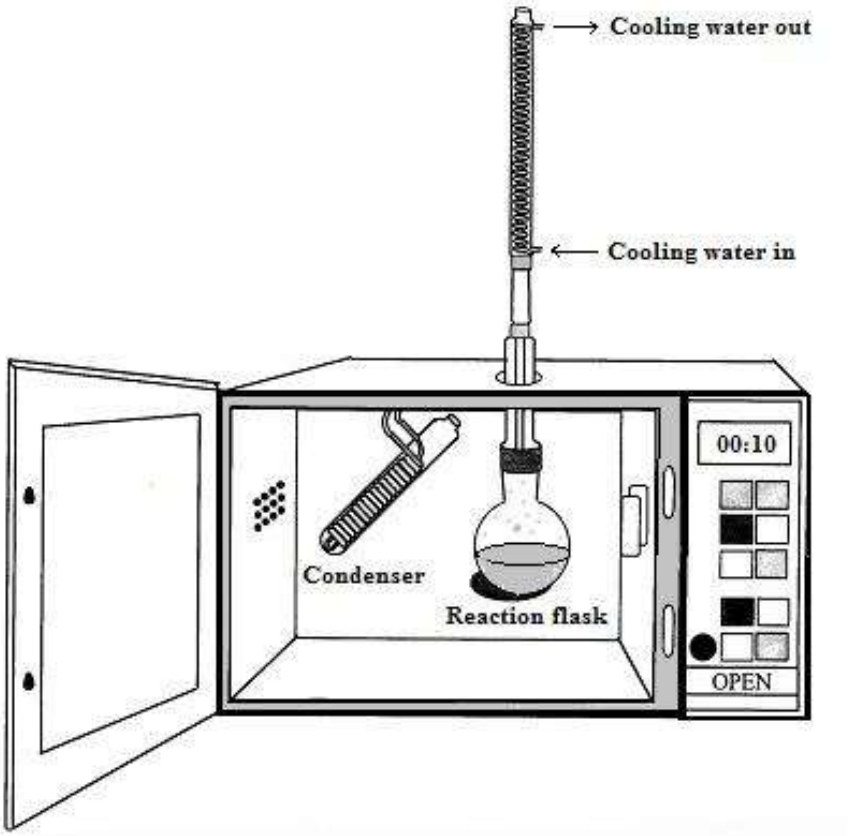

FIGURE 1. Apparatus of the microwave assisted derivatization (MAD) system

2.3 Preparation of calibration solutions of derivateddioxolane

Since the derivatization product 2-methyl-2-phenyl-4-(chloromethyl)-1,3-dioxolane, is not commercial available, varied concentrations of the derivateddioxolane were synthesized by mixing varied volumes of 3-MCPD (12, 24, 47, 95, 190, and 380 μL) and acetophenone in 1:3 weight ratio, respectively, and adding 20 mg of p-toluenesulfonic acid monohydrate in 25 mL toluene under microwave irradiation (362 watts) for 10 min. After cooling to ambient temperature, 10 mL of saturated sodium chloride solution was added and stirred thoroughly. After setting and removing the aqueous phase, the organic phase was made-up to 25 mL with toluene. The working solutions were prepared by diluting 0.1 mL of these solutions to 100 mL with acetonitrile and concentrations were ranged from 0.6 to 20.1 μg mL^{-1} (as 3-MCPD).

2.4 Sample preparation (LPE/clean-up) and MAD

Soy sauce (12 g) was added into a beaker containing 15 mL of saturated sodium chloride. After 10 min mixing and setting into two layers, the upper liquid layer was poured into an Extrelut NT3 cartridge column and allowed to equilibrate for 15 min. The column was eluted with 30 mL of diethyl ether and the eluent was collected in a vial. After removing water by adding anhydrous sodium sulfate, the resulting extract was then evaporated to dryness at room temperature (30 ºC) under nitrogen [27].

The residue in vial was re-dissolved by adding 365 μL of acetophenone and 20 mg of p-toluenesulfonic acid in 25 mL toluene. After mixing thoroughly, the solution was put into microwave oven for derivatization under 362 watts for 10 min. After cooling to ambient temperature, 0.1 M NaOH was used to titrate the solution to pH 7.0 and 10 mL of saturated sodium chloride solution was added and stirred thoroughly. After setting, the aqueous phase was removed and the organic phase was dried with 5 g of anhydrous sodium sulfate and purged with nitrogen to near dryness. The residue was re-dissolved by adding 20 mL of acetonitrile for HPLC analysis (injection volume: 20 μL).

III. RESULTS AND DISCUSSION

3.1 Optimization of HPLC conditions

In the derivatization, in spite of the derivated product, 2-methyl-2-phenyl-4- (chloro-methyl)-1,3-dioxolan, dypnone was also produced through the dimerization of acetophenone. Reactions are shown in **Fig. 2**. Therefore, the optimum chromatographic conditions for resolving acetophenone, dypnone, and 2-methyl-2- phenyl-4-(chloromethyl) -1,3-dioxolane were examined. Results were listed in **Table 1**. Under the conditions, the acetophenone, 2-methyl-2-phenyl-4-(chloromethyl)-1,3-dioxolane, and dypnone were with retention time of 3.81, 11.17, and 27.42, respectively. Obviously, the derivateddioxolane was separated from the derivatization agent and its dimer product. All chromatograms were virtually free of any interference.

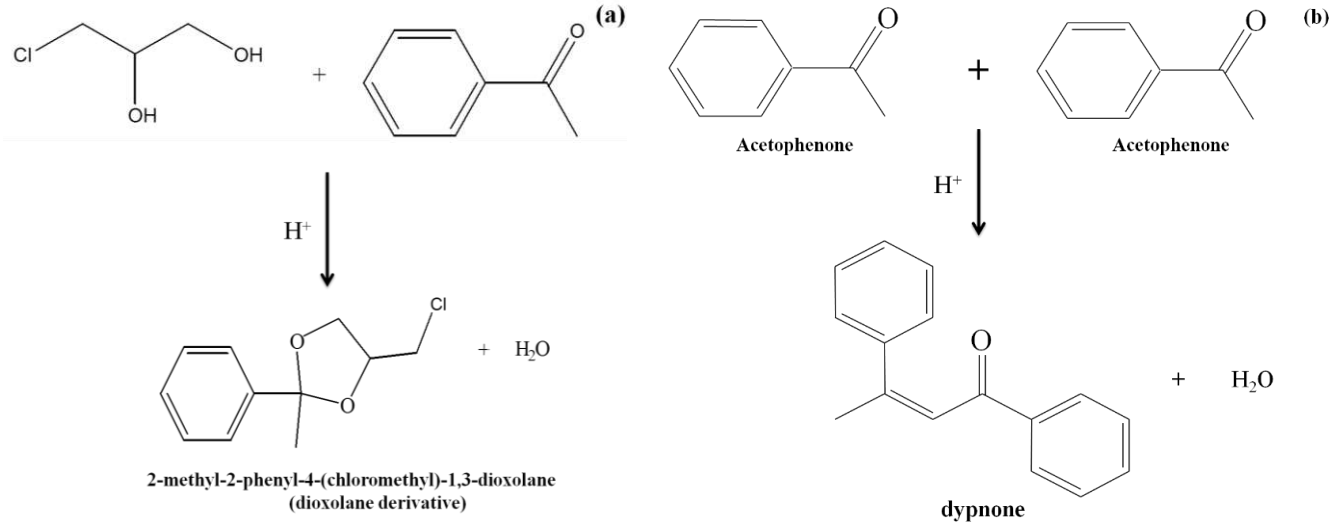

FIGURE 2. (a) Reactions in the derivatization of 3-MCPD with acetophenone, and (b) Dimerization of acetophenone

TABLE 1
THE OPTIMAL HPLC ELUTING CONDITION FOR SEPARATION

Time	Eluent composition	Flow rate
1-13 min	50% acetonitrile in pH 6.9 ammonium acetate buffer	1.0 mL min^{-1}
13-16 min	80% acetonitrile in pH 6.9 ammonium acetate buffer	1.0 mL min^{-1}
16-20 min	50% acetonitrile in pH 6.9 ammonium acetate buffer	1.0 mL min^{-1}

Quantification of 3-MCPD in samples was based on external standards using the calibration solutions described in Section 2.3. The derivateddioxolane (1.3 μg mL^{-1} as 3-MCPD) was with retention time of 11.17 min with 1.08% RSD and the peak area for quantitative determination was with 2.47% RSD for three determinations.

3.2 Optimization of MAD conditions

The isolated (eluent) solution obtained from (LPE)/clean-up was subjected to derivatization with acetophenone to form 2-methyl-2-phenyl-4-(chloromethyl) -1,3-dioxolane for the sensitive HPLC-UV analysis. When using the conventional heating/reflux protocol for the derivatization of 3-MCPD with acetophenone with 110 ^{o}C oil bath, an 18-hour reaction was required. Therefore, the microwave irradiation was investigated to accelerate the derivatization. In the studies, factors that affect the derivatization such as quantity of acetophenone and catalyst (p-toluenesulfonic acid), power and time of microwave irradiation were investigated.

3.2.1 Effect of microwave irradiation power and time

Microwave irradiation power and time is an important parameter affecting the efficiency of the derivatization of 3-MCPD posterior to the LPE/clean-up of soy sauce sample [24-26]. In order to optimize the microwave irradiation, various effective

powers of 105, 188, 362, and 502 watts were examined with 190 µL of 3-MCPD, 735 µL of acetophenone, and 20 mg of p-toluene sulfonic acid dissolved in 25 mL toluene, at microwave irradiation times ranging from 5 to 25 min. After a series of tests, results (in **Fig. 3**) indicated that the derivatization efficiency of 3-MCPD increases when the microwave irradiation power was increased from 105 to 362 W. The effective microwave irradiation power of 362 W showed maximum derivatization efficiency for the target analyte (3-MCPD). However, when microwave was irradiated at 105 and 188 W, a minimum quantity of 3-MCPD derivative was detected due to the insufficient microwave energy for the derivatization of 3-MCPD. Conversely, increasing the microwave irradiation to 502 W showed less extraction efficiency due to the sequential degradation of derivatization reagents from the derivatization vessel under high microwave irradiation. Similarly, experimental results indicated that the peak areas increased with increasing microwave irradiation time in the range of 5–10 min, and maximum derivatization quantity was obtained at 10 min (**Fig. 4**). However, with longer microwave exposure times (>10 min), the peak areas began to decrease, possibly due to the degradation of the derivatization product resulting from higher temperature. Therefore, microwave irradiation with effective irradiation power of 362 W for 10 min was selected for the subsequent analysis.

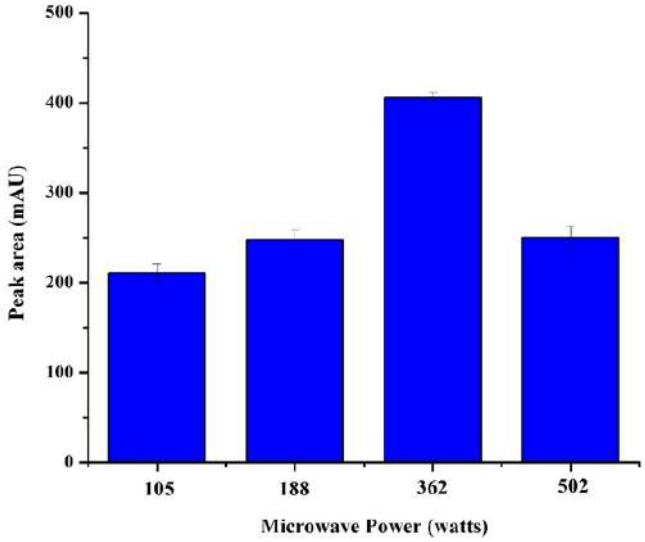

FIGURE 3. EFFECT OF THE MICROWAVE IRRADIATION POWER ON DERIVATIZATION

Conditions: 190 µL of 3-MCPD, 735 µL of Acetophenone, and 20 mg of p-toluene sulfonic acid dissolved in 25 mL toluene, under varied microwave power irradiation for 10 min.

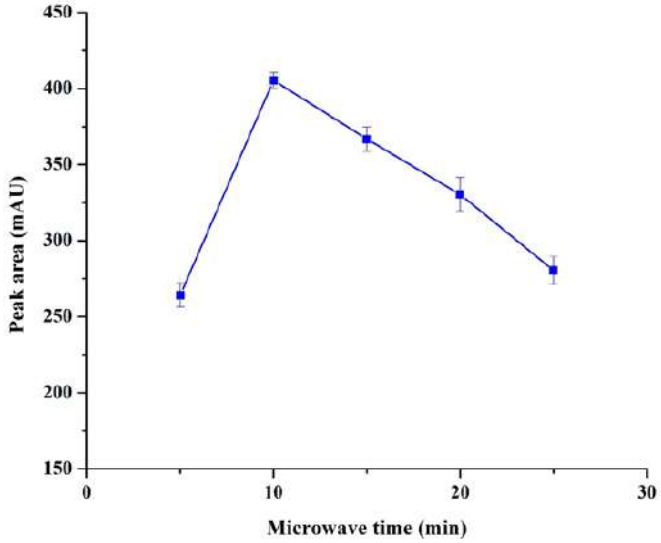

FIGURE 4. EFFECT OF THE MICROWAVE IRRADIATION TIME ON DERIVATIZATION

Conditions: 190 µL of 3-MCPD, 735 µL of acetophenone, and 20 mg of p-toluene sulfonic acid dissolved in 25 mL toluene, under 362 watts microwave irradiation

3.2.2 Optimization of derivatization agent and catalyst

The optimization of derivatization agentwas examined. Aftera series of experiment runs, the maximum derivatization efficiency was achieved at the ratio of derivatization agent (acetophenone) to 3-MCPD and was optimum at 3:1 under MAD. Regarding the quantity of catalyst required in the derivatization, there was no significant difference in detection peak area of the derivateddioxolane from 10 to 60 mg of p-toluenesulfonic acid in the reaction of 190 µL 3-MCPD with 735 µLof acetophenone. Therefore, 20 mg of p-toluenesulfonic acid was added as catalyst in the derivatization.

3.3 Method validation and real sample analysis

In order to examine the applicability of the proposed LPE/clean-up coupled with MAD followed by HPLC-UV for quantitative determination of 3-MCPD in soy sauce, standard spiked soy sauce samples were used for calibration after they were subjected to overall procedure as described in Material and Methods Section. An HPLC-UV chromatogram of derivateddioxolane from 3-MCPD standards spiked in soy sauce under chromatographic condition described in the Material and Methods section is showed in **Fig. 5(a)**. Calibration plot was built-up over the concentration range of 0.6 – 20.1 µg mL^{-1} (as 3-MCPD). Linear relationship between the peak area and the injected quantity was in good agreement with the correlation coefficients (r^2) being 0.9991. Detection limits of the proposed method was calculated based on three times the standard deviation (n=7) of the lower concentration in the method calibration plot (0.6 µg mL^{-1}divided by the detection sensitivity

(slope of calibration plot), which was 80 ng mL^{-1}. The precision of this method was estimated by performing 3 derivatizations and HPLC-UV determinations of sample spiked 3-MCPD at 5 µg mL^{-1}. The precision was 5.6 % RSD, which should be satisfactory for determining the 3-MCPD in soy sauce.In order to examine the applicability of the method to determine 3-MCPD in real sample,soy sauce sample was obtained from local traditional store in Silo town (Taiwan) and analyzed by the proposed method. The chromatogram was shown in **Fig. 5(b)**. Peak related to 3-MCPD was not found. When spiked a 5 µg mL^{-1} of 3-MCPD in real sample prior to the pretreatment and derivatization, the chromatogram was shown in **Fig. 5(c)**. The peak with retention time of 11.7 min was related to the derivateddioxolane from 3-MCPD.The recovery was ranged between 78.5 - 82.3% and the precision was 5.4 % RSD (n=5).

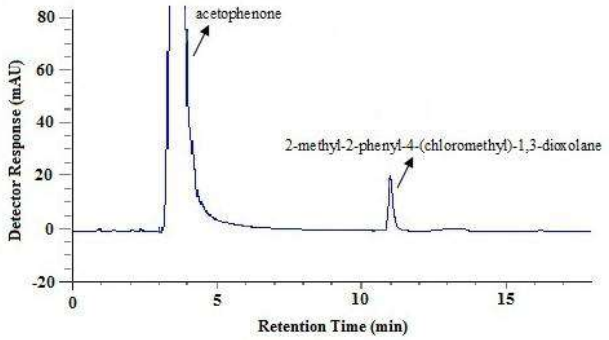

(a)

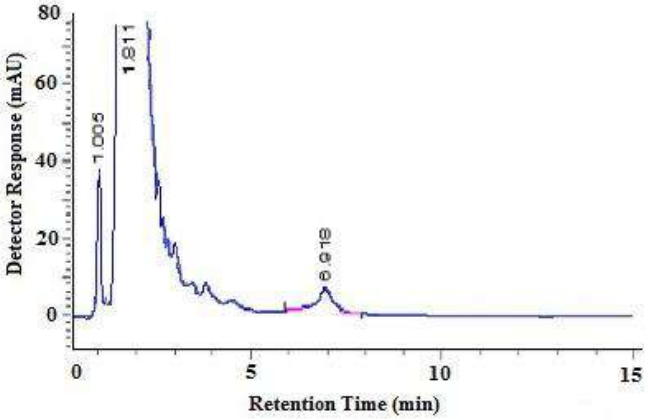

(b)

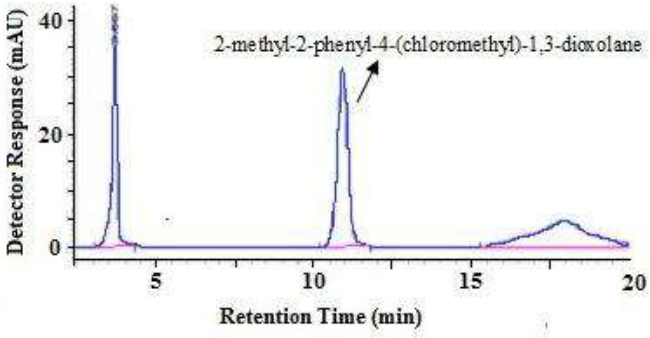

(c)

FIGURE 5. HPLC-UV chromatogram of derivateddioxolane
(a) from 3-MCPD standard solution;
(b) from soy sauce sample;
(c) from spiked soy sauce sample (5 µg mL^{-1}).

3.4 Characteristics of the proposed method

In the proposed method, the conventional HPLC-UV coupled to LPE/cleanup with MAD was developed to determine 3-MCPD in soy sauce. The detection limit (80 ng mL^{-1}) was comparable to GC-ECD and FID [13-14], although it was higher than GC-MS (15-17). Moreover, it meets the local requirement (1.0 µg/mL) and also with china and Japan's regulations [8-12]. The sensitivity of the presented method can also be improved further by decreasing the volume of re-dissolving solvent (acetonitrile) or evaporation prior to HPLC analysis. The derivatization reaction time has also been accelerated under microwave irradiation when compared with previous reports [13-15]. It takes only 10 min to complete the derivatization of 3-MCPD with acetophenone compared to several hours in other methods.

IV. CONCLUSION

In this study, a fast and sensitive LPE/*cleanup*-MAD method combined with HPLC-UV has been developed for the analysis of trace level of 3-MCPD in soy sauce samples. From the results of the applicability test for the analysis of 3-MCPD in commercial soy sauce sample, the present approach showed good linearity, good precisions, and satisfactory relative

recoveries, thus proving to be an efficient, convenient, and cost-effective method. Thus, the present technique possesses great potential in the fast preconcentration and analysis of 3-MCPD in soy sauce samples and represents an attractive alternative to both traditional and recently developed methods.

ACKNOWLEDGMENT

The authors thank the Ministry of Science and Technology of Taiwan (MOST) under the grant number NSC-91-2113-M-005-024 and NSC-101-2811-M-005-014 for financial supports.

REFERENCES

[1] R. Macarthur, C. Crews, A. Davies, P. Brereton, P. Hough, and D. Harvey,"3-Monochloropropane-1,2-diol (3-MCPD) in soy sauces and similar products available from retail outlets in the UK," Food Addit. Contam.,17, 903-906, 2000.

[2] W. Seefelder, N.Varga, A.Studer, and G. Williamson, "Esters of 3-chloro-1,2-propanediol (3-MCPD) in vegetable oils: Significance in the formation of 3-MCPD," Food Addit. Contam. 25, 391–400, 2008.

[3] P.D. Collier, D.D.O.Cromie, and A.P. Davies,"Mechanism of formation of chloropropands present in protein hydrolysates,"J. Am. Oil Chem. Soc.68, 785-790, 1991.

[4] R. El Ramy,M.OuldElhkim,S.Lezmi,and J.M.Poul,"Evaluation of the genotoxic potential of 3-monochloropropane-1,2-diol (3-MCPD) and its metabolites, glycidol and beta-chlorolactic acid, using the single cell gel/comet assay," Food ChemToxicol. 45, 41–48, 2007.

[5] J. Cerbulis, O. Parks, R. Liu, G. Piotrowski, and H. Farrell, "Occurrence of diesters of 3-chloro-1,2-propanediol in the neutral lipid fraction of goats' milk," J. Agric. Food Chem. 32, 474–476, 1984.

[6] J. Elı´sˇek, J.Davı´dek, V.Kubelka, and G.Janı´cek, "New chlorine-containing organic compounds in protein hydrolysates." J. Agric. Food Chem. 28, 1142–1144, 1980.

[7] J. Skamarauskas, W. Carter, M. Fowler, A.Madjd, T. Lister, G.Mavroudis, andD.E. Ray, "The selective neurotoxicity produced by 3-chloropropanediol in the rat is not a result of energy deprivation,"Toxicol. 232, 268–276, 2007.

[8] European Commission,"Opinion of the Scientific Committee on Food on 3-monochloro-propane-1,2-diol (3-MCPD) updating the SCF opinion of 1994 (adopted on 30 May 2001)," SCF/CS/CNTM/OTH/17 Final. Brussels: European Commission,2001.

[9] Food Standard Agency,"Survey of 3-monochloropropane-1, 2-diol (3-MCPD) in soy sauce and related products," No: 14/01, 2001.

[10] X. Xing, and Y. Cao, "Determination of 3-chloro-1,2-propanediol in soy sauces by capillary electrophoresis with electrochemical detection,"Food Control. 18 167–172, 2007.

[11] C. Crews, S.Hasnip, S. Chapman, P. Hough, N. Potter, J. Todd, P. Brereton, and W. Matthews, "Survey of chloropropanols in soy sauces and related products purchased in the UK in 2000 and 2002."Food Additives and Contaminates, 20, 916-922, 2003.

[12] W.C. Chung, K.-Y. Hui, and S. C. Cheng, "Sensitive method for the determination of 1,3-dichloropropan-2-ol and 3-chloropropane-1,2-diol in soy sauce by capillary gas chromatography with mass spectrometric detection,"J. Chromatogr. A, 952, 185–192, 2002.

[13] W.J. Plantingua, W.G. van-Toorn, and G.H.D. van der Stegen, "Determination of 3-chloropropane-1,2-diol in liquid hydrolysed vegetable proteins by capillary gas chromatography with flame ionization detection,"J. Chromatogr., 555, 311-314, 1991.

[14] K. Erik, "Determination of 3-chloropropandiol and related dioxolanes by gas chromatography,"J. Chromatogr., 605, 134-138, 1992.

[15] C.G. Hamlet, "Analytical methods for the determination of 3-chloro-1,2-propandiol and 2-chloro-1,3-propandiol in hydrolysed vegetable protein, seasonings and food products using gas chromatography ion trap tandem mass spectrometry,"Food Addit. Contam. 15, 451–465, 1998.

[16] M. Huang, G. Jiang, B. He, J. Liu, Q. Zhou, W. Fu, and Y. Wu, "Determination of 3-chloropropane-1,2-diol in liquid hydrolyzed vegetable proteins and soy sauce by solid-phase microextraction and gas chromatography/mass spectrometry,"Anal. Sci. 21, 1343-1347, 2005.

[17] P.J. Nyman,G.W. Diachenko, and G.A.Perfetti,"Determination of 1,3-dichloropropanol in soy and related sauces by using gas chromatography/mass spectrometry,"Food Addit. Contam.20, 903-908, 2003.

[18] D.C. Meierhans, S.Bruehlmann, J.Meili, and C.Taeschler,"Sensitive method for the determination of 3-chloropropane-1,2-diol and 2-chloropropane-1,3-diol by capillary gas chromatography with mass spectrometric detection," J. Chromatogr.A, 802, 325-333, 1998.

[19] W. Fu, Y.N. Wu, Y.F. Zhao, J.B. Ma, and Q. Zhang, "Determination of dichloropropanols and monochloropropanediols in soy sauce by capillary gas chromatography/ion trap mass spectrometry using stable isotope dilution technique,"Chin. J. Food Hyg.16, 289-294, 2004.

[20] C. Crews, G.LeBrun, and P.A. Brereton, "Determination of 1,3-dichloropropanol in soy sauces by automated headspace gas chromatography-mass spectrometry,"Food Addit. Contam.19, 343-349, 2002.

[21] P. Brereton, J. Kelly, C. Crews, S.Honour, R. Wood, and A. Davies, "Determination of 3-chloro-1,2-propanediol in foods and food ingredients by gas chromatography with mass spectrometric detection: collaborative study," J. AOAC Int. 84, 455-65, 2001.

[22] P. Robert, and J.F.Melroy, "Determination of residual epichlorohydrin and 3-chloropropandiol in water by gas chromatography with electro-capture detection,"J. Chromatogr. 439, 448-452, 1988.

[23] M.K.P. Leung, B.K.W. Chiu, and M.H.W. Lam, "Molecular sensing of 3-chloro-1,2-propanediol by molecular imprinting,"Anal. Chim.Acta, 491, 15–25, 2003.

[24] M. C. Wei, and J.F. Jen, "Determination of polycyclic aromatic hydrocarbons in aqueous samples by microwave assisted headspace solid-phase microextraction and gas chromatography/flame ionization detection,"Talanta,72, 1269-74, 2007.

[25] P. Vinoth Kumar, and J.F.Jen, "Rapid determination of DDT and its main metabolites in aqueous samples by one-step microwave-assisted headspace controlled- temperature liquid-phase microextraction and gas chromatography with electron capture detections,". Chemosphere, 83, 200-207, 2011.

[26] C. H. Lin, C. T. Yan, P.Vinoth Kumar, H.P. Li, and J. F. Jen, "Determination of pyrethroid metabolites in human urine using liquid phase microextraction coupled in-syringe derivatization followed by gas chromatography/electron capture detection," Anal.Bioanal. Chem. 401, 927-937, 2011.

[27] Y.P. Lin, Y.S. Su, and J.F. Jen, "Capillary Electrophoretic analysis of g-aminobutyric acid and alanine in tea with in-capillary derivatization and fluorescence detection," J. Agri. Food Chem. 55, 2103-2108, 2007.

Synthesis of oligoguanidine - Based on polycondensation and compare their Antimicrobial Activities with Chloramine B

Nguyen Viet Hung[1], Nguyen Viet Bac[2], Tran Van Chung[3], Tran Duc Luong[4]

[1,2,3]Institute of Chemical and material, Hanoi
[4]Nam Dinh University of Nursing
Corresponding author: Nguyen Viet Hung; Email: Hungdiego76@yahoo.com

Abstract— *Oligoguanidine with chain extension were synthesized by condensation and cross-linking polymerizations in an attempt to increase molecular weight and charge density of the anti microbial oligoguanidine. The reactions are procedure at 170 ^oC for 5h with ratio molar of HMDA: GHC = 1: 1.1, refined by vacuum filter at 60 ^oC. The Oligoguanidine OHMG.HCl synthesized has molecular weight equal 521 g/mol, chain structure and good water solubility. The comparison results of the antimicrobial activities of oligoguanidine with chloramine B indicated that MIC index of OHMG.HCl is 5ppm during MIC index of chloramine B is 50 ppm; MBC of OHMG.HCl is 12 minutes and MBC of chloramine B is 11 minutes; The SEM, TEM imagines exhibited clear biocide, low residue microorganism of OHMG.HCl. The LC-MS spectrum indicates the presence of haloacetic acid following the bactericidal action of chloramphen B, while OHGM.HCl is not available. This result confirms the environmental friendliness of oligoguanidine.*

Keywords— Oligoguanidine, Oligohexamethylene guanidine hydrochloride, antimicrobial polymer.

I. INTRODUCTION

Antimicrobial polymer is a range of agents with bacteria or fungi inhibition ability, which has been used widely in plastic, textile, water purification, and so on. Most of antimicrobial polymers bear cationic groups along polymer chains, thus facilitating the adsorption of the polymer onto bacteria surfaces and further inhibiting the growth of bacteria via various mechanisms. As one of the cationic antimicrobial polymers, the guanidine-based polymer has attracted substantial interests due to its wide spectrum antimicrobial activity, excellent biocide efficiency and nontoxicity. Oligoguanidine is usually synthesized by polycondensation between guanidinium and diamine, The chain cross-linking would occur if prolonging reaction time and increasing reaction temperature. At low molecular weight constrains the guanidine polymer as antimicrobial agent would be used [6],[12] Guanidine polymer inhibits bacterial growth by attacking them through electrostatic attraction between cationic guanidio-groups and anionic groups on the cell surface of bacteria. After attaching to bacteria cells, guanidine polymer induces bacterial membrane collapsed and intracellular components leaked. Therefore positive charge density, molecular weight and molecular structure of guanidine polymer would influence adsorption on bacterial surface and inhibition efficiency [4], [7], [10]. At present, antibacterial substances such as atomic chlorine, chloramine B are used in practice. However these antibacterial substances are often used in large quantities, especially when reducing, especially after in water disinfected, there are a residue and by-product of chlorine compounds that are directly harmful to the health of humans and organisms [1]. In this article, a method synthesizing oligohexamethyleneguanidine hydrochloride (OHMG.HCl) synthesis, and evaluating its disinfection efficacy over chloramine B are presented in detail.

II. EXPERIMENTAL

2.1 Materials

Guanidine hydrochloride (GHC), purity ≥ 99.0% (Merck, Germany). Hexamethylene diamine (HMDA), purity ≥ 99.0% (Merck, Germany). Chloramine B, purity ≥ 99.0% (Pharmacy Center 2 Company).

Escherichia coli (E. coli) were obtained from the National Institute of Hygiene and Epidemiology; and the E. coli was cultured overnight at 37 ^oC in LB Broth prior to use.

2.2 Synthesis method of Oligoguanidine

Oligo guanidine was synthesized by a two-step polymerization. The poligo was obtained by polycondensation from amine and guanidine hydrochloride. The detailed procedures are as follows: HMDA: GHC = 1: 1.1 ratio molar ratio of chemicals containing guanidine groups and amino groups were added into a 500 mL three-neck flask, the reagents were stirred mechanically and reaction temperature was increased step by step, first kept at 100^oC for 1 hr, then 170 ^oC for 5 hrs, until the stirrer could continue for the high viscosity of polymer. The reactant was further diluted with de-ionized water to 20% (wt) and temperature was increased to 60 ^oC for 6 hrs; then the reaction was stopped and the modified guanidine-based polymer was obtained. De-ionized water was used as a solvent for the polymer [3], [9].

The obtained oligoguanidine by polycondensation between hexamethylene diamine and guanidine hydrochloride is as following scheme 1 [8], [11].

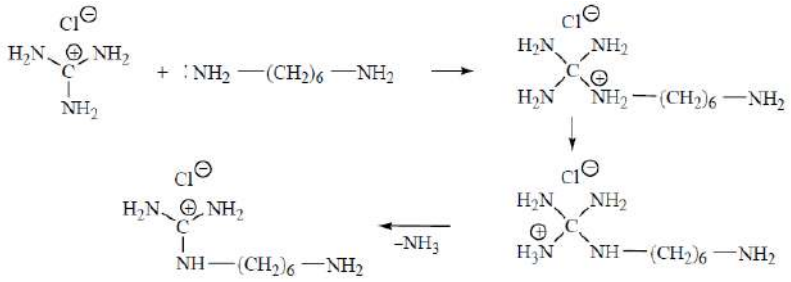

FIGURE 1. SCHEME OF OLIGOGUANIDINE SYNTHESIS

The oligoguanidine synthesis from GHC and HMDA can be carried out by nucleophilic mechanisms. The reaction between the monomers is implemented by bonding the free electron pairing of the nitrogen atom in the HMDA molecule into the positive charge of the carbon atom in the GHC (with the proton transfer from the amino group HMDA into the amine group of GHC). Under the reaction medium, the polymer chain continues to grow and will be limited by the solubility of the oligoguanidine. Therefore, the experimental conditions of this method are very important, which affect the quality and the characteristics of OHMG.HCl.

2.3 Characterization of Oligoguanidine.

GPC (Pump: Waters 600E System Controller; Detector: Waters 410 Differential Refractometer; Colums: Ultrahydrogel 250 and 500) on Shimadzu CLASS-VIP V6.14SP1 gel electrophoresis equipment, at the Faculty of Chemistry, Hanoi National University, was used to measure molecular weight and ^{1}H-NMR, COSY, HSQC spectra was used to determine structure of of Oligoguanidine.

2.4 Minimum Inhibition Concentration (MIC).

The minimum inhibitory concentration (MIC) is the lowest concentration of a chemical which prevents visible growth of a bacterrium. A serial dilution method was used to determine MIC of Oligoguanidine against *E. coli*. Fresh cultured *E. coli* was diluted with LB broth to 106CFU/ml which was reckoned by an OD600-Con standard curve. Oligomers dissolved in sterile deionized water were serially diluted in LB broth, the same amount of E. coli were put into polymer broth solution. Both seeded tubes and growth controls were incubated at 37 ^{o}C for 18h. MIC was the lowest concentration inhibiting visible growth of bacteria compared with control samples.

2.5 The time for killing bacteria by minimum bacteria concentration (MBC).

The minimum bactericidal concentration (MBC) is the lowest concentration of an antibacterial agent equired to kill a particular bacterrium. The minimum antibacterial concentration index was tested on Ecoli bacteria with a concentration of 1 to 100 ppm of product in aqueous solvents. Initiate bacterial culture is implemented with 5 mL of product solution in test tubes, then the tubes are being shaken before incubation at 37 ° C for 48 hours. To test the growth of bacteria in growth medium with and without bacterial growth by determining the growth of the organism together with the turbidity in the tubes.

2.6 Study of microstructure of oligome by SEM, TEM

Scanning electron microscopy (SEM) to evaluate the surface structure of the object by magnification to tens of thousands. he images obtained from this method, combined with the results of other methods, can give an estimate of the surface structure of the sample about size, distribution…

Transmission electron microscopy (TEM) is a device for the study of sample microstructure, using high energy electron beams, penetrating through thin sample specimens and using magnetic lenses. The TEM method can produce solid-state images with high contrast and resolution, and at the same time provide easy information about the structure of the material. TEM gives the real picture of the structure inside a solid, so it gives more information.

Experimental: The SEM image, TEM image used in this thesis was recorded on JEOL 1010 (Japan) at National Institute of Hygiene and Epidemiology.

III. RESULTS AND DISCUSSION

3.1 Result of synthesis and Characterization of Oligoguanidine.

3.1.1 The molecular weight (Mw) of Oligoguanidine was presented in Table 1.

TABLE 1
RESULT OF THE MOLECULAR WEIGHT, CHARGE DENSITY

Value	pre-oligomer	Oligomer
Mw (g/mol)	160 ± 10	521 ± 20
Electric charge density (meq/g)	2.45 ± 0.11	3.60 ± 0.13

3.1.2 The results of ^{1}H-NMR

Nuclear magnetic resonance spectra (^{1}H-NMR) at 500 MHz of Oligoguanidine (OHMG.HCl) in the synthesized product showed in Figure 2 including peak at 7.490 ppm - corresponding to the group - NH-C (NH) -NH-; peak at 1,809 ppm - corresponding to the group (- CH_2-)n.

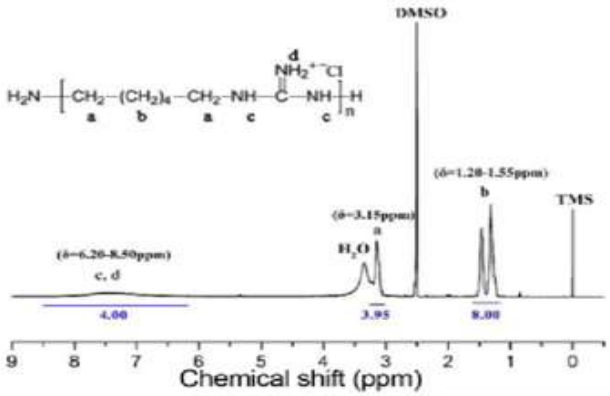

FIGURE 2. H-NMR SPECTRUM OF TH SYNTHESIZED OHMG.HCL

The results of this study have shown that OHMG.HCl can be synthesized from guanidine hydrochloride and hexamethylene diamine by melting molten condensation. Figure 2 confirmed the synthesized product having a chain structure.

3.2 The result of antimicrobial Effects of oligoguanidine OHMG.HCl and chloramine B in the sample

The antibacterial effects of OHMG and were compared to chloramine B baesd on MIC, MBC index, antibacterial time SEM and TEM spectra

3.2.1 Results of MIC index

The results of determining MIC are given in Table 2. This is shown that, for the concentrations of OHMG.HCl > 5 ppm there is no growth of the E. coli strain in, while for chloramine B is 50 ppm.

TABLE 2
MIC VALUE OF OHMG.HCL AND CHLORAMINE B

Concentration (ppm)	MIC value	
	OHMG.HCl	Chloramine B
100	-	-
50	-	-
10	-	+
5	-	+
3	+	+
1	+	+

(-): no growth of bacteria.
(+): there is the development of bacteria

3.2.2 The time for killing bacteria (MBC)

The results are shown in Table 3. It was shown that the MBC index of OHMG.HCl was 12 minutes and that of Chloramine B was 11 minutes.

TABLE 3
MBC RESULT OF OHMG.HCL AND CHLORAMINE B

Time (minute)	MBC Value	
	OHMG.HCl (5 ppm)	Chloramine B (50 ppm)
1	+	+
2	+	+
4	+	+
6	+	+
8	+	+
10	+	+
11	+	-
12	-	-
13	-	-
14	-	-
15	-	-

(-): no growth of bacteria.
(+): there is the development of bacteria

3.2.3 Results of SEM and TEM imagines

The SEM and TEM measurements of antimicrobial Effects of samples showed in Figure 3 and 4

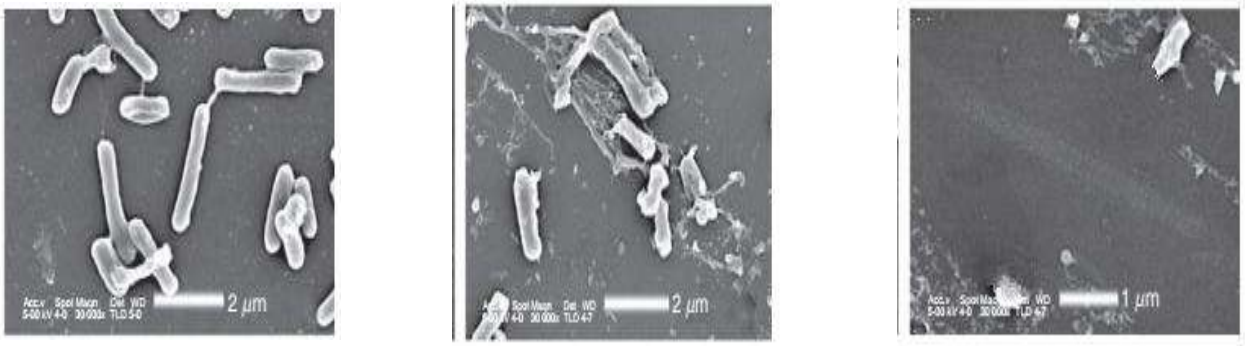

(a) Control sample **(b) Chloramine B** **(c) OHMG.HCl**

FIGURE 3. SEM IMAGINE OF THE RESIDUE OF E.COLI AFTER DISINFECTION

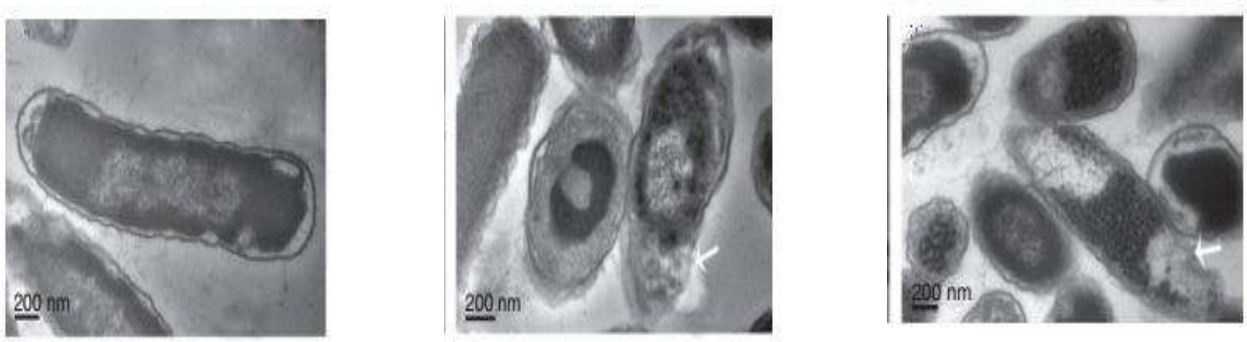

(a) Sample with 5 ppm OHMG.HCl after 1 minute **(b) Sample with 5ppm OHMG.HCl after 5 minute** **(c) Sample with 5ppm OHMG.HCl after 12 minute**

FIGURE 4. TEM IMAGINE SAMPLE OF E.COLI USING 5PPM OHMG.HCL

SEM images showed the extent of the damage of the cells after exposured to different doses of OHMG.HCl, and only high concentrations of OHMG.HCl could result in concave collapses in most of the treated cells (Fig. 3c). In accordance with the SEM results, the TEM results showed that a low concentration of OHMG.HCl mainly damaged the outer membrane structure, while no significant damage to the intracellular structure was observed. In contrast, after exposure to a high concentration of OHMG.HCl, although the general morphological structure of the cells was still retained, the integrity of the cell wall layer structure was destroyed, most of which was collapsed, and obvious gaps could be seen even in some cells. It is concluded that the membrane damage was dose-dependent and local, and the disorganization of the membrane lipid structure was local and not global; the concave collapses observed in SEM and gaps observed in TEM indicated that the formation of local pores was possible. Bisbiguanides antiseptics, alexidine and chlorhexidine, could be adsorbed to E. coli cells and to isolated membrane components (Fig. 4a), which could lead to phospholipid phase separation and domain formation. So, it was possible that OHMG.HCl was adsorbed (Fig. 4b), bound to the phospholipid of cell membrane and led to the formation of the local pores (Fig. 4c); as a result, the cells lost their viability.

Oligoguanide were rapidly adsorbed to the negatively charged bacterial cell surface, then impaired the outer membrane and caused domain formation of the acidic phospholipids of the cytoplasmic membrane with an increase in the cytoplasmic membrane permeability; suggested that the uptake of chlorhexidine by *E. coli* was very rapid. concluded that death of cells and cytoplasmic membrane damage were directly associated and were a direct result of biocide action rather than mediated through the induction of autolytic enzymes.

3.2.4 Results of LC-MS

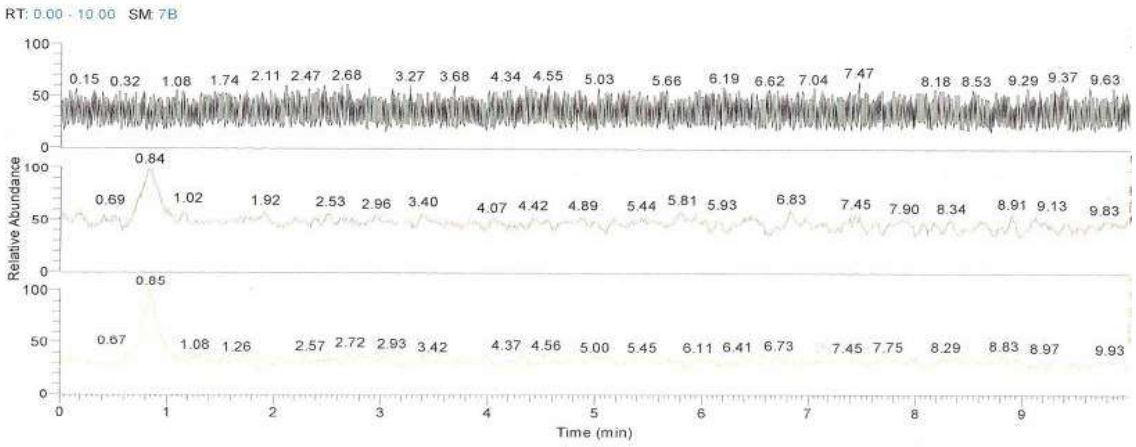

FIGURE 5. LIQUID CHROMATOGRAPHY OF TEST SAMPLE USING OHMG.HCL AND CHLORAMINE B

The results of liquid chromatography of the two samples showed that for the bactericidal agent (OHMG.HCl), no retention time was observed for the extra compounds such as in the prototype with chloramine B at 0.84 and 0.85 min). Corresponding to the retention time at 0.84 and 0.85 minutes the obtained MS spectrum is shown in Figure 6.

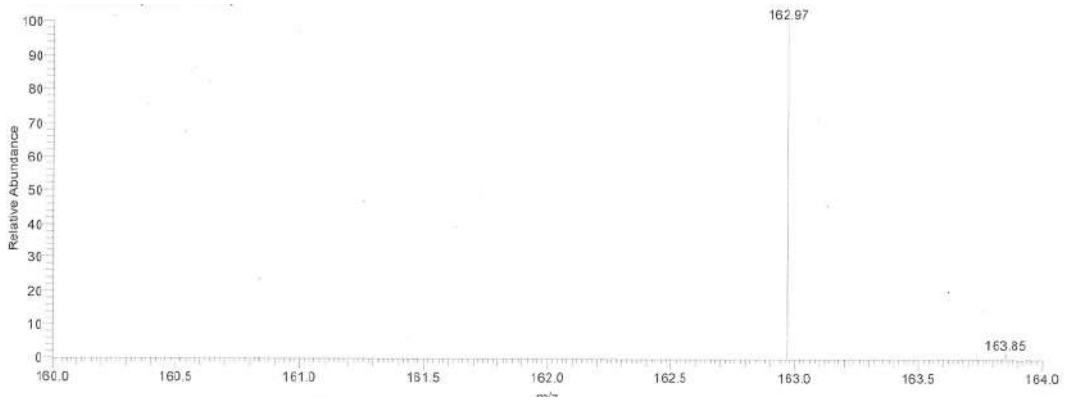

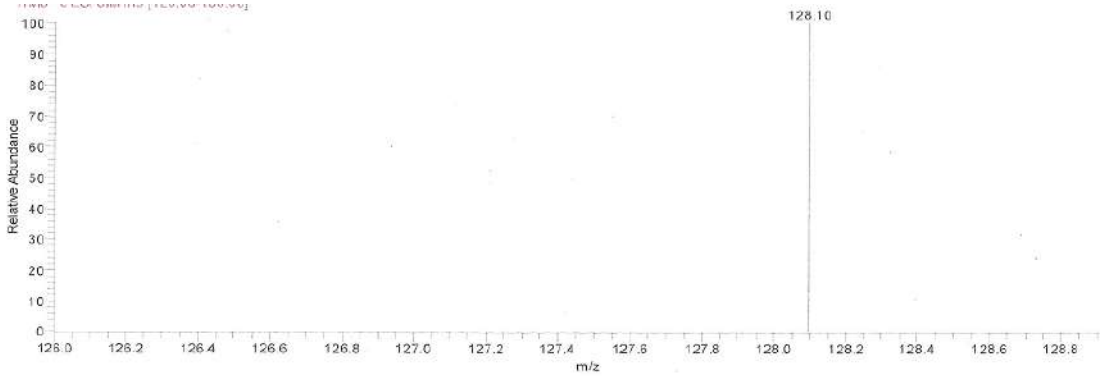

FIGURE 6. MS SPECTRUM OF TEST SAMPLE USING CHLORAMINE B

With the MS spectrum, the two retention times at 0.84 and 0.85 minutes exhibit the corresponding values of m / z of 162.97 and 128.10 respectively for corresponding two fragments as $CHCl_3COO^-$ and $CHCl_2COO$.

As compared to chloramine B, OHMG.HCl is a highly effective, non-toxic bactericidal agent, which does not create dangerous by-products in the process. Particularly when chloramine B used, there is the appearance of the by-products haloacetic acid in the water affecting human health.

IV. CONCLUSION

Oligoguanidine OHMG.HCl was synthesized by a two-step polymerization consisting of condensation and cross-linking to obtain the antimicrobial oligomer with a higher molecular weightand cationic form with the higer positive charge density than pre-polymer. The Oligoguanidine synthesized has a chain structure, good water solubility and suitable for use as a disinfectant in wastewater treatment. Antimicrobial ability of OHMG.HCl was adjusted by varying alkyl monomer ratios at the same content of guanidio groups when they are absorbed into the cell walls of the bacteria

Results of the bactericidal efficiency comparison with Chloramine B showed that the synthetic OHMG.HCl has a fast killing time, low consumption environmental friendliness and not cause a toxic effect on health.

REFERENCES

[1] Tran Thi Mai Phuong (2017), Environmental toxicology, Ho Chi Minh City National University.

[2] Nguyễn Đình Triệu, Universal methods in organic and biochemical chemistry, Viet nam National University, 2007.

[3] Nguyen Viet Hung, Nguyen Viet Bac, Tran Van Chung, Vo Hoang Phuong (2013), Synthesis of germicidal oligomers based on guanidine, 6th National Chemistry Conference, T.51 Chemistry Journal, pages 832-837.

[4] Asiedu-Gyekye, I. J. Mahmood A. S. Awortwe C. and Nyarko A. K (2015), *Toxicological assessment of polyhexamethylene biguanide for water treatment,* Interdiscip Toxicol , Vol 8 (4), pp193-202.

[5] Hye min Choi, Keuk-Jun Kim, Dong Gun Lee (2017), *Antifungal activity of the cationic antimicrobial polymer-polyhexamethylene guanidine hydrochloride and its mode of action*, Fungal Biology, Volume 121, Issue 1, pp 53-60.

[6] Mandygra, M. S., & Lysytsya, A. V. (2014), *Some aspects of the polyhexa-methyleneguanidine salts effect on cell cultures,* Agricultural Science and Practice, vol 1(1), pp 62-67.

[7] Mashat, B. H. (2016), *Polyhexamethylene biguanide hydrochloride: Features and applications*, British Journal of Environmental Sciences, vol 4(1), pp 49-55.

[8] Petra Feiertag, Martin Albert, Eva-M. Ecker-Eckhofen, Gertraud Hayn, Helmut Hönig, Hanns W. Oberwalder, Robert Saf, Andreas Schmidt, Oskar Schmidt, Dmitrij Topchiev (2003), *Structural Characterization of Biocidal Oligoguanidines*, Macromolecular Rapid Communications, vol. 24, Issue 9, pp 567-570.

[9] Pranav R. Joshi, Joseph McGuire, Jennifer A. Neff (2009), *Synthesis and antibacterial activity of nisin-containing block copolymers*, Journal of Biomedical Materials Research Part B: Applied Biomaterials, vol. 91B, Issue 1, pp 128-134.

[10] Rembe, J-D. Fromm-Dornieden C. Schafer N. Bohm J. K. and Stuermer E. K (2016), *Comparing two polymeric biguanides: chemical distinction, antiseptic efficacy and cytotoxicity of polyaminopropyl biguanide and polyhexamethylene biguanide*, Journal of Medical Microbiology, vol65, pp 867-876.

[11] S. A. Stel'mah, L. U. Bazaron, D. M. Mognonov (2010), *On the mechanism of the hexamethylenediamine and guanidine hydrochloride polycondensation*, Russian Journal of Applied Chemistry, vol. 83, Issue 2, pp 342-344.

[12] V. V. Goncharuk, V. F. Vakulenko, Yu. O. Shvadchina, L. M. Oleinik, T. N. Sitnichenko (2008), *Impact of polyhexamethylene guanidine hydrochloride on the process of coagulation treatment of river waters*, Journal of Water Chemistry and Technology, vol. 30, Issue 5, pp 314-321.

AD Publications
Sector-3, MP Nagar, Bikaner,
Rajasthan, India
www.adpublications.org, info@adpublications.org